

DENSE CORE FORMATION IN TURBULENT
MOLECULAR CLOUDS

**DENSE CORE FORMATION SIMULATIONS IN TURBULENT
MOLECULAR CLOUDS WITH LARGE SCALE ANISOTROPY**

By
NICOLAS PETITCLERC, M.SC

A Thesis
Submitted in Partial Fulfillment
of the Requirements
for the Degree of

Doctor of Philosophy

March 2009

McMaster University

© 2009 Nicolas Petitclerc

DOCTOR OF PHILOSOPHY (2009) McMaster University
(Physics and Astronomy) Hamilton, Ontario

TITLE: Dense Core Formation Simulations in Turbulent Molecular
Clouds with Large Scale Anisotropy

AUTHOR: Nicolas Petitclerc, M.Sc. (University of Montreal)

SUPERVISOR: Professor A. Sills and Professor J. Wadsley

NUMBER OF PAGES: XVIII, 184

Abstract

In this thesis, we study star formation in clustered environment within molecular clouds using Smooth Particle Hydrodynamics (SPH) simulations. Our first approach was to use “sink particles” to replace the dense gas particles where stars are forming. We implemented this type of particle in GASOLINE, and ran a simulation with a similar set of parameters to Bate et al. (2003). We found a good general agreement with this study. However, this work raised increasing concerns about some of the approximations used to follow the fragmentation process over many orders of magnitude in density. Our first issue was with the polytropic equation of state used to simulate gas of high density, that we believe would require some form of radiative transfer to be reliable. We also had concerns about the sink particles themselves, potentially overestimating the accretion rates.

This guided our following work, where we choose to avoid both sinks and polytropic assumptions; allowing us to concentrate on the role of turbulence in forming prestellar cores. Supersonic turbulence is known to decay rapidly even when considering magnetic fields and gravity. However these studies are based on grid codes for periodic boxes. Our simulations are not periodic, they have open boundaries. Therefore the gravitational collapse can occur for the whole molecular cloud, not only for small portions of it. Hence the picture we observe in our self-gravitating turbulent molecular clouds is different. We found that under gravitational collapse turbulence is naturally developed and maintained with properties in good agreement with the current observational and theoretical picture.

We also compared the cores we formed with observations. We looked at several observable properties of cores: density profiles, velocity dispersion and rotation of the cores, core-core velocity dispersion, core-envelope velocity dispersion, velocity dispersion vs. core size relation and the core mass func-

tion. We found a good general agreement between our simulated and observed cores, which indicates that extra physics like magnetic fields, outflows, proper equation of state or radiative transfer would have only secondary effects at this formation stages, or would tend to cancel each other.

Acknowledgments

Throughout the years, many people contributed in a way or another to the accomplishment of this work. I would especially like to thank my co-supervisor Dr. James Wadsley for his help and abundant suggestions that made this project possible. I am also very thankful that he let me use (and abuse) of *Imp*, his computer. This project wouldn't have been possible either without the contribution of my other co-supervisor Dr. Alison Sills. Her advice and comments, especially at the thesis writing stage, were very helpful.

I would like to give a special mention to Dr. Kari Dalnoki-Veress whose advice as graduate student coordinator were the turning point of my PhD. I would also like to thanks Dr. Christine Wilson whose comments as a supervising committee member were very helpful. The collaborations I had with Dr. Michael Reid were also essential to connect my simulations with observations.

Through the years, many office mates came and went, but one of them was there the whole time and luckily it was the best one ever! Thanks Sijing Shen for all those very interesting conversations... Also, you were always there to listen during my research, no matter if I had problems or successes, that was a precious help at times.

I also need to thank SHARCnet and everyone involved in it, to provide such an essential computing tool for research. No matter how much we can complain about it on the everyday basis, it is still an amazing resource and I am glad I had the chance to enjoy it. I am especially grateful for the dedicated resources they granted me for this work.

Table of Contents

Acknowledgments	v
List of Figures	ix
List of Tables	xvii
Chapter 1	
Introduction	1
Chapter 2	
Star Cluster Formation	10
2.1 Introduction	10
2.1.1 Fragmentation Models	12
2.1.2 Protostellar Collapse	13
2.1.3 Equation of state	16
2.1.4 BBB3 code	19
2.1.5 Sink particles	19
2.2 Methods	22
2.2.1 Initial conditions	22
2.2.2 Turbulent Velocity Field	23
2.3 Results and discussion	24
2.3.1 Energy evolution	25
2.3.2 Star formation	31
2.3.3 Multiplicity	32
2.3.4 Mass Accretion History	37
2.4 Testing sinks	40
2.5 Conclusion	43

Chapter 3	
Molecular Cloud Turbulence	49
3.1 Introduction	49
3.1.1 Kolmogorov and Burgers turbulence theory	52
3.1.2 Inertial range	53
3.1.3 Timescale	53
3.1.4 The role of gravity within molecular clouds	55
3.2 Turbulence Observables	56
3.2.1 Scaling relation	56
3.2.2 Universality of the turbulence	57
3.2.3 Power spectrum	57
3.2.4 Generalized structure function	59
3.2.5 Observed power spectrum	63
3.2.6 Density Probability Density Function	63
3.3 Initial Conditions	64
3.3.1 Anisotropic Turbulent Velocity Field	65
3.3.1.1 Shear vectors	66
3.3.1.2 Anisotropic collapse shapes	67
3.3.1.3 Large and small scale turbulence	68
3.3.1.4 Statistical study of anisotropy	69
3.3.2 Resolution Limit for Density Peaks	70
3.4 Results	73
3.4.1 Turbulence Magnitude Evolution	73
3.4.2 Energy distribution	77
3.4.3 Probability Distribution Function (PDF)	78
3.4.4 Velocity Structure Functions	82
3.5 Conclusion	85
Chapter 4	
Proto-stellar cores	99
4.1 Introduction	99
4.2 Simulated observations	100
4.3 Core formation	108
4.4 Core sample selection	109
4.5 Cores map	112
4.6 Density profiles	126
4.7 Velocity dispersion	132
4.7.1 Velocity dispersion with size of cores	133
4.7.2 Velocity dispersion vs. Density relation	136
4.8 Mean velocity	140
4.9 Core-Core velocity dispersion	152

4.10	Core-envelope velocity dispersion	152
4.11	Core observed mass	154
4.11.1	Core Mass Function (CMF)	155
4.11.2	3D cores analysis	159
4.12	Conclusion	166
Chapter 5		
	Conclusion	173
5.1	Future work	176
Chapter A		
	Appendix A	179

List of Figures

2.1	Central temperature evolution with central density from Masunaga & Inutsuka (2000), modified by Andre et al. (2008).	13
2.2	Timescale for the evolution of the central density, in units of free fall time $t_{ff}^0 = 1.781 \times 10^5 yr$ (Stamatellos et al. (2007)). The red dots are a comparison to the Masunaga & Inutsuka (2000) calculations.	16
2.3	Barotropic equation of state (dotted line) compared to Masunaga & Inutsuka (2000) calculations (full line), from Bate et al. (2003).	17
2.4	Temperature vs. density at different time steps from Stamatellos et al. (2007). The lines shows the time evolution from the thin black line ($0.843t_{ff}$) to cyan, magenta, black, green to red ($1.05156t_{ff}$). At later stages the regions around the center heat up at much lower density. The dotted line is to compare to Masunaga & Inutsuka (2000).	18
2.5	Snapshots showing the evolution of the star forming clump. The gas density is plotted on a log scale $-21.2 \leq \log_{10}\rho \leq -11.2$ g/cm ³ on the z axis. Each panel is 77 400 AU across and the stars are shown as white dots on the later evolution time steps. The time for each snapshot is indicated in years and in free-fall time (t_{ff}) fraction.	26
2.6	Same as Figure 2.5, but for the inner 20000 AU. All the stars form originally near the center, but some are kicked out by strong gravitational interactions.	27

2.7	Evolution of the kinetic (dashed line) and gravitational (full line; the negative value is shown to compare to the kinetic) energy per mass for the gas (top panel), the stars (middle panel) and both combined (bottom panel). We can see the decay of the initial turbulence and the later re-injection of kinetic energy by the global collapse and the stirring effect of the star particles.	28
2.8	Plot of the negative of the energy ratios (kinetic over gravitational) for the gas (full line), the stars (dashed) and for both combined (dot-dashed). The virial ratio is marked by the dotted line.	29
2.9	Evolution of specific scalar momentum in units of Mach number ($c_s = 1.84 \times 10^4$ cm/s). The full line near the bottom is for the gas, the full line to the right is for stars only and the dashed line is for the combination of both.	30
2.10	Velocity dispersion for the gas and stars (full lines) and $\hat{x}, \hat{y}, \hat{z}$ components (dotted or dashed lines).	30
2.11	The initial mass function of all the sink particles formed. The Salpeter and Kroupa mass distributions are plotted for reference and normalized to fit the high mass end of our distribution.	33
2.12	The cumulative initial mass function of all the sink particles formed, representing the fraction of stars in the clump with a mass equal or larger to the binned value. The Salpeter and Kroupa mass distributions are plotted for reference and normalized to fit the high mass end of our distribution.	34
2.13	Histogram of the binary fraction in function of mass at the final stage (135 000 yr).	38
2.14	Observed mass distribution of the binary fraction, from Goodwin's talk at the Multiplicity in star formation workshop in Toronto (http://www.astro.utoronto.ca/msf/talks/Day1/MSF2007-1A1-Goodwin.pdf).	39
2.15	Evolution tracks of the sink particles. The stars with final masses below 0.01 solar mass are shown in green, above 0.631 solar mass in red and in between these masses in black.	40
2.16	Test for the number of neighbours effects. The black line/dots are the results using 32 neighbours and in red the results using 50 neighbours. The first plot is showing the mass accreted over time. The middle is showing the density for each gas particles as a function of its distance from the sink after 120 years. And in the bottom plot we see the velocity magnitude as a function of the distance.	41

3.1	The scaling relation of velocity dispersion in function of the scale for 27 different molecular clouds from Heyer & Brunt (2004). The filled circles at the upper end of each dotted line represent the global line-width velocity dispersion as in the Larson relation. The light full line is the bisector fit of all points. The thick full line is the bisector fit of the filled points only. The small scatter of points attest that the power-law relation is followed over a large range of scales.	58
3.2	Schematic view of the 3 possible configurations of shear vectors. Configuration a) represents a filament collapse, b) a sheet and c) the ribbon case.	67
3.3	Statistical distribution of the shear vectors λ_1 and λ_3 , where $\lambda_1 > \lambda_2 > \lambda_3$ and $\lambda_1 + \lambda_2 + \lambda_3 = 0$. The contour lines show the variations of a standard deviation from the maximum likelihood. The filled square represent the initial conditions chosen for the ribbon case, the filled upside down triangle represent the filament case, the filled triangle represent the sheet case and the open circle represent the spherical case.	70
3.4	Kernel function used by GASOLINE for the smoothing and softening profiles. The softening or smoothing chosen here is $h = 50AU$ shown by the dotted line.	71
3.5	Maximal density resolved in function the softening resolution. Our choice of 50 AU is indicated by the dotted lines. The dash-dot lines represent the typical range of density reached by the shocks. The bottom panel shows the minimal Jeans mass we can resolve.	73
3.6	Evolution of the RMS Mach number (top panel) and of the half mass radius (bottom panel) for each simulation: the spherical case (full line), the ribbon case (dotted line), the filament case (dashed line) and the sheet case (dashed dot line). This figure shows how the potential energy is converted during the collapse to maintain or even increase the turbulent kinetic energy. . . .	75
3.7	Evolution of the RMS Mach number (top panel) and of the half mass radius (bottom panel) for the spherical case with RMS Mach number 0.9 (full line), 6.2 (dotted line) and 13.5 (dashed line).	76
3.8	Mach number distribution of the gas particles in function of density. Every particle of the spherical case simulation is plotted on a log-log scale and the 1σ contour lines are over-plotted. The RMS mach number is represented by the dashed line.	78

3.9	Mach number distribution of the gas particles in function of density for the spherical case (top left), the ribbon case (top right), the filament case (bottom left) and the sheet case (bottom right). Every particle of the simulation is plotted on a log-linear scale and the 1σ contour lines are over-plotted. The RMS Mach number is represented by the dashed line.	79
3.10	Density PDF at the final timestep (135 kyr), for each simulations: spherical, ribbon, filament and sheet cases. The dashed lines represent the best fit of a log-normal with mean μ and standard deviation σ , the parameter b is also calculated for each run.	80
3.11	Density PDF evolution for each simulations: spherical, ribbon, filament and sheet cases. The evolution goes from light grey to black and the timesteps represented are 20, 60, 100, 120 and 135 kyr.	82
3.12	The standard deviation of the density PDFs in function of the Mach number for each simulations. The crosses represent the timesteps: 0, 20, 40, 60, 80, 100, 110, 120, 130 and 135 kyr. The dashed line represent the linear fit to the last 6 data points, the slope (b) is also indicated.	83
3.13	Structure functions of the transverse velocities (full line) and the longitudinal velocities (dashed line) for the spherical case. The first (top panel), second (middle panel) and third (bottom panel) order are shown. The bottom axis of each plot is showing the spacing (l) in units of the initial size of the simulation. The best fits to each structure function are over-plotted in grey. . .	88
3.14	Structure functions similar to figure 3.13, but for the ribbon case.	89
3.15	Structure functions similar to figure 3.13, but for the filament case.	90
3.16	Structure functions similar to figure 3.13, but for the sheet case.	91
4.1	Column density maps (500×500 lines of sight) of the spherical case (inner 3.4 pc) seen through the z axis at the final stage (135 kyr). The logarithmic color scale is shown at the bottom, in units of g/cm^2 . The crosses represent all the cores identified by Clumpfind2D and the open circles are cores we looked at in details. The open squares are showing “fake” cores; identified as cores by Clumpfind2D and looked like real cores from the column density map, but they were not when looked in detail in the 3D density distribution.	104

4.2	Column density maps of the filamentary case seen through the y axis similar to Figure 4.1.	105
4.3	Column density maps of the ribbon case seen through the y axis similar to Figure 4.1.	106
4.4	Column density maps of the sheet case seen through the y axis similar to Figure 4.1.	107
4.5	2D maps (200×200 lines of sight) for the Fil5 (CR) core seen through the z axis. The size of the images shown is 56000×56000 AU. The left column is showing the column density, the middle one the mean velocity and right one the velocity dispersion. The 3 rows are for 3 density ranges, on top $\rho_{C^{18}O}$, in the middle $\rho_{N_2H^+}$ and at the bottom ρ_{NH_3} . On the left column the contour line shown is for 90, 75, 50 and 25% of the maximum column density of the ρ_{NH_3} map. On the middle and right hand side columns, the contour lines are the same levels but for the maximum column density at their respective density ranges. .	114
4.6	Same as Figure 4.5 but this time the lines of sight are going through the whole cloud instead of only the 56000 AU cube box.	115
4.7	Same as Figure 4.5 but for the Rib3 (CR) core seen through the x axis. The image size shown is 34000×34000 AU.	116
4.8	Same as Figure 4.7 but this time the lines of sight are going through the z axis. The observed structure is significantly different.	117
4.9	Same as Figure 4.7 but for Fil5, a typical CR core, seen through the x axis. The image size shown is 56000×56000 AU.	118
4.10	Radial profile of the typical CR core Fil5. The top panel shows the radial distribution of velocity dispersion. The bottom panel shows the column density profile. The fit to the density profile for the NH_3 line (labeled as all) is shown by the dotted line. The short dashed vertical line on each panel represent the half-maximum radius ($R_{1/2}$).	119
4.11	Same as Figure 4.5 but for Fil3, a typical CC core, seen through the y axis. The image size shown is 16000×16000 AU.	120
4.12	Same as Figure 4.10, but for Fil3, a typical CC core, seen through the y axis.	121
4.13	Same as Figure 4.5 but for Fil1, a typical N core, seen through the y axis. The image size shown is 20000×20000 AU.	122
4.14	Same as Figure 4.10, but for Fil1, a typical N core, seen through the y axis.	123

4.15	Same as Figure 4.6 but for Rib6, a <i>fake</i> core showing a structure very similar to a dense core, seen through the y axis. The image size shown is 32000×32000 AU.	124
4.16	Same as Figure 4.15 but here the lines of sight went only through a 32000 AU cube box around what looked the most like an object along the line of sight, which is a fairly low density core. The “object” is not seen at all in the $\rho_{N_2H^+}$ density range. The image looks dramatically different from the image 4.15, due to a low density filamentary structure aligned in the line of sight.	125
4.17	Statistical distribution of the density profile parameters. The black histogram is for all the cores, the red one is for N cores, the green one is for CC cores and the blue one is for CR cores.	128
4.18	Mean velocity dispersion inside the cores in function of their size. The observed power-law, from Caselli et al. (2002) data, is also shown (dotted line). The average velocity dispersion for cores smaller than 10000 AU is also shown (dashed line). . . .	135
4.19	Velocity dispersion of density bins for each cores (in grey) and the averaged relation (in black). The range of density included in the fit is indicated by the dashed lines. The linear fit to the mean relation yield a slope $\eta = -0.222$. The total number of particles per density bin is shown in the bottom panel.	137
4.20	Velocity dispersion of density bins for the CR cores (in grey) and the averaged relation (in black), similar to Figure 4.19. The linear fit to the mean relation yield a slope $\eta = -0.253$. .	138
4.21	Velocity dispersion of density bins for the CC cores (in grey) and the averaged relation (in black), similar to Figure 4.19. The linear fit to the mean relation yield a slope $\eta = -0.203$. .	139
4.22	Velocity dispersion of density bins for the N cores (in grey) and the averaged relation (in black), similar to Figure 4.19. The linear fit to the mean relation yield a slope $\eta = -0.160$	140
4.23	Distribution of the measured gradients for the $\rho_{C^{18}O}$ (left) and the $\rho_{N_2H^+}$ (right) density ranges of the 19 cores in the 3 perpendicular directions (x, y, z).	143
4.24	Comparison of the velocity gradients measured for each core in the density ranges $\rho_{C^{18}O}$ and $\rho_{N_2H^+}$. The straight line represent the case where both gradients are identical.	144
4.25	Distribution of the measured rotation energy ratio in the $\rho_{C^{18}O}$ (left) and the $\rho_{N_2H^+}$ (right) ranges.	145
4.26	Comparison of the rotation energy ratios measured for each core in the density ranges $\rho_{C^{18}O}$ and $\rho_{N_2H^+}$. The straight line represent the case where both ratios are identical.	146

4.27	Specific angular momentum in function of size (top panel) for each core from 3 perpendicular perspectives. The best linear fit to the data is shown (full line) and also the observed relation by Goodman et al. (1993) $J/M \propto R^{1.6}$ (dotted line). The angular momentum in each direction (x,y,z) have been calculated using the 2D maps of mean velocity for the low density tracers ($\rho_{C^{18}O}$), using a similar technique to Goodman et al. (1993). From the measured velocity gradients (middle panel), we calculated the specific angular momentum ($\nabla v \approx 5(J/M)/2R^2$) and compared to the observed relation $\nabla v \propto R^{-0.4}$ (dotted line). On the bottom panel we plotted the rotation energy ratio, $\beta_{rot} = E_{rot}/E_{grav}$ for which no significant slope is observed.	148
4.28	Same as Figure 4.27, but for the medium density range ($\rho_{N_2H^+}$).	149
4.29	Same as Figure 4.27, but for the high density range (ρ_{NH_3}).	150
4.30	Same properties shown in Figure 4.27, but here the specific angular momentum is calculated directly from the sum of all the core particles. We then calculated the velocity gradient and rotation energy ratio from the same formulas used previously.	151
4.31	Difference in the mean velocity (on the line of sight) of the cores in $\rho_{C^{18}O}$ and $\rho_{N_2H^+}^+$. We fitted a Gaussian to the data, shown by the dashed line, with $\sigma = 0.22$. The dotted lines represent the speed of sound, showing that very few cores have supersonic velocities with respect to their envelope.	153
4.32	The virial mass ($M_{vir} = 210R[pc]\Delta_{eff}^2[km/s]$) of the cores is plotted as a function of $M_{1/2}$. The equipartition ($M_{1/2} = M_{vir}$) is shown by the full line. Departure from equipartition by a factor 3, 10 and 30 are shown by the dashed lines. The cores below the dotted line are bound.	156
4.33	The CMF of the cores found with Clumpfind 2D, we combined the cores found in each simulation to get sufficient statistics. We also plotted the Salpeter power-law ($M^{-2.35}$) (dashed line), a log-normal fit to the data with Poisson statistical weighting (full line) and the Chabrier (2005) logarithmic multiple systems IMF (dotted line).	158
4.34	CMF for each simulation at the final time step (135 kyr). The dashed line represents the breaking point between the double power-law relation and the best fit power-laws are also shown. The resulting CMF from combining the CMF of each simulation are shown (thick line) and also its log-normal fit (dotted line).	160

4.35	Virial mass of the 3D density group cores is plotted in function of their mass. The lines are the same as the one shown in Figure 4.32.	161
4.36	CMF of the bounded cores (dashed lines) compared to the total CMF (full lines) for each simulation.	162
4.37	CMF of the combined bounded cores (dashed lines) with the log-normal fit (dotted line).	163
4.38	Mass of the cores integrated along the whole line of sight ($M_{1/2}^{all}$), in function of the real mass of the cores ($M_{1/2}^{cut}$). The “+” represent the “real” cores from 3 orthogonal directions (x, y, z). Similarly, the “fake” cores are represented by the open diamonds. The dotted line shows equal masses, the full line an overestimation by a factor 2 and the dashed line a factor 6.	165

List of Tables

2.1	List of the multiple systems found after 220 000 yr ($1.16t_{ff}$) and their statistics. The masses are in solar masses, Q is the mass ratio ($Q = M_{primary}/M_{secondary}$) and a is the semi-major axis in AU. The binary systems marked with a * are part of a larger system.	35
2.2	List of the multiple systems found same as table 2.1, but after 235 000 yr ($1.25t_{ff}$).	36
2.3	List of the changes in the systems, between 220 kyr and 235 kyr. The bold stars moved from one binary system to a different one.	36
3.1	List of the fit to the slopes of the transverse (ζ_p^\perp) and longitudinal (ζ_p^\parallel) structure functions ($p = 1, 2$ and 3) for the initial and final stage of each simulations.	84
4.1	Properties of the compact regions, \bar{D} is the average diameter of the object, M is the total mass and $\bar{\rho}$ is the average density.	111
4.2	Properties of the centrally concentrated objects, \bar{D} is the average diameter of the object, M is the total mass and $\bar{\rho}$ is the average density.	111
4.3	Properties of the nucleus, \bar{D} is the average diameter of the object, M is the total mass and $\bar{\rho}$ is the average density.	112
4.4	Mean values and standard deviations of the density profile fit parameters for all cores and for every core type.	127
4.5	Properties and fitting parameters for every core we looked at in details, from the 3 different angles.	129
4.5	Properties and fitting parameters for every core we looked at in details, from the 3 different angles.	130
4.5	Properties and fitting parameters for every core we looked at in details, from the 3 different angles.	131

4.5	Properties and fitting parameters for every core we looked at in details, from the 3 different angles.	132
4.6	List of the fit to the $\log \sigma - \log \rho$ relation for each core type. The parameters are for a linear fit with $A + Bx$, where the 1σ uncertainty are for the fit of the averaged relation weighted by the total number of particles in each density bin ($1/\sqrt{N_{\rho_i}}$).	138

Chapter

1

Introduction

Stars form in galaxies where the gaseous interstellar medium (ISM) is compressed to high densities. The ISM is the matter (gas and dust) within a galaxy filling the gap between the stars. It composes approximately 10 – 15% of the total mass of the galactic disc and it is mostly concentrated along the spiral arms (Ferrière, 2001). The ISM itself is composed of a wide range of density and temperature, which is generally subdivided in three different phases (Cox, 2005). There is the hot low-density phase ($T \geq 10^5 K$, $n \leq 0.01 \text{ cm}^{-3}$) associated with supernovae ejecta, the warm intermediate phase ($T \approx 4 - 6000 K$, $0.01 \leq n \leq 10 \text{ cm}^{-3}$) either ionized (WIM) or neutral (WNM) and the cold neutral phase ($T \leq 100 K$, $n \geq 10 \text{ cm}^{-3}$).

What could be considered as a fourth colder phase ($T \approx 15 K$, $n \approx 100 - 300 \text{ cm}^{-3}$), on a much smaller scale, is known as giant molecular clouds (GMC), where molecules form. These are often found grouped into large GMC complexes ($\sim 10 - 60 \text{ pc}$, $10^4 - 10^6 M_\odot$) composed of gas and dust. There are thousands of such objects located mostly in the spiral arms of the Milky Way

(e.g. Orion-Monoceros, Taurus-Auriga-Perseus, W51, W3, M17). GMCs are clumpy and the dense regions are known as molecular clouds (MC). MCs are significantly smaller ($\sim 2 - 20 pc$) and denser ($n \approx 10^2 - 10^4 cm^{-3}$). They are also slightly cooler ($T \approx 10K$) and in the mass range of $10^2 - 10^4 M_{\odot}$. Examples of such objects are Taurus, Ophiuchus, Musca, L1641, L1630, W33, W3A, B227, L1495 and L1529. All contemporary star formation is occurring in molecular clouds (Blitz, 1993; Williams et al., 2000), so a better understanding of their observable properties (e.g. Zuckerman & Evans (1974); Leisawitz (1990); Sodroski (1991); May et al. (1997)) theoretical formation mechanisms and evolution (Ballesteros-Paredes et al., 1999; Hartmann et al., 2001; Pringle et al., 2001; Hartmann, 2003; Vázquez-Semadeni et al., 2005; Mouschovias et al., 2006; Krumholz et al., 2006; Bonnell et al., 2006; Elmegreen, 2007; Shetty & Ostriker, 2008; Tasker & Tan, 2008) and of their fragmentation process (Boss, 1998; Klessen et al., 1998; Krumholz et al., 2005; Bonnell & Bate, 2006; Bonnell et al., 2008; Bate, 2009) is essential to understand star formation.

The study of star formation is the study of the processes by which the low density gas of the interstellar medium (ISM) can transform into objects as dense as a stars. The wide range of density involved makes it a very challenging topic of contemporary astrophysics. The field can even be separated in two ranges of scales: microphysics and macrophysics of star formation (McKee & Ostriker, 2007). The former is about the details of how individual stars or binary systems forms from a single dense core of molecular gas. However, most stars are formed in large molecular clouds, in dense environment called *clumps*, that can fragment into multiple cores to form a stellar cluster (Lada & Lada, 2003). The macrophysics of star formation is the study of these environmental effects on the formation of stellar systems at the level of cores. The focus of

this thesis is on the latter scales.

Molecular clouds are large aggregation of molecular gas, dominated by the H_2 molecule. This is their fundamental difference with the rest of the ISM, typically dominated by atomic H (Ferrière, 2001). The molecules can accumulate in these clouds because of the presence of dust grains. Dust grains absorb optical wavelengths shielding the cloud from the heating effect of the external radiation present in the ISM. This way the temperature of these clouds is kept low ($\sim 10\text{K}$, Masunaga & Inutsuka (2000)). This feature also gave them the alternative name of “dark cloud”, since they appear as opaque objects in visual wavelengths. Also, GMCs are dense enough that self-gravity is now important for the dynamics of the gas.

In the last decade or so, key progress has been made on both the theoretical and observational fronts of star formation. On the theoretical perspective, a new paradigm has made an appearance (Mac Low & Klessen, 2004; Ballesteros-Paredes et al., 2007). The presence of supersonic turbulence in molecular clouds is now thought to play the central role, instead of gravity, in the fragmentation process of molecular clouds into multiple dense objects. These dense objects, if gravitationally bounded, can then evolve into stars. One of the key successes of this theory is that it naturally explains the mass distribution of forming stars as a consequence of turbulence.

On the observational side, star forming regions are now routinely observed in the infrared, sub-millimeter or millimeter wavelengths. The recent development of sensitive continuum and heterodyne detectors allowed significant progress (Bergin & Tafalla, 2007) especially in the observations of dense cores (di Francesco et al., 2007; Ward-Thompson et al., 2007; André et al., 2008; Kirk et al., 2007). These objects are dense regions in the molecular

clouds, where stars are thought to form. These observations can now provide key information on the initial conditions of star formation.

Observations have refined the dense core classification (André et al., 2008) to an evolutionary sequence: *starless cores*, *prestellar cores* to “*Class 0*” *protostellar cores*. This is the generally accepted dense core nomenclature, this is also the one we will use throughout this thesis.

Starless cores are starless concentration of molecular gas and dust. They can be observed with tracers like $C^{18}O$ and NH_3 or dust extinction. They do not show infall motion and are thought in certain theoretical paradigms to be mostly transient objects, easily disrupted. Most of them end up as “failed cores”, they get dispersed and never form a star, but some of them evolve to prestellar cores.

Prestellar cores are similar to starless cores, but denser and more centrally-concentrated. They are self-gravitating and therefore unlikely to be transient like starless cores. They are also starless, but usually have infall motions. They are observed with (sub)millimeter dust continuum emission, in absorption in mid to far infrared and denser molecular gas tracers like: NH_3 and N_2H^+ . Class 0 protostellar cores contain an accreting protostar, but can still be considered as cores since most of the mass of the system is still in the surrounding envelope. As most of the protostellar envelope is dissipated by accretion or ejection, the object become of Class I, II and III proto-star.

More specifically, the aim of this thesis is to study star formation in its natural clustered environment. The complex dynamic of the fragmentation process and the gravitational interactions of the gas in clustered environment is best studied, from a theoretical perspective, with simulations. To study these complex dynamics, we used a Smoothed Particle Hydrodynamics (SPH)

code, GASOLINE (Wadsley et al., 2004).

Our starting point was to reproduce the “state of the art” Smoothed Particles Hydrodynamics (SPH) simulations at the time (Bate et al., 2003), that had a large impact in the field. These simulations studied star formation within star clusters using a special technique. They used “sink particles” to put dense gas particles on or below a set physical scale, slowing down the simulation, in a single particle. We implemented this type of particle in GASOLINE, and ran a simulation with a similar set of parameters. We present the results of this simulation in chapter 2. We found a good general agreement with Bate et al. (2003). However, this work raised increasing concerns about some of the approximations used to follow the fragmentation process over so many orders of magnitude in density. Our first issue was with the barotropic equation of state used to simulate gas of density exceeding $\approx 2.56 \times 10^{10} \text{cm}^{-3}$ that we believe would require some form of radiative transfer to be reliable. We also had concerns about the sink particles themselves, potentially overestimating the accretion rates.

Dense cores have typical densities in the range $\approx 10^4 - 10^5 \text{cm}^{-3}$ (Bergin & Tafalla, 2007). In this density range, the molecular gas is able to cool efficiently and remain at a temperature very close to $\approx 10\text{K}$ (Masunaga & Inutsuka, 2000). The isothermal approximation in this context is then well justified. We therefore chose to simulate the formation of cores within molecular clouds and to consider only the prestellar phase, before stellar feedback could have a large influence. We are confident that the physics in the density range involved can be reliably accounted for. We didn’t use sink particles, on purpose, so that the cores structure can be well resolved down to the resolution of the simulation.

We studied the evolution of turbulence in our simulations (chapter 3). Supersonic turbulence is known to decay rapidly (Mac Low et al., 1998) with and without the presence of magnetic fields. Similar results were also obtained including self-gravity (Tilley & Pudritz, 2004). However these studies are based on grid codes for periodic boxes. Our simulations are not periodic; they have open boundaries. Therefore the gravitational collapse can occur for the whole molecular cloud, not only for small portions of it. Hence the picture we observe in our self-gravitating turbulent molecular clouds is different. We found that under gravitational collapse turbulence is naturally developed and maintained with properties in good agreement with the current observational and theoretical pictures.

We also compared the cores we formed this way with observations in chapter 4. We looked at several observable properties of cores: density profiles, velocity dispersion and rotation of the cores, core-core velocity dispersion, core-envelope velocity dispersion, velocity dispersion vs. core size relation and the core mass function. From this we could identify which observed features can be reproduced well with isothermal hydrodynamics simulations. We found a good general agreement between our simulated and observed cores, which indicates that extra physics like magnetic fields, outflows, proper equation of state or radiative transfer would have only secondary effects at this formation stages, or would tend to cancel each other.

Bibliography

André, P., Basu, S., & Inutsuka, S.-i. 2008, ArXiv e-prints, 801, arXiv:0801.4210

Bate, M. R., Bonnell, I. A., & Bromm, V. 2003, MNRAS, 339, 577

Bate, M. R. 2009, MNRAS, 392, 1363

Ballesteros-Paredes, J., Hartmann, L., & Vázquez-Semadeni, E. 1999, ApJ, 527, 285

Ballesteros-Paredes, J., Klessen, R. S., Mac Low, M.-M., & Vazquez-Semadeni, E. 2007, Protostars and Planets V, 63

Bergin, E. A., & Tafalla, M. 2007, ARA&A, 45, 339

Blitz, L. 1993, Protostars and Planets III, 125

Bonnell, I. A., Dobbs, C. L., Robitaille, T. P., & Pringle, J. E. 2006, MNRAS, 365, 37

Bonnell, I. A., & Bate, M. R. 2006, MNRAS, 370, 488

Bonnell, I. A., Clark, P., & Bate, M. R. 2008, MNRAS, 389, 1556

Boss, A. P. 1998, *ApJ*, 501, L77

Cox, D. P. 2005, *ARA&A*, 43, 337

di Francesco, J., Evans, N. J., II, Caselli, P., Myers, P. C., Shirley, Y., Aikawa, Y., & Tafalla, M. 2007, *Protostars and Planets V*, 17

Elmegreen, B. G. 2007, *ApJ*, 668, 1064

Ferrière, K. M. 2001, *Reviews of Modern Physics*, 73, 1031

Hartmann, L., Ballesteros-Paredes, J., & Bergin, E. A. 2001, *ApJ*, 562, 852

Hartmann, L. 2003, *ApJ*, 585, 398

Kirk, H., Johnstone, D., & Tafalla, M. 2007, *ApJ*, 668, 1042

Klessen, R. S., Burkert, A., & Bate, M. R. 1998, *ApJ*, 501, L205

Krumholz, M. R., McKee, C. F., & Klein, R. I. 2005, *Nature*, 438, 332

Krumholz, M. R., Matzner, C. D., & McKee, C. F. 2006, *ApJ*, 653, 361

Lada, C. J., & Lada, E. A. 2003, *ARA&A*, 41, 57

Leisawitz, D. 1990, *ApJ*, 359, 319

Mac Low, M.-M., Klessen, R. S., Burkert, A., & Smith, M. D. 1998, *Physical Review Letters*, 80, 2754

Mac Low, M.-M., & Klessen, R. S. 2004, *Reviews of Modern Physics*, 76, 125

Masunaga, H., & Inutsuka, S.-i. 2000, *ApJ*, 531, 350

May, J., Alvarez, H., & Bronfman, L. 1997, *A&A*, 327, 325

- McKee, C. F., & Ostriker, E. C. 2007, *ARA&A*, 45, 565
- Mouschovias, T. C., Tassis, K., & Kunz, M. W. 2006, *ApJ*, 646, 1043
- Pringle, J. E., Allen, R. J., & Lubow, S. H. 2001, *MNRAS*, 327, 663
- Shetty, R., & Ostriker, E. C. 2008, *ApJ*, 684, 978
- Sodroski, T. J. 1991, *ApJ*, 366, 95
- Tasker, E. J., & Tan, J. C. 2008, arXiv:0811.0207
- Tilley, D. A., & Pudritz, R. E. 2004, *MNRAS*, 353, 769
- Vázquez-Semadeni, E., Kim, J., Shadmehri, M., & Ballesteros-Paredes, J. 2005, *ApJ*, 618, 344
- Wadsley, J. W., Stadel, J., & Quinn, T. 2004, *New Astronomy*, 9, 137
- Ward-Thompson, D., André, P., Crutcher, R., Johnstone, D., Onishi, T., & Wilson, C. 2007, *Protostars and Planets V*, 33
- Williams, J. P., Blitz, L., & McKee, C. F. 2000, *Protostars and Planets IV*, 97
- Zuckerman, B., & Evans, N. J., II 1974, *ApJ*, 192, L149

Chapter 2

Star Cluster Formation

2.1 Introduction

Most stars form in clusters within cores of molecular gas ($0.1 - 10 M_{\odot}$, $n > 10^4 \text{ cm}^{-3}$, Mac Low & Klessen (2004); Bergin & Tafalla (2007)). The fragmentation processes of these cores often leads to binary or multiple systems and is not yet fully understood, but has been widely studied numerically (see Bodenheimer et al., 2000, for a review).

To study interactions between stars as they are forming and to get a statistical sample of the properties of the stellar systems formed, it is useful to simulate the collapse and fragmentation of a whole clump ($10 - 1000 M_{\odot}$, $n \approx 10^3 - 10^5 \text{ cm}^{-3}$)(Mac Low & Klessen, 2004; Bergin & Tafalla, 2007). Such simulations allow study of the initial mass function (IMF), the multiplicity of star formation, the star formation efficiency and the stellar velocity dispersion. The complex dynamics of the fragmentation process and the gravitational in-

interactions of the gas and the stars in a clustered environment can be well studied computationally using smooth particle hydrodynamics (SPH). One of the advantages this particle based method offers over grid based methods is that as the gas density increases, the particle density is also naturally increasing. This insures the resolution of the simulations is automatically adjusted with the gas density, without requiring explicit refinement. Also SPH allows us to easily use non-periodic boundary conditions, which enables us to simulate a whole molecular clump instead of only a periodic box representing a sub-section of the clump.

We performed SPH simulations of the collapse of a turbulent clump typical of what is found in molecular clouds. We used similar parameters to the ones used by Bate et al. (2003), henceforth BBB3, to use as a benchmark, since BBB3 uses a SPH code similar to ours. This was the logical first step towards making more realistic star formation simulations by including more physics like stellar feedback or mergers. BBB3 simulations of star clusters were the first to follow the collapse and fragmentation of a large scale turbulent molecular gas cloud and resolve beyond the opacity limit for fragmentation. These simulations spawned a debate (Krumholz et al., 2005) on the mechanism of massive stars formation, by suggesting the presence of competitive accretion (Bonnell & Bate, 2006). We describe this model in section 2.1.1.

We aim to reproduce those results. In section 2.1.2, we review core collapse theory, which leads to the definition of an equation of state (section 2.1.3). In section 2.2 we describe briefly our SPH code and the sink particles we implemented. Section 2.2.1 describes the initial conditions used and how we created the initial turbulence. The results are presented in section 2.3, we show a simple test of the sinks in section 2.4 and then conclude in section 2.5.

2.1.1 Fragmentation Models

A key challenge to star formation theory is how to reproduce the initial mass function (IMF). There is currently a debate in the star formation community between 2 different models of fragmentation: competitive accretion and turbulent fragmentation. These models should be able to reproduce the right number of low and high mass stars to fit the IMF.

Competitive accretion postulates that low mass stars ($0.5 M_{\odot}$) are formed early via gravitational fragmentation within cores and then compete to accrete the available surrounding gas (Bonnell & Bate, 2006; Bonnell, 2008). In this scenario, stars at the center of cloud's gravitational potential accrete the most gas and form massive stars because more gas is available to them. This model is supported by simulations (Bate et al., 2003) that successfully produce IMFs in good agreement with observations for the high mass end. However, Krumholz et al. (2005) argue that the rates of accretion required by this model are inconsistent with observations.

Turbulent fragmentation, sometimes referred to as *gravitational collapse* (Krumholz et al., 2005) posits that turbulence creates gravitationally unstable over-dense regions (cores) with the appropriate mass distribution. These cores collapse and form stars with masses proportional to the original core mass. This model is supported by the observed similarity between the core mass function and the IMF (Motte et al., 1998; Alves et al., 2007). However, it is currently unknown which physical process prevents massive cores from fragmenting into lower mass stars as they accumulate their mass (Dobbs et al., 2005).

The main difference between the 2 models is *when* the mass is accumu-

lated, in the pre-stellar period by turbulence or after the initial core is formed via accretion.

2.1.2 Protostellar Collapse

The initial stages of protostellar collapse have been studied with 1-D radiative transfer models (Masunaga et al. (1998); Masunaga & Inutsuka (2000); Stamatellos et al. (2007)) that provide key information on the initial stages of star formation. The following description of dense core collapse is based on this work and is summarized in Figure 2.1.

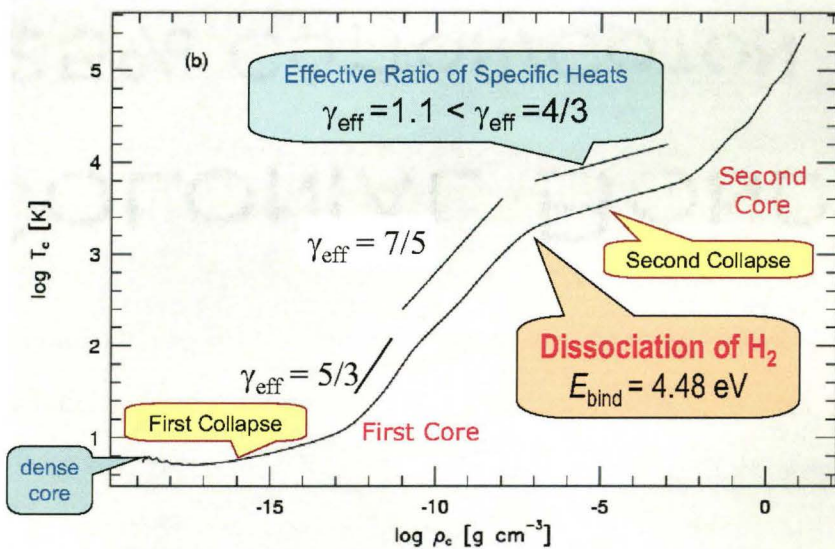


Figure 2.1 Central temperature evolution with central density from Masunaga & Inutsuka (2000), modified by Andre et al. (2008).

Initially, in the density range 10^{-18} g/cm⁽³⁾ $\leq \rho \leq 10^{-13}$ g/cm³, molecular clouds can radiate away their thermal energy very efficiently by infrared thermal emission from dust grains and line cooling. These dust grains also

absorb optical wavelengths shielding the cloud from the heating effect of the external radiation present in the ISM. This enables the cloud to reach thermal equilibrium with the heating by the external radiation and cosmic rays (Masunaga & Inutsuka (2000)). So, at the initial stage, isothermality is generally recognized as a very good approximation. But, during protostellar collapse, the gravitational energy released by the collapse also contributes to the heating. Detailed consideration of those energy sources using 1-D radiative transfer calculations (Masunaga & Inutsuka (2000); Stamatellos et al. (2007)) revealed only small variations around isothermality $T = 5(\rho_{18})^{0.08}$ K, where $\rho_{18} = \rho/10^{-18}$ g/cm³. Those variations are also in agreement with the Larson (2005) relation $T = 4.4 \text{ K}(\rho_{18}^{0.07})$ for 10^{-18} g/cm³ $\leq \rho \leq 10^{-13}$ g/cm³. Over 5 orders of magnitude in density, the temperature variations are limited to the range $4.4 \text{ K} \leq T \leq 12.6 \text{ K}$. Therefore, the isothermal ($\sim 10 \text{ K}$) approximation in this density range is well justified.

As the collapse proceeds beyond 10^{-13} g/cm³, however, the temperature in the central region begins to increase. As the central density increases the optical depth also increases and the adiabatic heating begins to dominate over radiative cooling. The temperature increase provides sufficient gas thermal pressure support to halt gravitational collapse. This central adiabatic equilibrium is called the “first core”. The increase of the central temperature is related to the central density by the ratio of specific heats, in the $10 \text{ K} < T < 100 \text{ K}$ regime: $\gamma_{eff} = C_P/C_V = 5/3$, where $p = K\rho^{\gamma_{eff}}$, $K = c_s^2$ and c_s is the sound speed. Since $p \propto T/\rho$, $T(\rho) \propto \rho^{2/3}$, this is the typical behavior of monoatomic gas. At this low temperature, the rotational degree of freedom of molecular hydrogen is not excited ($E_{J=0-2}/k_B = 512 \text{ K}$), so H_2 does not radiate and behaves like an ideal gas. The collapse becomes completely adiabatic

once $T > 10^2$ K, with the effective adiabatic exponent, $\gamma_{eff} = 7/5$, typical of a diatomic molecule.

A gas with any γ_{eff} can collapse, but if $\gamma_{eff} > 4/3$ the collapse is halted at virial equilibrium and for $\gamma_{eff} < 4/3$ the gas pressure can never support its own gravity. In these two regimes $\gamma_{eff} > 4/3$, but the virial equilibrium is not reached and the gas pressure is insufficient to support the core against self-gravity. However, the collapse is significantly decelerated and the first core has a lifetime of $\sim 10^3$ yr.

When the first core reaches central temperatures of ≈ 2000 K, at $\rho_c \approx 10^{-12}$ g/cm⁻³, the molecular hydrogen begins to dissociate. This process consumes the released gravitational energy such that the thermal pressure cannot slow the self-gravitational collapse anymore. The effective adiabatic exponent becomes $\gamma_{eff} \sim 1.1$ (Masunaga & Inutsuka (2000)) and the core goes into a second phase of collapse, until the molecular hydrogen is exhausted.

In the second collapse the central density increases to reach a stellar value ($\rho_c \sim 1$ g/cm³). A second stable equilibrium is then reached and a second core, a real hydrostatic protostar, is born. The effective adiabatic exponent after the second collapse gets steeper, but the expected value for monoatomic gas, $\gamma_{eff} = 5/3$, is never reached because the partial electron degeneracy has a significant effect on the central pressure (Masunaga & Inutsuka (2000)). The timescale to reach the second collapse is of the order of the free-fall time (see Figure 2.2).

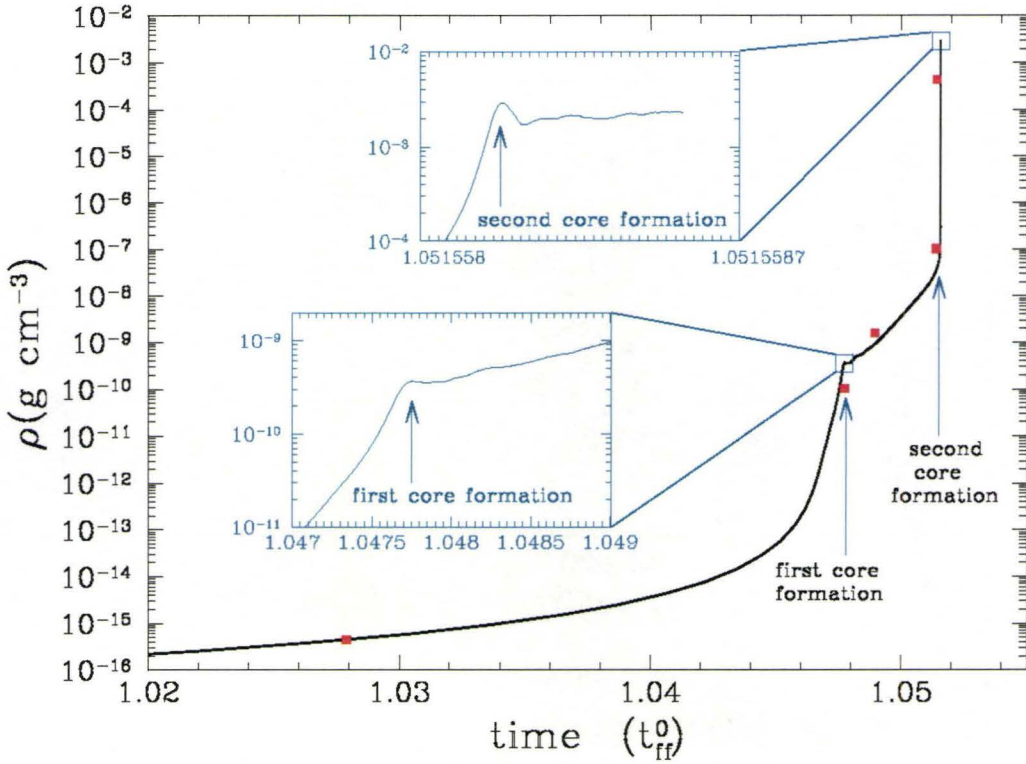


Figure 2.2 Timescale for the evolution of the central density, in units of free fall time $t_{ff}^0 = 1.781 \times 10^5 \text{yr}$ (Stamatellos et al. (2007)). The red dots are a comparison to the Masunaga & Inutsuka (2000) calculations.

2.1.3 Equation of state

Full 3-D radiative transfer would be required to calculate the exact temperature everywhere in a molecular cloud. But BBB3 used a simple barotropic equation of state, developed by Bonnell (1994) and Bate (1998), reproducing reasonably well the main features of the 1-D radiative transfer hydrodynamic calculations of Masunaga & Inutsuka (2000) (see Figure 2.3). It assumes low density gas is isothermal (10K) and higher density gas follows the barotropic equations

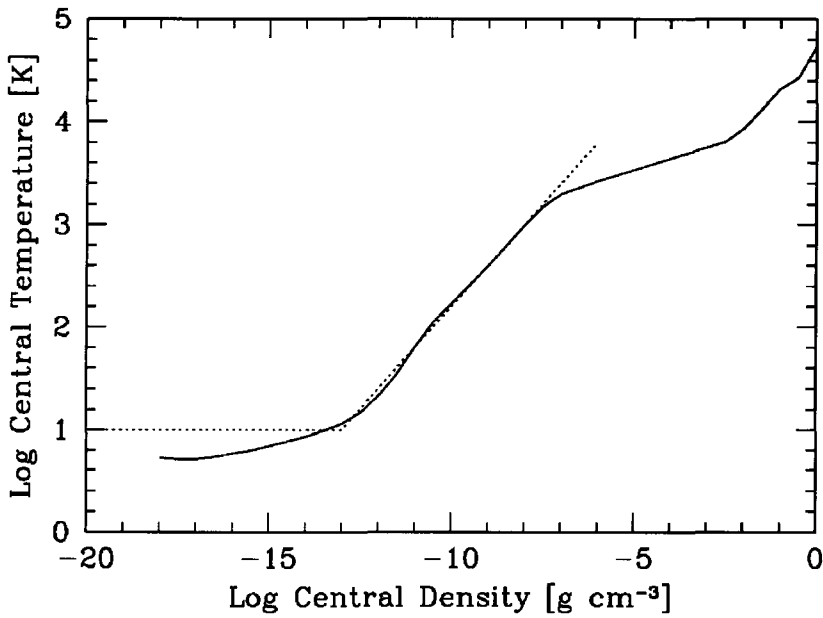


Figure 2.3 Barotropic equation of state (dotted line) compared to Masunaga & Inutsuka (2000) calculations (full line), from Bate et al. (2003).

$$P = \begin{cases} K_1 \rho & : \rho \leq 10^{-13} \text{ g/cm}^3 \\ K_2 \rho^{7/5} & : 10^{-13} < \rho \leq 10^{-7.24} \text{ g/cm}^3 \\ K_3 \rho^{1.15} & : 10^{-7.24} < \rho \leq 10^{-3} \text{ g/cm}^3 \\ K_4 \rho^{5/3} & : \rho > 10^{-3} \text{ g/cm}^3 \end{cases}$$

where K_1 , K_2 , K_3 and K_4 are set such that the pressure is continuous at $\rho = 10^{-13}$, $10^{-7.24}$ and 10^{-3} g/cm³ respectively.

While the barotropic equation of state greatly reduces the complexity of the computation, Figure 2.4 shows the fit is not exact. Stamatellos et al. (2007) found that the center of the core begins heating at 10^{-15} g/cm³ after their model has evolved for $1.05t_{ff}$ rather than 10^{-13} g/cm³ as assumed in the barotropic model. A similar result was found in Whitehouse & Bate (2006), where they conclude that simple barotropic equations of state like this provide

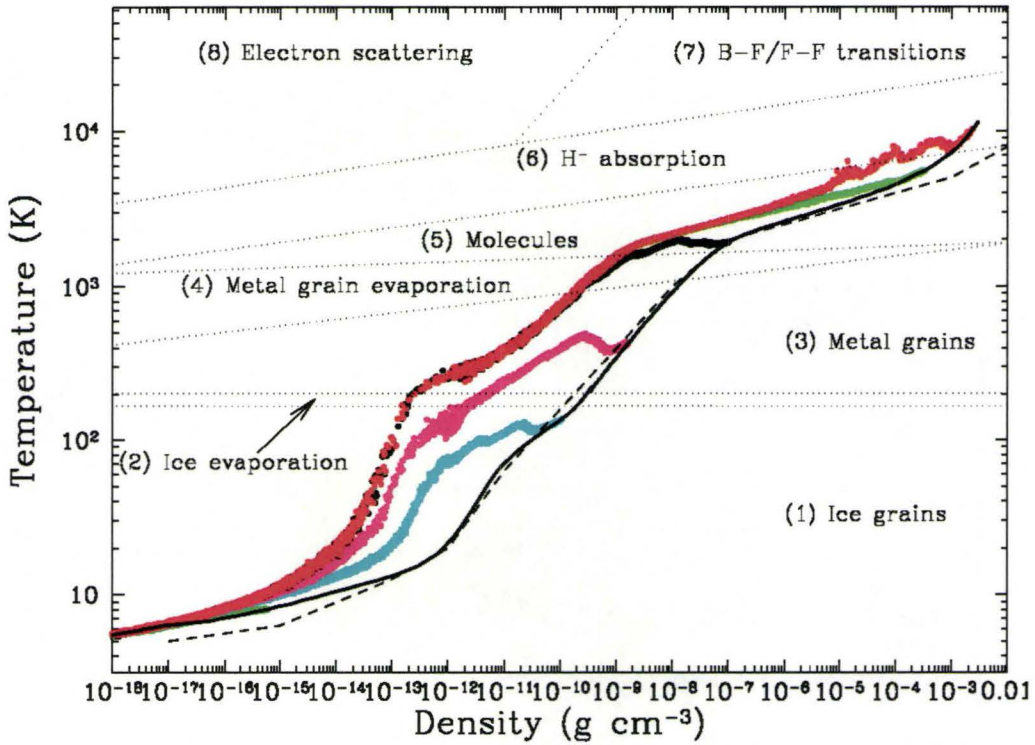


Figure 2.4 Temperature vs. density at different time steps from Stamatellos et al. (2007). The lines show the time evolution from the thin black line ($0.843t_{ff}$) to cyan, magenta, black, green to red ($1.05156t_{ff}$). At later stages the regions around the center heat up at much lower density. The dotted line is to compare to Masunaga & Inutsuka (2000).

a crude approximation, at best, of the thermal behaviour of the gas. The temperature even at the maximum density is underestimated by a factor 2-3 and the difference would go over an order in magnitude in other regions. This temperature inaccuracy would directly affect the Jeans mass ($M_J \propto T^{3/2}$) and destroy the credibility of the simulated fragmentation. Thus, full 3D radiative transfer calculations are necessary for a more realistic picture of stellar scale fragmentation.

However, such calculations are currently computationally unpractical. The simple barotropic equation of state gives a reasonable first approximation

to follow collapse through ~ 2 more orders of magnitude in density better than a simple isothermal equation of state. However, the barotropic equation of state prevents proper heating at shocks. Therefore, we note that this approximation could have large effects on the final result, especially on the detailed fragmentation process.

2.1.4 BBB3 code

Bate used the SPH code described in Bate et al. (1995) based on the original version developed by Benz (Benz (1990); Benz et al. (1990)). The smoothing lengths in SPH simulations defines the size of the particles. They are variable in space and time in order to keep an approximately constant number (~ 50) of neighbour particles. The SPH equations are integrated using a second-order Runge-Kutta-Fehlberg integrator using individual time steps for each particles (Bate et al. (1995)). The gravitational forces between a particle and its close neighbours are calculated using a binary tree.

2.1.5 Sink particles

As density rises in SPH, the Courant condition (or CFL for Courant-Friedrichs-Lewy) (Courant et al., 1928) for numerical stability ($\Delta t \leq \Delta x/v_0$ in 1D, where v_0 is the maximum velocity and Δx is the particle spacing) demands that timesteps become smaller to maintain numerical accuracy and the simulation slows considerably. Bate et al. (1995) created sink particles in SPH to remove gas particles with the highest densities and replace them with a star particles interacting with gas only by gravity. Sink particles are created when gas particles reach a threshold density ($\rho_{threshold} = 10^{-11}$ g/cm³). This threshold

is chosen to be 2 orders of magnitude denser than the point where a fragment leaves isothermality, to ensure that the fragment is self-gravitating and centrally condensed. These 2 orders in density range minimize the possibility of defining fragments that would merge or would be disrupted by dynamical interactions as sinks.

The newly formed sink particle combines the mass and momentum of all the gas particles located within the set sink radius (5 AU). 50 gas particles must be located within the sink radius to allow the sink particle to form. The sink particle accretes in-falling gas particles when they cross the sink radius if they satisfy the following binding criteria:

$$E_{Grav} + E_{Thermal} + E_{kinetic} < 0 \quad (2.1)$$

$$E_{thermal} \leq \left| \frac{E_{Grav}}{2} \right| \quad (2.2)$$

Bate et al. (1995) require boundary conditions around sink particles in order to avoid any effect on the evolution of the gas outside of it. Without these, the discontinuity in particle number at the sink radius affects pressure and viscous forces. Without pressure support, particles are artificially drawn towards the sink particle. The left hand side of Figure 2 in Bate et al. (1995) clearly demonstrates this problem. There is an artificial density drop near the sink and an artificial radial pressure pushing the particles towards the sink. Bate et al. (1995) tried several boundary conditions, and managed to fix the key issues of the density profile and pressure (see their Figure 2, right hand side). However no single boundary conditions could fix all the problems at once. We note that the boundary condition issues were neglected in each of

Bate’s later simulations (including BBB3) using the assumption that the gas accretion onto the sink is mostly supersonic. He claims that the “void” effect of the sink particle does not propagate or have large scale effects on the gas dynamics. Our star cluster simulation did not employ any special boundary conditions for sink particles either.

Neither we or BBB3 allowed sinks to merge. Merging stars might form more massive stars, if it occurred frequently. It could also reduce the number of strong gravitational interactions leading to artificially large velocity dispersions.

Commerçon et al. (2008) investigated the macroscopic side effects of sink particles by running protostellar collapse simulations using three threshold densities, $\rho_{threshold} = 10^{-10}, 10^{-11}$ and 3×10^{-12} g/cm³. Their Figure D.1 shows snapshots of these simulations at two different time steps. At the later time, no sink particles form using the highest density threshold, one forms using the medium threshold and 9 form using the lowest threshold. Their Figure D.1 shows that a single sink particle forming at the density threshold used in the BBB3 simulations has significant effects on the gas dynamics, even at long range (~ 100 AU) compared to the sink radius (5 AU).

Sink particles provide an efficient means to follow the collapse of large gaseous objects. It is currently essential to use some numerical trick to prevent high densities from grinding the simulation to a halt. However, to be fully trusted, a reliable boundary condition needs to be developed. We discuss more tests of sinks in section 2.4.

2.2 Methods

The simulations run here used the parallel SPH code GASOLINE (Wadsley et al. (2004)) to which we added sink particles (see section 2.1.5). The SPH method calculate the evolution of a fluid whose properties are represented by particles. The local properties of the fluid can be measured by a summation over the neighboring particles weighted by a smoothing kernel (see section 2.4 for more details). The gravitational forces between a particle and its close neighbours are calculated using a binary tree. And the hydrodynamics of the gas is calculated by solving the Euler's equations in the Lagrangian form. Gasoline uses a symplectic integration scheme named Kick-Drift-Kick as described in Quinn et al. (1997). It uses a neighbour finding method based on the smooth algorithm, developed by Stadel ¹, to locate the nearest $N_{neighbour}$ for each particle. This method has been parallelized to find non-local neighbours. The SPH interaction distance, $2h_i$, is fixed by the $N_{neighbour}^{th}$ neighbour distance from the i^{th} particle. One significant difference between GASOLINE and Bate's code is that GASOLINE uses a fixed number of neighbours, while Bate et al. (2003) allow the number of neighbours to vary. See section 2.4 for a discussion of the effects of such difference.

2.2.1 Initial conditions

Our initial model was configured to match BBB3 as a means of comparison between the two SPH solving algorithms. The model consisted of a $50 M_{\odot}$ uniform density ($3 \times 10^4 \text{ cm}^{-3}$) sphere 77 400 AU in diameter comprised of 3.6×10^6 particles, with a uniform gas particle mass of $1.4 \times 10^{-5} M_{\odot}$. The

¹<http://www-hpcc.astro.washington.edu>

particles are initially placed on a uniform spatial grid, but are perturbed by interpolating over a turbulent velocity grid. This initial turbulent field is randomly generated and thus cannot be identical to BBB3, but it shares the same statistical properties. Therefore the result should be similar, but not identical. We give more discussion about this in section 2.5.

2.2.2 Turbulent Velocity Field

Our turbulence generator code is based on the code David Tilley used for his Master's thesis (Tilley (2001)), which was based on Hugh Couchman's *cosmic* code (private communication). We rewrote it in IDL for convenience and adapted it to our specific needs. It is presented in Appendix A.

The program sets the power spectrum of the velocity field to $P(k) \propto k^{-4}$ in k-space and inverse Fourier transformed the grid to real space.

The wave vectors were normalized such that their amplitude is $A \propto |\vec{r}_k|^{n/2}$, where n is the power spectrum index ($n = -4$) and \vec{r}_k is the 3D wave vector in k-space. A random phase $e^{i\phi_k}$ is applied to ensure the waves are uncorrelated in real space. We apply a randomly oriented unit vector \hat{u}_k to keep the k-space velocity isotropic.

We also want to force our velocity field to be divergence-free. We take the cross product of the wave vector and the vector we just described to get our k-space velocity field. Taking this cross product ensures $\nabla \cdot \vec{v}_k = 0$, but we need to re-normalized the magnitude of the cross product between the wave vector and the unit vector such that

$$\vec{v}_k = \frac{\vec{r}_k \times (|\vec{r}_k|^{n/2} e^{i\phi_k} \hat{u}_k)}{|\vec{r}_k \times \hat{u}_k|} \quad (2.3)$$

where \vec{v}_k is our complex velocity field. Also, to be strictly real, \vec{v}_k has to be Hermitian

$$\vec{v}_k(N - k_x, N - k_y, N - k_z) = \vec{v}_k(k_x, k_y, k_z)^*, \quad (2.4)$$

where N is the number of k modes the velocity field contain in each direction (x, y, z). Finally, \vec{v}_k is inverse Fourier transformed to real space to get our velocity field. We computed the velocity field on a 128^3 grid and interpolated on that grid to get our particle's velocities.

The normalization of the turbulence was set such that the kinetic energy of the cloud equals the magnitude of the potential energy ($K_i = |W_i|$). Thus, the cloud is initially supported by supersonic turbulence and as it decays, the cloud collapses. The normalization of the turbulence we used is a root mean square (RMS) Mach number of 6.4.

2.3 Results and discussion

In this section, we describe the evolution of our model clump. Note that for a better understanding of the dynamics, it is very instructive to look at the movie.² Figure 2.5 shows the density distribution in our simulation at 9 different timesteps. The stars, represented by sink particles in our simulation, are also plotted as white dots. Relatively small scale shocks are created by the initial random velocity field early in the evolution of the clump. Then some larger filamentary structures start forming around $0.53 t_{ff}$ ($t_{ff} = \frac{\pi}{2} \sqrt{\frac{R^3}{2GM}} = 1.97 \times 10^5$ yr). The cloud is losing kinetic energy quickly through these shocks and the cloud starts to collapse under self-gravity, even though initially the cloud has enough kinetic energy to support itself ($\mathcal{M} = 6.4$). Then a central

²Hosted at: <http://www.physics.mcmaster.ca/~petitcn/movie/ClumpMovie2.avi>.

over-density starts forming once the clump begins to collapse under gravity ($t \approx 150 \text{ kyr} = 0.8t_{ff}$). The first star forms after nearly one initial free-fall time, ($t = 1.9 \times 10^5 \text{ yr} = 0.96t_{ff}$), when the kinetic energy of the cloud has significantly decreased ($\mathcal{M} = 3.5$).

Stars begins to form in a relatively small central region of this over-density. See Figure 2.6 for zoomed snapshots of this region ($\sim 20\,000 \text{ AU}$). The number of stars increases quickly, with many stars forming along dense filamentary structures. Many multiple systems are forming during this process, but the high star density in the central region generates many strong gravitational interactions. From these interactions some stars gain high enough velocities to be expelled from the clump and also multiple systems are constantly ripped apart. In the final stages of evolution, leftover gas collapses into the central region where star forming activity is centralized. Most of these evolution features are studied in more detail in this section.

2.3.1 Energy evolution

Figure 2.7 shows the decay of the turbulent kinetic energy of the gas (dashed line, top box) from $t = 0$ to 130 kyr ($0.7t_{ff}$). Kinetic energy is lost in the multiple shocks forming early in the simulation. BBB3 also note rapid initial kinetic energy decay. The rapid decay of turbulent energy allows the global gravitational collapse of the clump which in turn re-injects substantial kinetic energy into the gas.

The first stars (middle box) appear after nearly one initial free-fall time, ($t = 1.9 \times 10^5 \text{ yr} = 0.96t_{ff}$). These stars also subsequently stir the gas, since they have a lot of kinetic energy, but interact only gravitationally with the

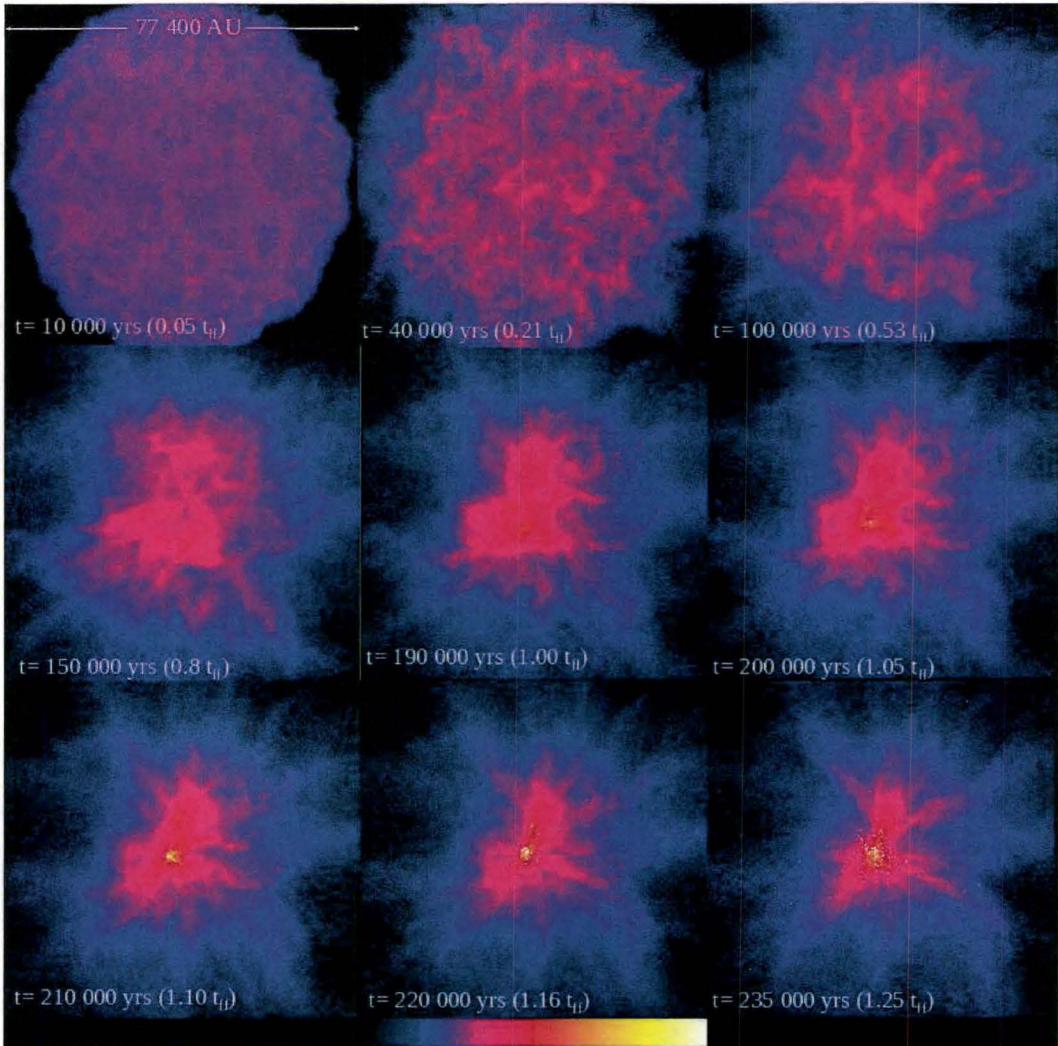


Figure 2.5 Snapshots showing the evolution of the star forming clump. The gas density is plotted on a log scale $-21.2 \leq \log_{10} \rho \leq -11.2$ g/cm³ on the z axis. Each panel is 77 400 AU across and the stars are shown as white dots on the later evolution time steps. The time for each snapshot is indicated in years and in free-fall time (t_{ff}) fraction.

surrounding gas. The gravitational energy is plotted for comparison (solid line).

Figure 2.8 shows the negative kinetic to gravitational energy ratios for the gas (solid line), the stars (dashed line) and for both combined (dot-dashed).

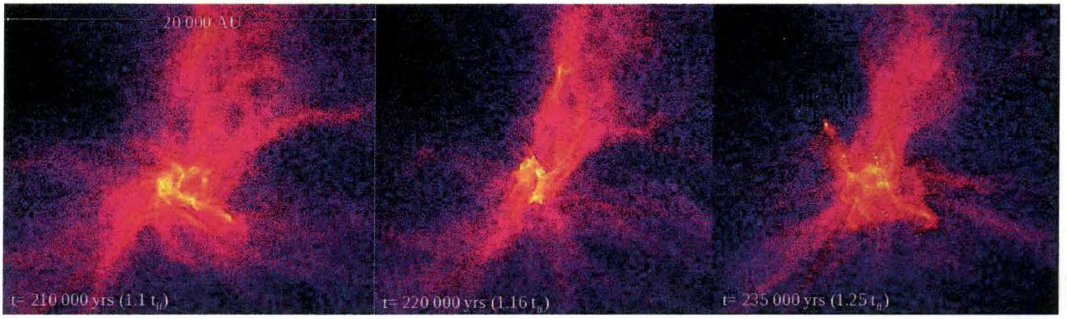


Figure 2.6 Same as Figure 2.5, but for the inner 20000 AU. All the stars form originally near the center, but some are kicked out by strong gravitational interactions.

The initially supersonic gas starts with an excess of kinetic energy compared to virial (dotted straight line). The ratio decreases as the turbulence decays and then goes back up to a significant fraction of the virial ratio ($-E_{Kin}/E_{Grav} = 1/2$), $-E_{Kin}/E_{Grav} \sim 0.4$ for the gas. The stars also become nearly virialized and reach a ratio of ~ 0.3 .

Figure 2.9 shows the evolution of the scalar momentum per mass in units of Mach number ($c_s = 1.84 \times 10^4$ cm/s at 10 K). The gas has an initial turbulent Mach number of 6.4. It decreases down to 3 at $0.6t_{ff}$ and then goes back up even higher (6.5) than its initial value.

When the first star forms, the RMS Mach number has already increased to 3.5 by gravitational collapse itself. Afterwards, the stars formed with high velocities or those gaining momentum through close gravitational interactions increase the overall gas kinetic energy. It is uncertain at this point whether stirring stars or gravitational collapse re-inject more kinetic energy into the gas for the later stages. However, this momentum re-injection exceeds recent results with explicit feedback (outflow) by Nakamura & Li (2007) suggesting that extra energy sources, like stellar feedback, might be unnecessary to explain

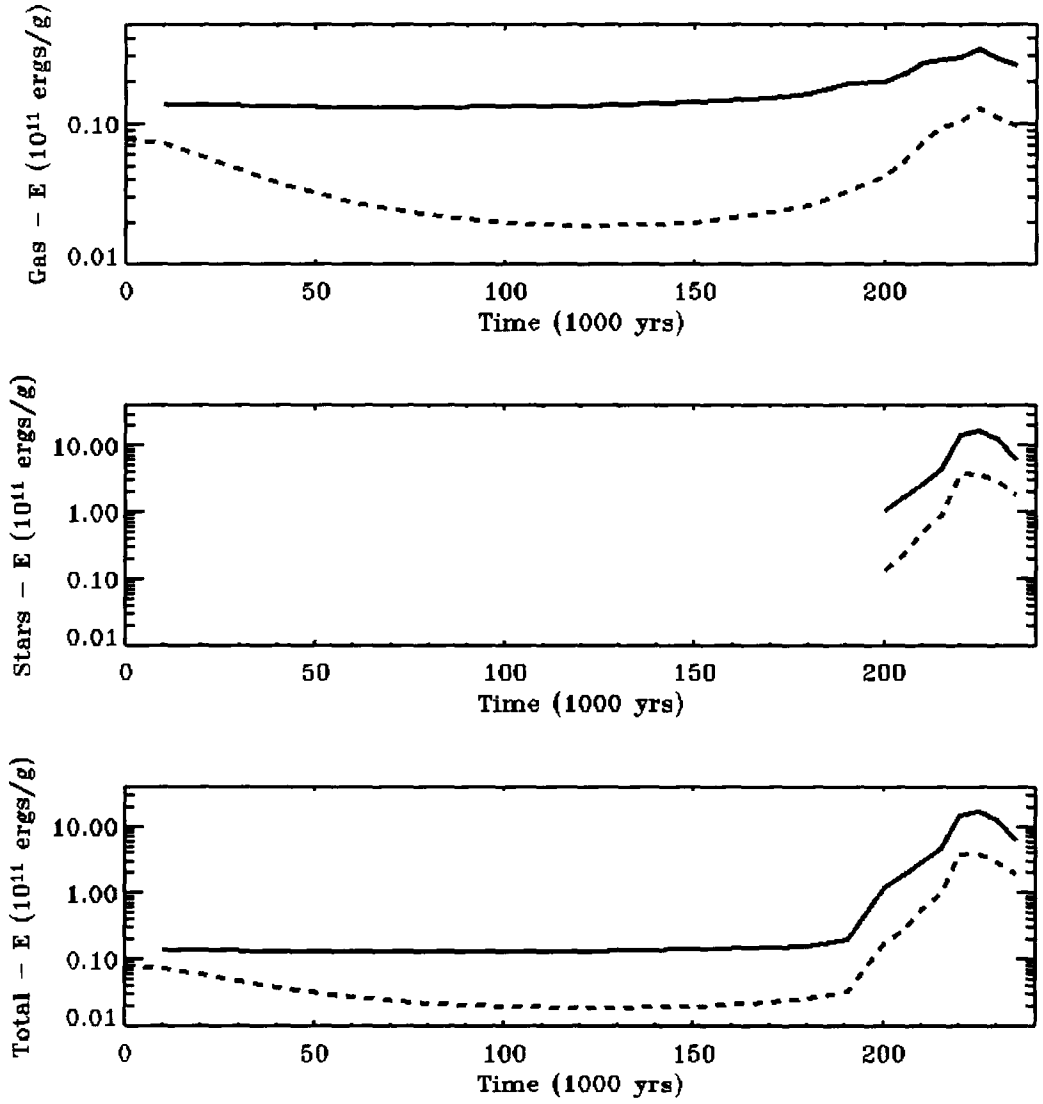


Figure 2.7 Evolution of the kinetic (dashed line) and gravitational (full line; the negative value is shown to compare to the kinetic) energy per mass for the gas (top panel), the stars (middle panel) and both combined (bottom panel). We can see the decay of the initial turbulence and the later re-injection of kinetic energy by the global collapse and the stirring effect of the star particles.

how star forming regions maintain their turbulence. This idea is investigated further in Chapter 3, using a simulation of an entire molecular cloud.

Figure 2.10 shows the evolution of the total velocity dispersion for

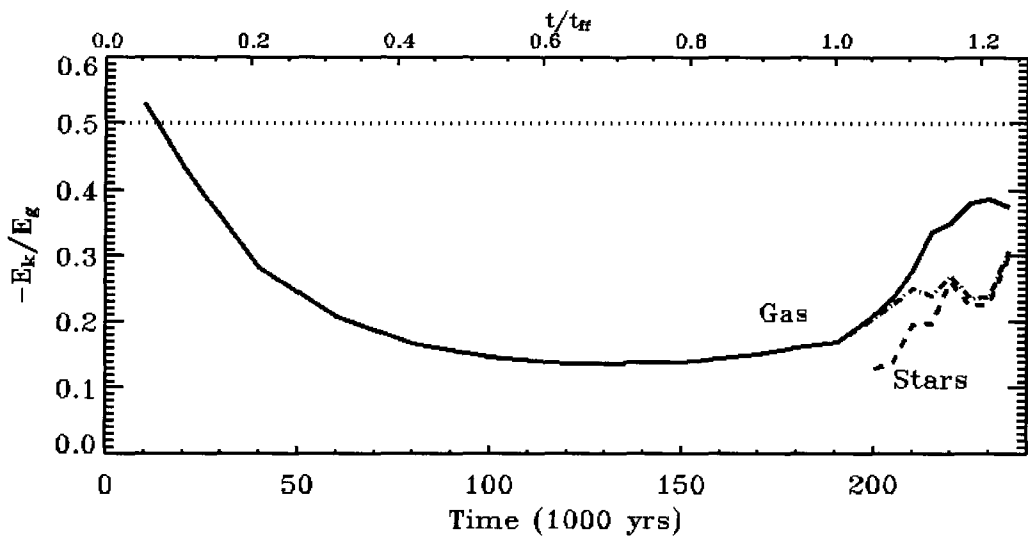


Figure 2.8 Plot of the negative of the energy ratios (kinetic over gravitational) for the gas (full line), the stars (dashed) and for both combined (dot-dashed). The virial ratio is marked by the dotted line.

the gas and stars along with their 1D individual orthogonal vector directions (\hat{x} , \hat{y} , \hat{z}). The stars start with a velocity dispersion similar to the gas, but gain up to a factor 10, some starting at ~ 0.4 km/s and reaching 4 km/s. This steep increase is probably due to strong dynamical interactions. In contrast, BBB3 found a final 3D velocity dispersion of 2.1 km/s and 1.2 km/s in 1D, whereas our final value in 3D is 3.7 km/s and ranges between 2.8 – 3.4 km/s in 1D. This discrepancy is discussed further in section 2.5. Each result compares well to observation: 1D values of ≤ 2.3 km/s have been found for Taurus-Auriga and the Orion Trapezium clusters (Frink et al. (1997); Tian et al. (1996)). For Chamaeleon I, a higher value has been measured ≤ 3.6 km/s (Joergens & Guenther (2001)).

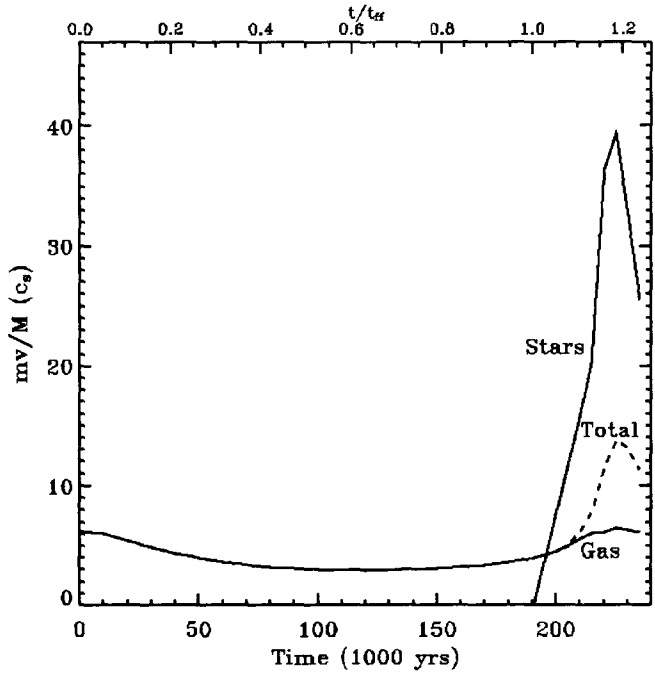


Figure 2.9 Evolution of specific scalar momentum in units of Mach number ($c_s = 1.84 \times 10^4$ cm/s). The full line near the bottom is for the gas, the full line to the right is for stars only and the dashed line is for the combination of both.

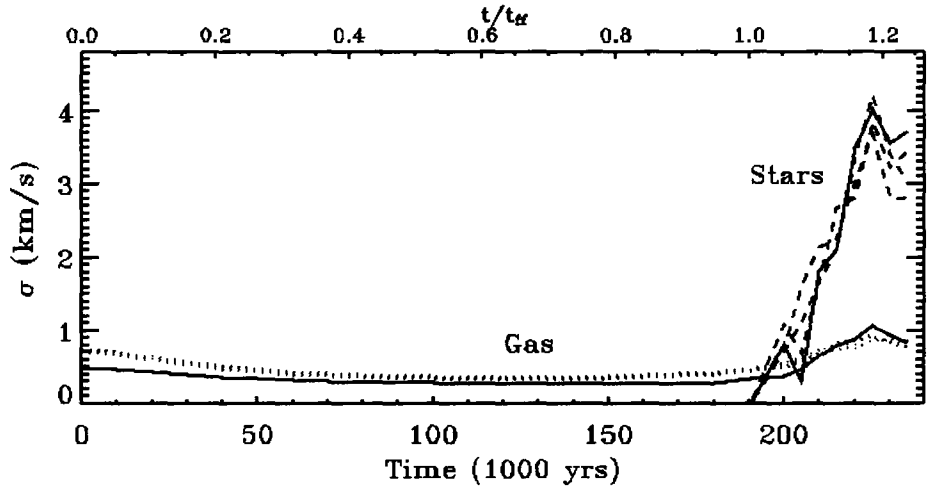


Figure 2.10 Velocity dispersion for the gas and stars (full lines) and $\hat{x}, \hat{y}, \hat{z}$ components (dotted or dashed lines).

2.3.2 Star formation

BBB3 found a total of 50 objects after $1.4t_{ff}$, 23 stars and 27 brown dwarfs. Brown dwarfs are defined here, following BBB3, as objects with $0.08 M_{\odot} \geq M \geq 50M_{gas} = 7 \times 10^{-4} M_{\odot}$, where M_{gas} is the mass of a gas particle and 50 particles are required to form a sink particle. We found 144 objects forming after $1.25t_{ff}$, 30 stars and 114 brown dwarfs. We found 79 objects by $1.16t_{ff}$, 25 stars (similar to BBB3) and 54 brown dwarfs (about twice BBB3).

BBB3 found a low overall star formation efficiency $\approx 12\%$ at $1.4t_{ff}$. After $1.25t_{ff}$, we found an overall formation efficiency of 26.8%, where stars contribute 22.4% and brown dwarfs 4.4%. At the time $1.16t_{ff}$, we found a total formation efficiency of 17.2%, a star formation efficiency of 13.7% and a brown dwarf formation efficiency of 3.5%. This indicates that most of the formation efficiency gained in the later stages of the simulation is via accretion onto stellar mass objects and that the bulk of the stellar fragmentation process is already over around $1.16t_{ff}$. The observed overall star formation efficiency in ρ Ophiuchus is 20-30% (Wilking & Lada, 1983), nearly what we find in our simulation.

The different star formation efficiency between BBB3 and our simulation could be explained by a different rate of dynamical evolution. Since star formation continues until the end of our simulation, the efficiency will depend on the time we decide to stop. Our star formation efficiency at $1.16t_{ff}$ is close to BBB3. Our simulation seems to evolve faster dynamically due to the different random initial turbulence field.

Figure 2.11 and 2.12 show that the high mass end of our stellar mass distribution compares well with the Salpeter (1955) or Kroupa (2001) IMF.

However, our simulation forms an excess of brown dwarfs. This result is consistent with what was found by BBB3, but it is more pronounced in our simulation. The limit between stars and brown dwarfs is shown (dotted line) on both figures. The cumulative IMF shown in Figure 2.12 is a way to display the mass distribution that is less intuitive, but it is much less influenced by low number statistics. We see on this figure that the trend at the high mass end is less affected by low number statistics and is in reasonable agreement with Salpeter or Kroupa. At the low mass end however, we see a clear divergence between our data and a Kroupa distribution.

2.3.3 Multiplicity

Tables 2.1 and 2.2 show how many stars have bound companions. We selected bound objects by measuring the kinetic energy of the system, subtracting the kinetic energy of the center of mass and comparing to their mutual gravitational energy. We found all the systems with semi-major axis ($a \leq 1000$ AU) following BBB3 to compare our results. The multiplicity fraction (f_{multi}) and the companion frequency (f_{comp}) are defined as

$$f_{multi} = (B + T + Q)/(S + B + T + Q) \quad (2.5)$$

$$f_{comp} = (B + 2T + 3Q)/(S + B + T + Q) \quad (2.6)$$

where S, B, T and Q are the number of single, binary, triple and quadruple systems respectively.

For the 144 objects after 135000 yr of evolution, we found S=124, B=8, T=0, Q=1 so $f_{multi} = 6.77\%$ and $f_{comp} = 8.27\%$. After only 120000 yr of

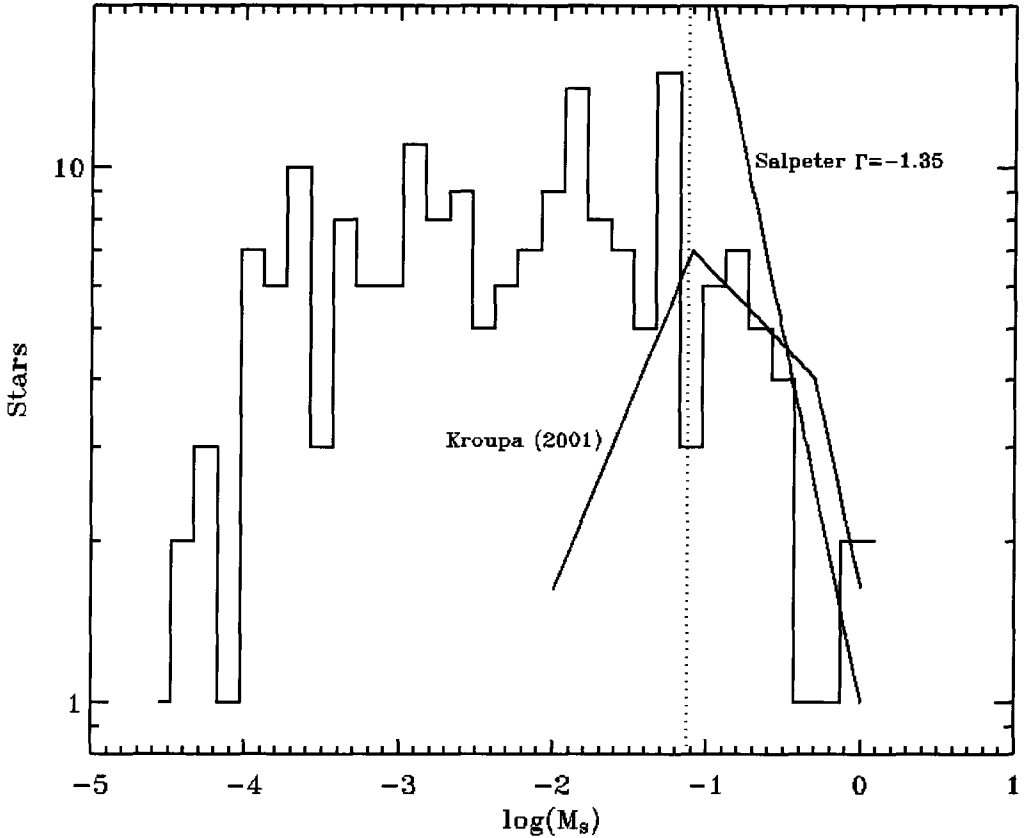


Figure 2.11 The initial mass function of all the sink particles formed. The Salpeter and Kroupa mass distributions are plotted for reference and normalized to fit the high mass end of our distribution.

evolution 79 objects had formed with $S=59$, $B=5$, $T=2$, $Q=1$ so $f_{multi} = 11.94\%$ and $f_{comp} = 17.91\%$. BBB3 found for 50 objects that $S=26$, $B=1$, $T=1$. They also found a system of 7 objects and another with 11 objects giving $f_{multi} = 13.33\%$ and $f_{comp} = 63.33\%$. Even though they found fewer binary systems, they still find a high companion frequency because 2 systems have so many objects. These systems are likely unstable.

Table 2.3 shows that fewer multiple systems remained (3) than got disrupted (5) or formed (5) between 220 kyr and 235 kyr. All of our triple

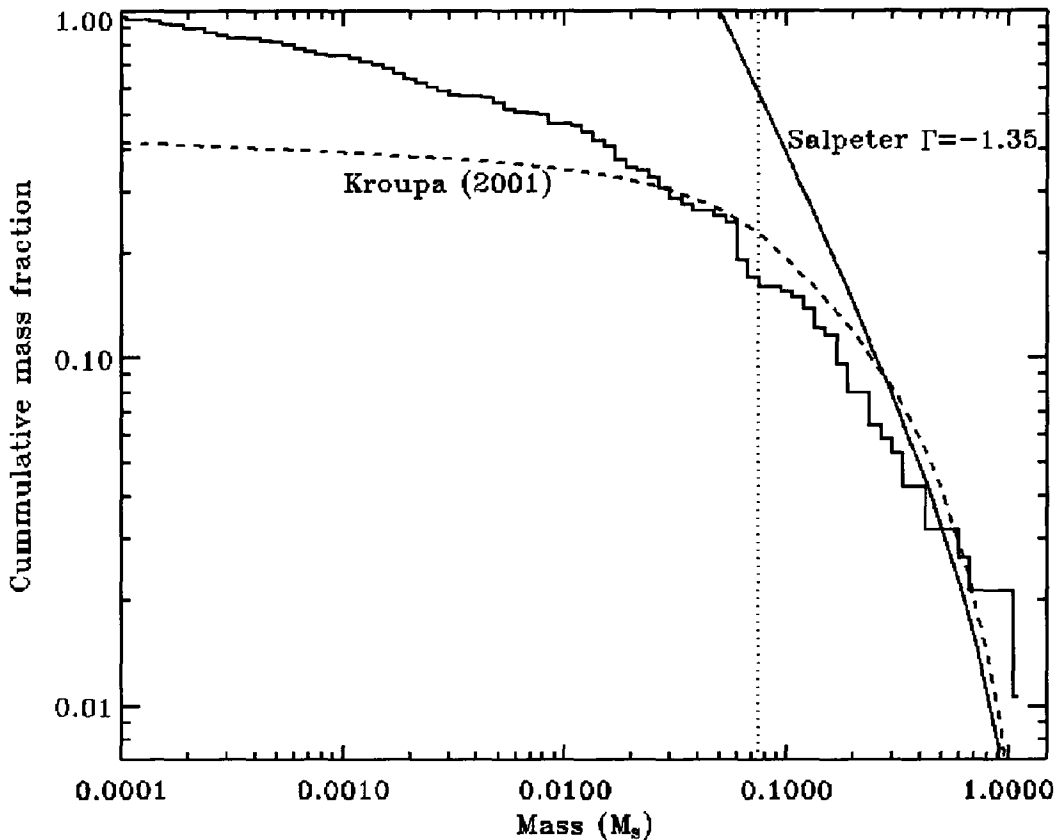


Figure 2.12 The cumulative initial mass function of all the sink particles formed, representing the fraction of stars in the clump with a mass equal or larger to the binned value. The Salpeter and Kroupa mass distributions are plotted for reference and normalized to fit the high mass end of our distribution.

and quadruple systems were destroyed. This represents the large amount of interaction between the systems. 2 stars (39 and 65, in bold on table 2.3) left their respective companion, but then found a new one. The stars numbered 0-98 were created before 220 kyr, and they include 3 new binary systems, including 2 (39 and 65) that exchanged companions. After 220 kyr, only two new binary systems formed from the 65 new stars and 63 of these new stars were brown dwarfs. Considering the low statistics on these multiple systems,

Table 2.1. List of the multiple systems found after 220 000 yr ($1.16t_{ff}$) and their statistics. The masses are in solar masses, Q is the mass ratio ($Q = M_{primary}/M_{secondary}$) and a is the semi-major axis in AU. The binary systems marked with a * are part of a larger system.

Star 1	Star 2	Mass 1 (M_{\odot})	Mass 2 (M_{\odot})	Q	a (AU)
*0	1	0.90	0.69	0.77	4
5	37	0.15	0.07	0.43	123
*6	12	0.74	0.29	0.39	25
*7	28	0.30	0.35	0.86	4
13	22	0.18	0.16	0.89	14
19	39	0.25	0.13	0.54	179
21	27	0.06	0.07	0.90	339
65	67	0.12	0.01	0.11	223
(0,1)	66	1.59	0.11	0.07	80
(6,12)	2	1.02	0.68	0.66	450
(6,12)	17	1.02	0.25	0.24	718
(7,28)	18	0.65	0.21	0.31	529

especially the higher order ones, and their very dynamical aspect (i.e. how different the results are from 120 to 135k yr), this apparent discrepancy with BBB3 in the multiple or companion frequency is not significant.

Observations of young star forming regions generally find a high companion frequency. In their review of all known nearby associations, Zuckerman & Song (2004) found a companion frequency of 20 to 60%. However, these observations suffers from low number statistics; see Duchêne et al. (2007) for a recent review. Our measured multiplicity is therefore lower than expected. However, from watching the movie of the simulation, we can see that many stars are forming in multiple systems, but eventually get disrupted via gravitational interactions with surrounding stars. It is therefore not too surprising

Table 2.2. List of the multiple systems found same as table 2.1, but after 235 000 yr ($1.25t_{ff}$).

Star 1	Star 2	Mass 1 (M_{\odot})	Mass 2 (M_{\odot})	Q	a (AU)
5	37	0.16	0.07	0.43	77
7	28	0.57	0.67	0.85	2
13	22	0.18	0.16	0.90	18
21	27	0.059	0.07	0.90	337
36	65	0.18	0.27	0.66	18
39	102	0.35	0.01	0.01	182
57	80	0.24	0.19	0.79	56
114	118	0.06	0.01	0.02	609
*140	150	0.09	0.01	0.06	307
*145	151	0.02	0.01	0.05	390
(145,151)	(140,150)	0.02	0.10	0.24	856

Table 2.3. List of the changes in the systems, between 220 kyr and 235 kyr. The bold stars moved from one binary system to a different one.

Remaining	Disrupted	New
(5,37)	(0,1)	(36, 65)
(7,28),(18-disrupted)	(6,12),(2),(17)	(39 ,102)
(13,22)	(19, 39)	(57,80)
	(21,27)	(114,118)
	(65 ,67)	(140,150),(145,151)

to find a lower multiplicity in a dense star cluster, like the one we simulated. This suggests that multiplicity in our simulation is highly time dependent and also strongly influenced by the number of stars present within the star cluster.

Figure 2.13 shows the binary fraction as a function of mass at the end of our simulation (135 kyr) and that massive stars are most likely to form in a binary system. The binary fraction increases from $\sim 10\%$ for brown dwarfs to $\sim 50\%$ for solar mass primary objects. Earlier in the simulation (120 000 yr), the binary fraction of solar mass objects is even bigger $\sim 75\%$. Figure 2.14 shows that these results compare well with the observed mass distribution for multiplicity. BBB3 also found a very low binary fraction for brown dwarf systems ($\sim 5\%$), so our simulations agree in this general trend. The observed multiplicity for brown dwarfs is also very low.

2.3.4 Mass Accretion History

Figure 2.15 shows the mass accretion history of each sink particle. We identify three distinct trends in these evolution tracks. The most massive stars, above 1 solar mass (red), formed early in the mass range between 0.02-0.2 solar mass and then accrete most of their mass throughout the entire simulation.

The mid-range final mass stars (black), 0.01-0.5 solar mass, formed with similar masses to the massive stars. However, they form later in the simulation and they accrete less mass. Accretion ceases before the end of the simulation for these stars as they seem to run out of gas and may have been ejected from the central part of the cluster.

The low final mass stars (green) formed late and show little mass accretion at any point of their evolution. This could explain the reduction in the

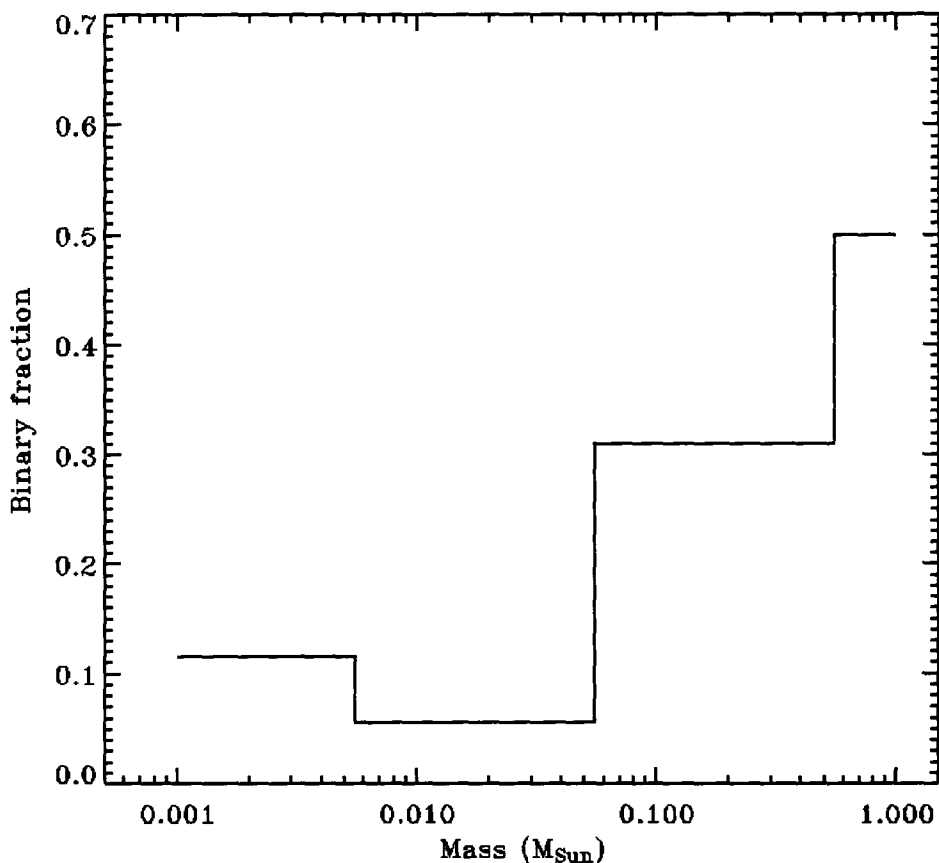


Figure 2.13 Histogram of the binary fraction in function of mass at the final stage (135 000 yr).

multiplicity fraction between 220 kyr and 235 kyr, since low mass objects are rarely found in multiple systems.

Figure 2.15 suggests that if we let the simulation evolve much longer, a gap might form between the massive stars and the others since massive stars keep accreting, albeit at a lower rate, and low mass accretion stops. The gap in the IMF would be around $1 M_{\odot}$. The observed IMF does not show such a gap. We ascribe the discrepancy to the lack of stellar feedback in our simulation that would affect the fragmentation and accretion processes at the late stages.

The evolution tracks of the black and green mass ranges could perhaps

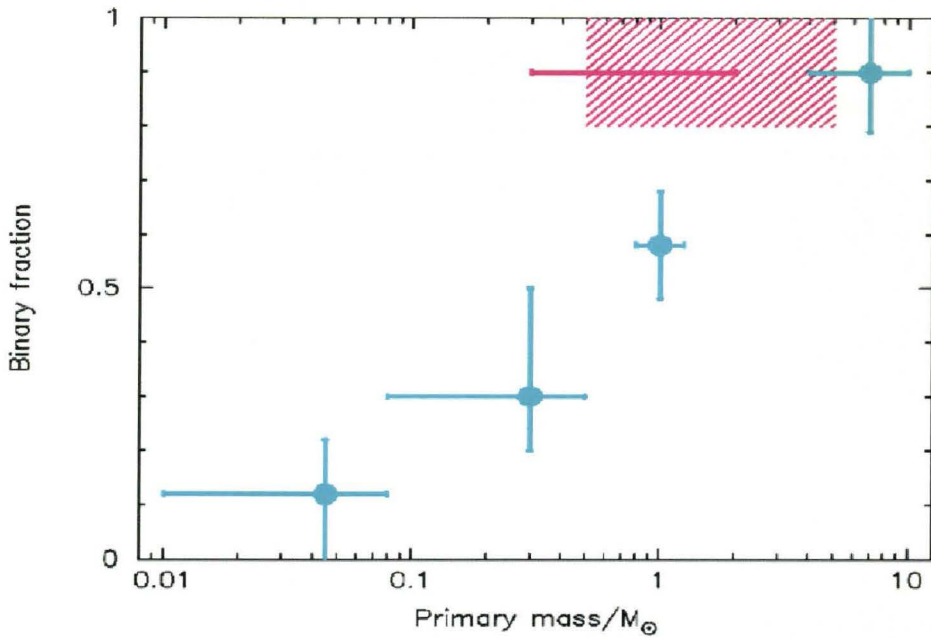


Figure 2.14 Observed mass distribution of the binary fraction, from Goodwin’s talk at the Multiplicity in star formation workshop in Toronto (<http://www.astro.utoronto.ca/msf/talks/Day1/MSF2007-1A1-Goodwin.pdf>).

be explained by the lack of accretable gas available for these stars after ~ 220 kyr. However, the average gas density at the center of mass of the simulation is actually increasing by over an order of magnitude between 200 kyr ($1.3 \times 10^6 \text{ cm}^{-3}$) and 230 kyr ($3.05 \times 10^7 \text{ cm}^{-3}$), as the gas collapses towards the center of mass. This explains why the massive stars (red) can still find a fair amount of gas to accrete. The accretion history shown on Figure 2.15 therefore suggests some form of competitive accretion. While all the stars are formed initially at a similar low mass, some accrete more than others.

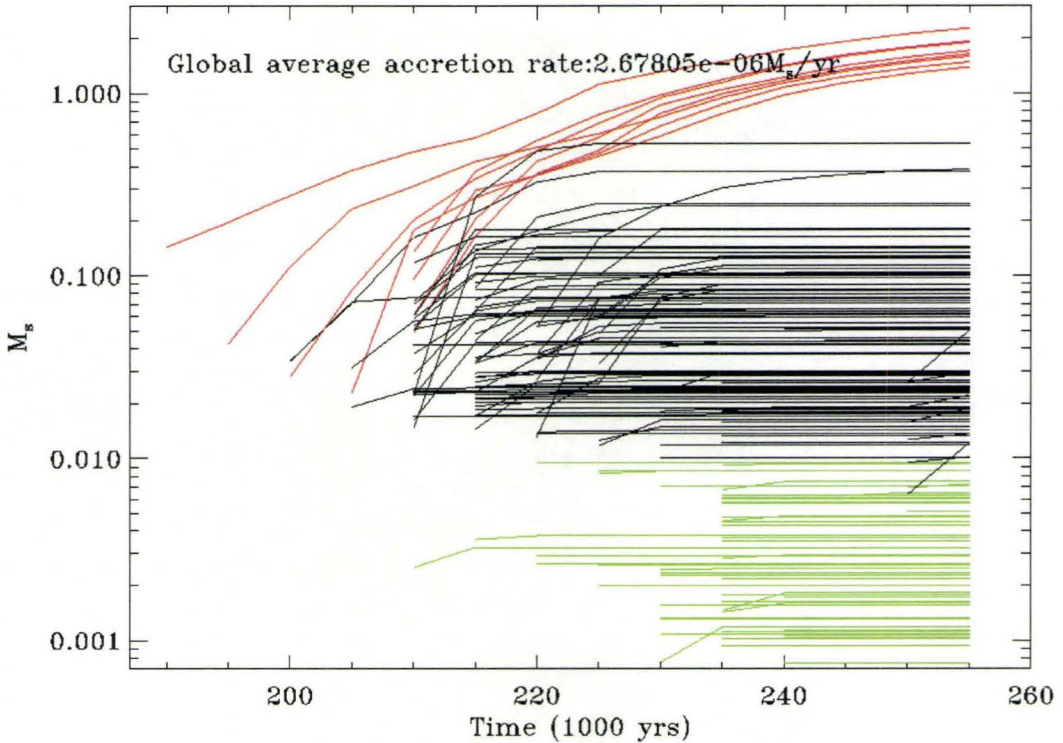


Figure 2.15 Evolution tracks of the sink particles. The stars with final masses below 0.01 solar mass are shown in green, above 0.631 solar mass in red and in between these masses in black.

2.4 Testing sinks

Given the discrepancy between our results and BBB3, we investigated the fundamental differences between our SPH solvers. Notably, each solver defines the number of neighbours for the SPH particles differently. GASOLINE always uses the same number of neighbours whereas BBB3 use an approximate number of neighbours that varies, but is generally higher (50) than the 32 particles used in GASOLINE and has shown good results in the past that way (Wadsley & Bond, 1997). We tested the impact of the difference in number of neighbours on the accretion rate and physical properties at the sink boundary. We evolved

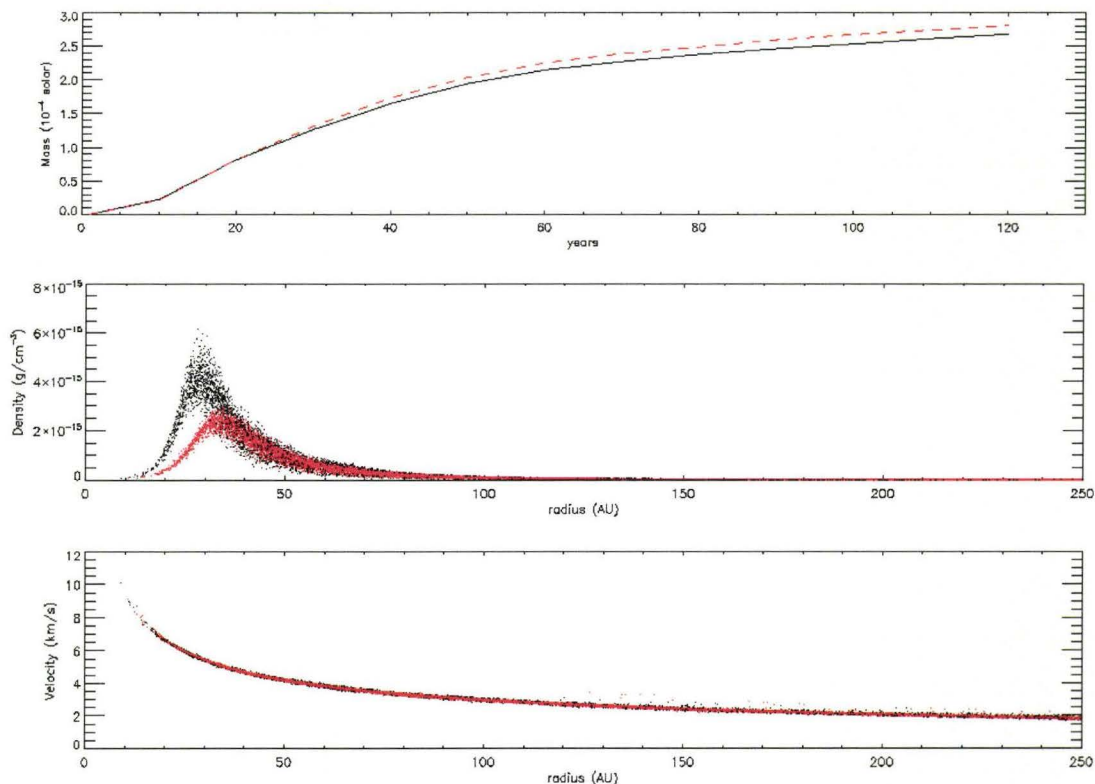


Figure 2.16 Test for the number of neighbours effects. The black line/dots are the results using 32 neighbours and in red the results using 50 neighbours. The first plot is showing the mass accreted over time. The middle is showing the density for each gas particles as a function of its distance from the sink after 120 years. And in the bottom plot we see the velocity magnitude as a function of the distance.

a simple $0.001 M_{\odot}$ sphere of 17 000 gas particles with uniform density and a $1 M_{\odot}$ sink particle in the middle. We let it evolve for 120 yr.

Using different number of neighbours, Figure 2.16 shows a significant difference in the accretion rate (top panel) and in the density around the sink (middle panel), but no difference in the particle velocities even very close to the sink (bottom panel).

For the gas particles near the sink radius, the smoothing length is larger

than it should be because of the lack of gas particles near the sink, and the requirement of the 32 or 50 neighbours. The density calculation is weighted by the smoothing length ($\rho \sim h^{-3}$) (Wadsley et al., 2004)

$$\rho_i = \sum_j m_j W_{ij}(r_{ij}, h_{ij}) \quad (2.7)$$

$$W(r_{ij}, h_{ij}) = \frac{1}{\pi h_{ij}^3} \begin{cases} 1 - \frac{3q^2}{2} + \frac{3q^3}{4} & : 0 \leq q < 1 \\ \frac{(2-q)^3}{4} & : 1 \leq q < 2 \\ 0 & : q \geq 2 \end{cases} \quad (2.8)$$

where $q = r_{ij}/h_{ij}$ and equation 2.8 is a kernel based on spline functions (Monaghan (1992)). Consequently, the density profile is worst near the sink using more neighbours. The sink radius was 5 AU in both cases, but the radius at which the density starts to drop and be unphysical is ~ 30 AU for $N_{neighbour} = 32$ and is larger by ~ 5 AU using $N_{neighbour} = 50$. The reduction in maximum density reached near the sink particle reduces the pressure support, which may explain the difference in the total mass that is accreted.

We observed no difference in particle velocities near the sink. Therefore, the angular momentum transfer via shear viscosity, present in the simulation due to interaction of the particles, does not seem to be affected by the change in the number of neighbours. Note that Bate (private communication) argues that the pressure issue is not critical and that the most important quantity at the boundary is the angular momentum. Therefore we expect the number of neighbours difference to have small impact overall.

2.5 Conclusion

Overall our simulation compares well with BBB3. We observe competitive accretion, as they do, but there are some differences. In both cases the first stars start forming after approximately one free fall time, $0.96t_{ff}$ for us and $1.037t_{ff}$ for BBB3. Our final object's 3D velocity dispersion is slightly larger, 3.7 km/s compared to ~ 2.1 km/s. We both found an excess of low mass objects. We formed many more objects (144 compared to 50), but the main difference is in our number of brown dwarfs. The bulk of our brown dwarfs form late in the simulation, when the effects of stellar feedback might be significant. So, at this late stage, the fragmentation process is probably already unphysical. The discrepancy with BBB3 thus is not problematic; it just highlights the fact that our simulation evolved faster. Consequently, our star forming efficiency is higher (27% after $1.25t_{ff}$ compared to 12% after $1.4t_{ff}$). A straight-forward explanation for the larger velocity dispersion is in the larger number of stars we formed. Since most stars form in the dense central region, the star density locally increased. The stars therefore have a larger chance to undergo strong gravitational interactions which increases their velocity dispersion.

Clearly, some discrepancies should be expected based on our use of slightly different initial conditions. Our initial velocity field had the same power spectrum, though each individual mode was generated randomly. Considering that the fragmentation process is generally considered to be dominated by turbulent fragmentation instead of pure gravitational fragmentation, small differences in the initial conditions velocity field could potentially lead to major discrepancies. For a more direct code comparison, we should use the exact same initial conditions. We didn't ask BB03 for their initial conditions, we

preferred to produce our own, so we could modify them and make them more realistic (see section 3.3.1).

Some variations also arise from the differences in the SPH solvers. The main difference we identified that could have a serious impact on the final result was the difference in how the codes determine the number of neighbours. Since the number of neighbours is a key element in the sink particle's boundary issues, this could affect the accretion rate and therefore the final mass of stars. It could also affect the star formation process by changing the amount of "free" gas available to form new stars. However, the change was small.

The sink particle is clearly an attractive idea, since it allows us to get rid of all the high density gas particles that slow down the simulation, and at the same time simplifies the complex physical processes happening at small scales. They enable us to follow the fragmentation process much further; however, further in-depth investigation of the numerical side effects is required before such results can be fully trusted. Without boundary conditions, the accretion rate is artificially high, unless all accretion is supersonic, which is unlikely. However, the boundary condition issues are very hard to fix. Therefore sinks are difficult to control and could have negative impacts on the resulting IMF, multiplicity, scattering, etc...

The time evolution of the temperature-density relation (Figure 2.4) shows that the barotropic equation of state cannot be fully trusted for the regions surrounding the protostar center. At densities as low as $2.5 \times 10^{5-6} \text{ cm}^{-3}$ ($10^{-17} - 10^{-18} \text{ g cm}^{-3}$), compressional heating becomes significant (Masunaga & Inutsuka (2000); Stamatellos et al. (2007)), and the temperature in the central region begins to increase. At the critical density ($2.5 \times 10^{10} \text{ cm}^{-3}$, $10^{-13} \text{ g cm}^{-3}$) where the barotropic equation of state is no longer isothermal, the sur-

rounding gas can already be heated by an order of magnitude (see Figure 2.4). Increased thermal support would slow down the accretion rate. Therefore, we consider the isothermal approximation accurate only until $n \approx 2.5 \times 10^8 \text{ cm}^{-3}$ ($10^{-15} \text{ g cm}^{-3}$), where the temperature-density curves start to diverge dramatically at different times. Following the fragmentation further would probably require radiative transfer to be reliable.

This could be the key missing physics to find out which fragmentation model is right. The extra heating predicted by the 1D radiative transfer calculations (Stamatellos et al., 2007) could prevent the fragmentation of the large cores to multiple low mass stars. This would solve the overabundance of brown dwarfs problem found by BBB03 and our simulations. Recently Bate (2008) indeed showed that including radiative transfer can have dramatic effects on the fragmentation process.

SPH simulations of gas clumps provide useful information about clustered star formation. However, we found two key points of concern about its accuracy that should be addressed: the sink particle's boundary conditions effect on their surrounding gas, and the over-simplification of the equation of state. This guided our new approach in succeeding chapters, where we choose to avoid both sinks and barotropic assumptions; allowing us to concentrate on the role of turbulence in forming prestellar cores.

Bibliography

Alves, J., Lombardi, M., & Lada, C. J. 2007, *A&A*, 462, L17

P. Andre, S. Basu and S. i. Inutsuka, The Formation and Evolution of Prestellar Cores, arXiv:0801.4210 [astro-ph].

Bate, M. R., Bonnell, I. A., & Price, N. M. 1995, *MNRAS*, 277, 362

Bate, M. R. 1998, *ApJ*, 508, L95

Bate, M. R., Bonnell, I. A., & Bromm, V. 2003, *MNRAS*, 339, 577

Bate, M. R. 2008, arXiv:0811.1035

Benz, W. 1990, Numerical Modelling of Nonlinear Stellar Pulsations Problems and Prospects, 269

Benz, W., Cameron, A. G. W., Press, W. H., & Bowers, R. L. 1990, *ApJ*, 348, 647

Bergin, E. A., & Tafalla, M. 2007, *ARA&A*, 45, 339

Bodenheimer, P., Burkert, A., Klein, R. I., & Boss, A. P. 2000, Protostars and Planets IV, 675

- Bonnell, I. A. 1994, MNRAS, 269, 837
- Bonnell, I. A., & Bate, M. R. 2006, MNRAS, 370, 488
- Bonnell, I. A. 2008, Pathways Through an Eclectic Universe, 390, 26
- Commerçon, B., Hennebelle, P., Audit, E., Chabrier, G., & Teyssier, R. 2008, A&A, 482, 371
- R. Courant, K. O. Friedrichs & H. Lewy 1928, Math. Ann., 100, 32
- Dobbs, C. L., Bonnell, I. A., & Clark, P. C. 2005, MNRAS, 360, 2
- Duchêne, G., Delgado-Donate, E., Haisch, K. E., Jr., Loinard, L., & Rodríguez, L. F. 2007, Protostars and Planets V, 379
- Frink, S., Röser, S., Neuhäuser, R., & Sterzik, M. F. 1997, A&A, 325, 613
- Joergens, V., & Guenther, E. 2001, A&A, 379, L9
- Kroupa, P. 2001, MNRAS, 322, 231
- Krumholz, M. R., McKee, C. F., & Klein, R. I. 2005, Nature, 438, 332
- Larson, R. B. 2005, MNRAS, 359, 211
- Mac Low, M.-M., & Klessen, R. S. 2004, Reviews of Modern Physics, 76, 125
- Masunaga, H., Miyama, S. M., & Inutsuka, S.-I. 1998, ApJ, 495, 346
- Masunaga, H., & Inutsuka, S.-i. 2000, ApJ, 531, 350
- Monaghan, J. J. 1992, ARA&A, 30, 543
- Motte, F., Andre, P., & Neri, R. 1998, A&A, 336, 150

Nakamura, F., & Li, Z.-Y. 2007, ApJ, 662, 395

Salpeter, E. E. 1955, ApJ, 121, 161

Stamatellos, D., Whitworth, A. P., Bisbas, T., & Goodwin, S. 2007, A&A, 475, 37

Tian, K. P., van Leeuwen, F., Zhao, J. L., & Su, C. G. 1996, A&AS, 118, 503

Tilley, D. A. 2001, *3-D simulations of structure formation in turbulent molecular clouds*, M.Sc. Thesis, McMaster University

Quinn, T., Katz, N., Stadel, J., & Lake, G. 1997, ArXiv Astrophysics e-prints, arXiv:astro-ph/9710043

Wadsley, J. W., & Bond, J. R. 1997, Computational Astrophysics; 12th Kingston Meeting on Theoretical Astrophysics, 123, 332

Wadsley, J. W., Stadel, J., & Quinn, T. 2004, New Astronomy, 9, 137

Whitehouse, S. C., & Bate, M. R. 2006, MNRAS, 367, 32

Wilking, B. A., & Lada, C. J. 1983, ApJ, 274, 698

Zuckerman, B., & Song, I. 2004, ARA&A, 42, 685

Chapter 3

Molecular Cloud Turbulence

3.1 Introduction

Molecular clouds have been known to be turbulent since the first observations of their CO linewidths, which were far too broad to be explained by thermal broadening. These were interpreted as a signature of large scale motion at first (rotation, collapse or expansion) (Goldreich & Kwan, 1974). But from the lack of evidence of systematic patterns induced in the lines by these motions (Heiles & Katz, 1976), they were later generally interpreted as the presence of supersonic turbulence (local motion) (Zuckerman & Evans, 1974). It was then considered as a mechanism of support against gravity. Now it is even considered as one of the key ingredients for the process of star formation, via turbulent fragmentation. Some numerical simulations have even shown that a reasonable IMF can be built from it (Padoan & Nordlund, 2002; Padoan et al., 2007), without even including self-gravity!

The physical origin of supersonic turbulence, however, remains unclear. Even more so, since numerical simulations of supersonic turbulence have shown how quickly such turbulence decays, in approximately a dynamical time ($t_{dyn} = L/\sigma_v$, where L is the simulation size and σ_v is the velocity dispersion), even in the presence of a magnetic field (Gammie & Ostriker, 1996; Mac Low et al., 1998; Stone et al., 1998; Padoan & Nordlund, 1999; Mac Low, 1999; Mac Low & Klessen, 2004; Elmegreen & Scalo, 2004). This implies that turbulence must be constantly driven somehow, if the lifetime of the molecular clouds is considered longer than a dynamical time (see section 3.1.3 for more details on this topic).

These issues leads to two different views of the molecular clouds evolution, leading to two different simulation methods. In the first one, the turbulence is set initially and is allowed to decay freely (Klessen et al., 1998; Bonnell et al., 2003; Bate et al., 2002; Tilley & Pudritz, 2004; Vázquez-Semadeni et al., 2007). However no significant decay in the molecular clouds turbulence is seen observationally. Therefore, the alternative view is to artificially drive the turbulence (Padoan & Nordlund, 1999; Gammie et al., 2003; Li et al., 2004; Jappsen et al., 2005) such that it is maintained at a constant level throughout the evolution of the molecular cloud. Both methods obtained reasonable success at reproducing observations, e.g. the IMF. However, the driving mechanism remains forced and thus unphysical.

Therefore, we try to address here two outstanding question about star formation in turbulent molecular clouds: Is turbulence driven or decaying? If it is driven, what is the driver? To do so we will first review the observable properties of turbulence (power spectrum, structure function and density probability density function (PDF)) in section 3.2. Then we will describe the

SPH simulations we ran and the anisotropic turbulent velocity field we used in section 3.3. We discuss our results (turbulence magnitude evolution, energy distribution, density PDF and the velocity structure function) in section 3.4 and in section 3.5 we present our conclusions.

Significant work has been done to find out whether turbulence is driven or decaying. Klessen (2001) numerically studied the effects of different types of turbulence on the IMF. They conclude that both decaying and large scale driven turbulence lead to fragmentation in reasonable agreement with observations. MHD turbulent simulations results, analysed by Basu & Murali (2001), also indicate that a large scale driving source could explain observations. More recently, Offner et al. (2008,b) did Adaptive Mesh Refinement (AMR) hydrodynamic self-gravitating simulations of prestellar and protostellar (using sinks) core formation. They compared a simulation where the turbulence was constantly driven to one where the initial turbulence could decay. They also compared them to observations, to find which matched the observations better. They found that the driven simulation agreed better with cores in Perseus, but the decaying simulation matched better to the cores observed in ρ Ophiuchus. Overall they were unable to determine which one was more similar to observations.

There are many possible sources of energy to drive turbulence. They can be separated in two different types: the external turbulence sources from the interstellar medium (ISM): shear from galactic rotation (Fleck, 1981; Sellwood & Balbus, 1999), spiral arm stirring (Bonnell et al., 2006; Kim et al., 2006) or internal sources from stellar feedback such as outflows and jets (Mac Low & Klessen, 2004; Krumholz et al., 2006; Matzner, 2007; Li & Nakamura, 2006; Nakamura & Li, 2007; Carroll et al., 2008; Banerjee et al., 2007), ioniz-

ing radiation (Bertoldi, 1989; Elmegreen et al., 1995; Kessel-Deynet & Burkert, 2003; Krumholz et al., 2006; Gritschneider et al., 2009), O star and Wolf-Rayet winds (Mac Low & Klessen, 2004) or supernovae (Rosen et al., 1993; Rosen & Bregman, 1995; Norman & Ferrara, 1996; de Avillez, 2000; Wada & Norman, 2001; Kim et al., 2001; de Avillez & Breitschwerdt, 2004a,b; Mac Low et al., 2005). However, which one of these dominates, if any, is unclear at this point.

The possibility of outflows driving turbulence has been the subject of a few recent analytical studies (Krumholz et al., 2006; Matzner, 2007). Also 3D simulations (Li & Nakamura, 2006; Nakamura & Li, 2007) have shown that outflows could provide a significant amount of kinetic energy to the molecular gas. Carroll et al. (2008) also came to similar conclusions, but found a resulting power spectrum of $\beta \sim 3$, which is steeper than expected ($\beta \approx 2$), see section 3.2.5. However, simulations of collimated jets (Banerjee et al., 2007) question the ability of jets to sustain supersonic turbulence in molecular clouds.

3.1.1 Kolmogorov and Burgers turbulence theory

In the warm diffuse ISM, turbulence is observed to be transonic, i.e. to have a root mean square (RMS) velocity ($\sqrt{\langle v^2 \rangle}$) close to the sound speed (c_s) with $c_s \sim \sqrt{\langle v^2 \rangle} \sim 10$ km/s (Heiles & Troland, 2003). In molecular clouds it is supersonic, with $\mathcal{M} \sim 5-20$ (Zuckerman & Evans, 1974), where \mathcal{M} is the Mach number ($\sqrt{\langle v^2 \rangle}/c_s$). Since the velocities are generally larger than the sound speed, $\sqrt{\langle v^2 \rangle} > c_s$, the Kolmogorov theory ($P(k) \propto k^{-5/3}$) for incompressible fluids (Kolmogorov, 1941), can not apply. For compressible gas, some of the energy will be dissipated by shocks. Dense structures also form via shocks. This regime is called Burgers turbulence ($P(k) \propto k^{-2}$) (Burgers, 1974), and

is approximately the type of turbulence expected within molecular clouds.

3.1.2 Inertial range

In a turbulent gas, the kinetic energy is transferred from the large scales, to smaller turbulence scales via nonlinear interactions. The turbulent energy then reaches the dissipative scale and the kinetic energy is transformed into heat. The regime where the turbulence cascades to smaller and smaller scales is called the inertial range. This is the range of scales where the simulations of turbulence can be compared to the above analytical theories (Burgers and Kolmogorov).

3.1.3 Timescale

Turbulence was originally thought of as a mechanism to support the cloud against gravitational collapse. However, its decay rate has been shown to be less than a dynamical time by simulations of supersonic turbulence including magnetic fields to slow down the turbulence decay (Stone et al., 1998; Mac Low, 1999; Padoan & Nordlund, 1999; Basu & Murali, 2001).

Traditionally, the molecular cloud lifetime was thought to be much larger than their freefall times (Blitz & Shu, 1980). This was based on the slow star formation rate observed (Zuckerman & Evans, 1974), by dividing the total mass of an object by its free-fall time, assuming 100% star formation efficiency. This calculation can also be applied to any molecular cloud or clump and the predicted star formation rate found is ~ 100 times larger than the observed values (Krumholz, 2006).

Many recent results however challenge this idea, and suggest that it

could be of the order of or even less than t_{ff} (Hartmann et al., 2001; Hartmann, 2003; Ballesteros-Paredes et al., 1999; Elmegreen, 2007).

To explain some outstanding issues with the stellar population ages, Hartmann et al. (2001) advocated for a short cloud lifetime and rapid star formation. The main problems are that the Taurus molecular cloud is lacking in post-T Tauri stars and also most star forming regions with molecular gas have stellar population ranging from ~ 1 to 3 Myr (Hartmann et al. (2001) and reference therein). Also almost every molecular cloud complex observed contains young stars. Hartmann et al. (2001) therefore argue that star formation follows the formation of the molecular cloud itself by less than 1 Myr. They conclude that large-scale flow in the diffuse ISM can form molecular clouds rapidly and also that stars could form within a single crossing time of the cloud.

From the age dispersion of stars in molecular clouds, Elmegreen (2000) claims that the lifetime of the clouds is of the order of their dynamical time. Elmegreen (2007) covers in details some issues of the rapid collapse and evolution of molecular clouds and also explains why modern observation finds much faster star formation in a simple way: as the resolution of the observations increased, the scale of the objects observed decreased and the smaller clouds are observed to have smaller timescales.

These ideas remain speculative, but it shows that the timescale for star formation and the lifetime of GMCs are still a matter of active debate.

3.1.4 The role of gravity within molecular clouds

The recent success of non-gravitating turbulence simulations of molecular clouds (see Mac Low & Klessen (2004) for a review) to reproduce realistic fragmentation, lead to a new paradigm.

“Clouds and clumps are no longer seen as the result of gravitational instabilities in a region containing a large number of Jeans masses, but simply the result of supersonic turbulence, whatever the source.” (Elmegreen & Scalo, 2004)

This picture, where the clouds and clumps are formed by supersonic turbulence is called “turbulent fragmentation”. Molecular clouds have internal velocities larger than the virial speed (Elmegreen & Scalo, 2004) and therefore the role of gravity must be minimal up to the the molecular cloud scales. Overall, the role of gravity is assumed to be only relevant on large scales via the spiral arms effects that could be driving the turbulence on kiloparsec scale and also, on the smaller scale for the gravitationally bound dense cores.

It was suggested by Elmegreen (1993) that the kinetic energy released via virialization of the bounded cloud could prevent further gravitational collapse. However, an isothermal gas can never reach virial equilibrium because it would require thermal pressure support. So clouds cannot reach equilibrium and stop their gravitational collapse. And the fast decay rate of turbulence measured by simulations, even when including self-gravity and the magnetic field support, suggest that the motions generated by gravitational collapse could not be an efficient turbulence driver (Mac Low & Klessen, 2004). The turbulence decay is assumed to be too fast to significantly support the cloud.

However, we will argue in this chapter that in the case of a gravitationally bounded molecular cloud, gravity can drive the cloud turbulence and maintain supersonic turbulence. Significant turbulence decay applies only for non gravitationally bounded clouds.

3.2 Turbulence Observables

3.2.1 Scaling relation

Using the spectroscopy of a molecular emission line tracing a certain density range, one can measure the velocity dispersion along a line of sight of a molecular cloud. Larson (1981) found a power-law relation between the global velocity dispersion and the molecular cloud size:

$$\Delta v = CL^\alpha \quad (3.1)$$

where $C = 1.1$ and $\alpha = 0.38$. Using a more homogeneous set of data, Solomon et al. (1987) found a similar relation, but with $C = 1.0$ and $\alpha = 0.5$.

Many other methods have been used since then to study the scaling behavior of velocities (see McKee & Ostriker (2007) and references therein). Overall, they all found a power-law exponent close to $1/2$, however the uncertainties on these measurements remain large (e.g. 0.49 ± 0.15 (Brunt et al., 2003)). The main issue with these measurements comes from the difficulty to recover all the statistical properties of a turbulent gas from only the line of sight motions on a 2D projection as well as the limited spatial extend of current observations and the significant noise level (Elmegreen & Scalo, 2004).

3.2.2 Universality of the turbulence

Turbulence is multiscale and has been observed to be remarkably uniform on a wide range of scales, $\sim 0.03 - 30$ pc, see figure 3.1. Heyer & Brunt (2004) measured the velocity dispersion, using Principal Component Analysis (PCA) (Brunt & Heyer, 2002), for 27 giant molecular clouds which represent a good sample of the Galaxy, covering a wide range of cloud sizes, environments and local star formation activity. They found an overall scaling exponent $\alpha = 0.65$, where $\delta v = v_0 l^\alpha$, δv is the velocity difference as defined for the structure function (see section 3.2.4), l is a scale and v_0 is the scaling coefficient. They argue that this apparent uniformity suggest a limited contribution of the localized and non-uniformly distributed driving sources (such as stellar feedback) to the overall turbulence. There is no correlation observed between star formation activity and turbulence. Therefore, the dominating driving source should be more uniform and it could occur on larger scale.

3.2.3 Power spectrum

The power spectrum ($P(k) \propto k^{-\beta}$) is the statistical measure of kinetic energy at different scales. The *steeper* the power spectrum is (i.e. the larger β is), the more power is given to the large modes (small k) and less to the small scales. It is a very fundamental measure to study turbulence and the transfer of energy at different scales.

It is a relatively simple measurement to do for simulations with grid codes. It can be retrieved by simply doing a Fourier transform of the velocities back to k-space. However, it is not as straightforward in our case with a particle-based hydrodynamics code. The Lagrangian nature of SPH simu-

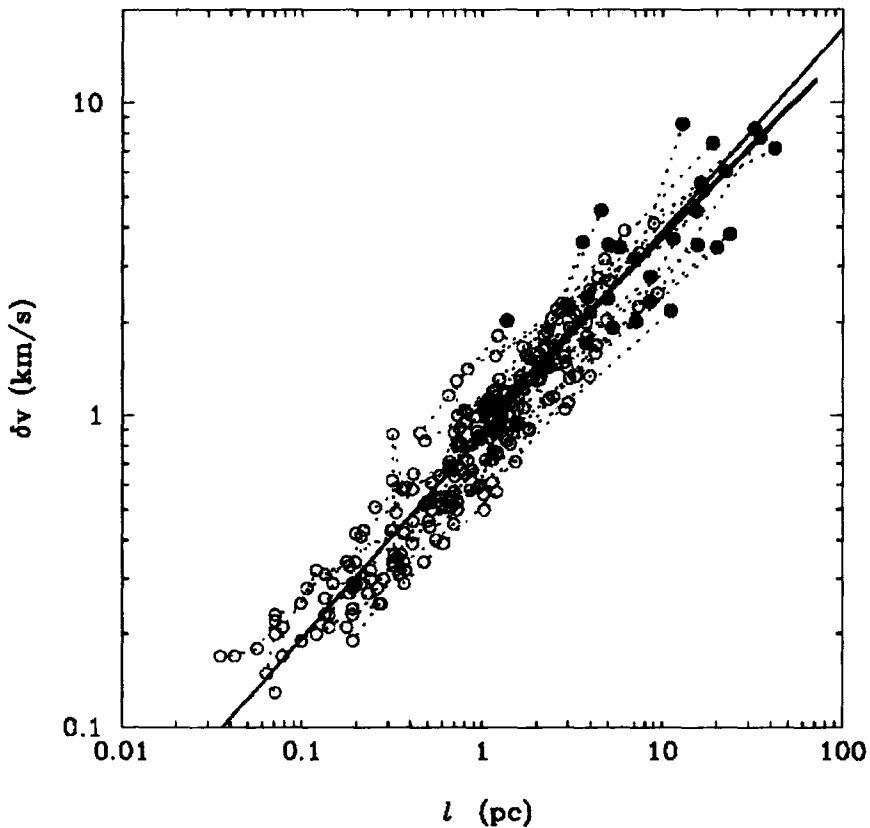


Figure 3.1 The scaling relation of velocity dispersion in function of the scale for 27 different molecular clouds from Heyer & Brunt (2004). The filled circles at the upper end of each dotted line represent the global line-width velocity dispersion as in the Larson relation. The light full line is the bisector fit of all points. The thick full line is the bisector fit of the filled points only. The small scatter of points attest that the power-law relation is followed over a large range of scales.

lations implies that the particles are moving with the gas, and are therefore non-uniformly distributed throughout the simulation area. Also, the non-periodicity of our simulation makes the size of the simulation somewhat arbitrary. Therefore, measuring the velocity power spectrum directly is not trivial. We could always interpolate the particles properties on a grid or weight the velocities by density to solve the particle distribution issues. For the box size,

if we choose a box size of interest around the center of the box, leaving out the low density gas surrounding it, the non-periodicity of that box would create edge effects. Artificial modes would be generated throughout the spectrum by the edges transitions. One way to get around this would be to perform the Fourier transform on a region substantially larger than the whole box. The lack of particles near the edges would act as an artificial periodicity of the box. But it would get computationally intensive to cover this whole range of scales.

It is also not possible to measure it directly from observations because of the lack of 3D information on the gas. Brunt & Heyer (2002) developed a method to observe the velocity structure function of molecular clouds, a related statistical measurement. We chose to use the same structure function technique to measure the power spectra in our simulations.

3.2.4 Generalized structure function

The generalized structure function is a statistical measurement of the p^{th} order velocity differences as a function of a spatial displacement (\mathbf{l}) on a velocity field (Monin & Yaglom , 1975).

$$S_p(l) \equiv \langle |\mathbf{v}(\mathbf{r} + \mathbf{l}) - \mathbf{v}(\mathbf{r})|^p \rangle \quad (3.2)$$

where the averaging is computed over every \mathbf{r} and every \mathbf{l} , making it a calculation of the N^{th} order, where N is the number of particles. The structure function can also be broken in the longitudinal ($\mathbf{v} \parallel \mathbf{l}$) and transverse ($\mathbf{v} \perp \mathbf{l}$) components, where

$$S_p^{\parallel}(l) \equiv \left\langle \left| \frac{(\mathbf{v}(\mathbf{r} + \mathbf{l}) - \mathbf{v}(\mathbf{r})) \cdot \mathbf{l}}{|\mathbf{l}|} \right|^p \right\rangle \quad (3.3)$$

$$S_p^{\perp}(l) = \sqrt{S_p^2 - S_p^{\parallel 2}} \quad (3.4)$$

These structure functions are all approximately power laws in the inertial range (see section 3.1.2) (Kritsuk et al., 2007), since they relate velocity to scale and, in the inertial range, the kinetic energy transfer to smaller scale is known to scale as a power law.

$$S_p(l) \propto l^{\zeta_p} \quad (3.5)$$

The second order of this function is of special interest for us, since it is related to the auto-correlation function ($C(l)$) (Heyer & Brunt, 2007; Pope , 2000).

$$C(l) \equiv \langle \mathbf{u}(\mathbf{r}) \cdot \mathbf{u}(\mathbf{r} + \mathbf{l}) \rangle \quad (3.6)$$

$$\begin{aligned} S_2(l) &\equiv 2(C(0) - C(l)) \\ &\equiv 2 \int_0^{\infty} (1 - \cos(\omega l)) E(\omega) d\omega \end{aligned} \quad (3.7)$$

The auto-correlation function is the real space Fourier transform of the velocity power spectrum ($P(k) \propto k^{-\beta}$). Therefore, by finding the power law index of the second order structure function (ζ_2), we can find the power spectrum index (Kritsuk et al., 2007; Pope , 2000).

$$\beta = \zeta_2 + 1 \quad (3.8)$$

The transverse (rotational) and the longitudinal (compressible) modes of turbulence can feed each other (Sasao, 1973). At low Mach number ($c_s > \langle |v| \rangle$) the flow is incompressible, so one would expect the turbulence to be mostly transverse. Inversely, at very high Mach number ($c_s \ll \langle |v| \rangle$), one would expect mostly longitudinal turbulence (Elmegreen & Scalo, 2004). It was predicted that the longitudinal to transverse ratio would increase with M^2 , for low Mach numbers (Bataille & Zhou, 1999).

Numerical simulations (Nordlund & Padoan, 2003; Vazquez-Semadeni et al., 1996; Boldyrev et al., 2002; Porter et al., 2002) found a wide range of ratios ($S_p^{\parallel}/S_p^{\perp}$) from < 1 to 10 , where the end result is influenced by the forcing, the initial ratio, the Mach number, the magnetic field strength and the cooling (Elmegreen & Scalo, 2004). The artificial forcing is usually set up to be transverse, since the longitudinal modes create shocks and are assumed to dissipate quickly. The transverse modes are therefore longer lasting.

The first order structure function is also of interest, since this is what is directly observed, the velocity dispersion (δv).

$$S_p(l)^{1/p} = \delta v = v_o l^{\gamma_p} \quad (3.9)$$

$$\gamma_p = \zeta_p/p \quad (3.10)$$

The variations of γ_p with p provide further information about the dissipative structures of a fluid (Boldyrev et al., 2002). However, non-intermittent

fields, where the flow is everywhere turbulent (Pope , 2000) and there is no transition between turbulent to non-turbulent regions, have less extreme velocity fluctuations over l (Brunt et al., 2003), and the relation is linear ($\gamma_p = \gamma$), where γ is a constant.

$$\gamma = \zeta_p/p \tag{3.11}$$

And this γ is related, more generally, to the power spectrum of the velocity field.

$$\beta = 2\gamma + 1 \tag{3.12}$$

Therefore, in theory, any order of the structure function allow us to determine the power spectrum of the turbulence. But this is based on the assumption of non-intermittence of our velocity field. Intermittence is a behaviour caused by a departure from the scale-invariance of the turbulent field (Biskamp , 2003). The exact scaling would require “intermittency corrections” ($\gamma = \zeta_p/p\mathcal{C}_p$) (Boldyrev et al., 2002; Merrifield et al., 2005), but these are small for the lower orders ($p \leq 3$) (Kritsuk et al., 2007). The comparison with the second order structure function is also more direct, see equation 3.7.

For incompressible turbulence, Kolmogorov (1941) predict a scaling exponent of $\zeta_p = p/3$. The high resolution simulations of compressible turbulence (Kritsuk et al., 2007) found a scaling exponent significantly higher than these predictions for the incompressible limit.

3.2.5 Observed power spectrum

The index α in the velocity dispersion and size observed relation ($\Delta v \propto l^\alpha$), is generally considered equivalent to the structure function scaling exponent (γ). However Brunt & Heyer (2002) from a series of models consider a correction ($\alpha = 0.66\gamma + 0.28$ for $1 < \beta < 3$) is required for a strict comparison of the intrinsic velocity field to the observable measures. The observed width of a spectral line does not depend only on velocity, but also on the density, temperature and abundance of the molecular gas which may vary along the line of sight.

Using equation 3.12, the velocity dispersion-size relation, discussed in section 3.2.1, can be used to infer the power spectrum of the turbulence. Taking the scaling relation observed by Brunt et al. (2003) $\alpha = 0.49 \pm 0.15$ we get $\beta \approx 1.68 - 2.28$. These measurements are therefore in a relatively good agreement with a Burgers turbulence ($\beta \approx 2$).

3.2.6 Density Probability Density Function

Another known property of supersonic isothermal turbulence is its near log-normal density probability density function (PDF) (Vazquez-Semadeni, 1994; Padoan et al., 1997; Nordlund & Padoan, 1999). This property has been derived theoretically by Pope & Ching (1993). The standard deviation (σ_{PDF}) of the distribution is also known to increase (Nordlund & Padoan, 1999) with the Mach number of the turbulence.

$$\sigma_{PDF}^2 = \ln(1 + b^2 \mathcal{M}^2) \quad (3.13)$$

Numerical simulations in 2-D (Vazquez-Semadeni, 1994) and 3-D (Padoan

et al., 1997) have also reproduced these features. Supersonic non-magnetized isothermal turbulence simulations by Kritsuk et al. (2007) found a value of $b \approx 0.260$.

3.3 Initial Conditions

We performed SPH simulations of a typical molecular cloud with 5000 solar masses. The gas was set to be isothermal with a temperature of 10K, which is the temperature expected from dust radiative transfer models (Stamatellos et al., 2007). We used a mean molecular weight of 2.33, a commonly used value (e.g. Motte et al. (1998); Offner et al. (2008)). We used 36 million particles, each with $m = 1.3855 \times 10^{-4} M_{\odot}$. Initially, the molecular cloud is a sphere of uniform density $n_{init} = 300 \text{cm}^{-3}$. It has an initial diameter of 8 parsec. The freefall time ($t_{ff} = \sqrt{(3\pi)/(32Gn_{init})}$) for this cloud is 1.9 Myr.

In these simulations, without sinks, we wanted to focus on the early period of star formation, where stellar feedback is not yet an issue. We could therefore let the simulations evolve until $\sim 1 - 2$ very dense objects formed. At this point, the simulations were getting significantly slower, by a factor ~ 60 . These dense objects were generally found in dense filamentary structures, where multiple objects were also forming. The feedback from these forming stars would therefore significantly affect their surrounding (Bate, 2008). This was the ideal point for us to halt our simulations. Our 4 simulations reached this point around 135 kyr, so this was the stopping time we chose.

3.3.1 Anisotropic Turbulent Velocity Field

In the Bate et al. (2003) and our previous (chapter 2) simulations, the initial conditions were uniform density spheres with turbulent velocity fields (see section 3.3). No large scale modes, larger than the initial simulation, was included, a condition that is imposed on periodic simulations. In nature however, nothing indicates that such modes wouldn't be present. These modes, larger than the whole cloud, can dictate the overall collapse of the cloud leading to anisotropic cloud collapse.

To generate more realistic molecular clouds initial conditions, we included here large scale turbulent modes. To do so we modified the code used in section 2.2.2, to select only a section of the whole velocity field grid. We selected a region of radius $l/8$, where l is the size of the initial grid. We chose this section to get modes significantly larger than the whole cloud. On the other hand, choosing a much smaller section of the velocity field would reduce the resolution of the resulting velocity field too much. The original velocity field used had a resolution of 256^3 , so the velocity field with large modes had a resolution of 64^3 .

The whole velocity field was created with a uniform RMS Mach number of 13.42, in order to balance the gravitational and kinetic energy, E_{Grav} and E_{Kin}

$$|E_{Grav}| = |E_{Kin}| \quad (3.14)$$

$$\left| -\frac{3}{5} \frac{GM^2}{R} \right| = \left| \frac{M\langle v \rangle^2}{2} \right| \quad (3.15)$$

$$\langle v \rangle = \sqrt{\frac{6GM}{5R}} = 13.42 \quad (3.16)$$

where initially $M = 5000M_{\odot}$ and $R = 4pc$. This insures that the cloud will be at least marginally bound. If the kinetic energy is much higher the cloud will disperse instead of collapsing. If they are at equilibrium, some the initial turbulence will decay and the cloud will start to collapse gravitationally. By selecting only a section of the initial velocity field, the initial RMS Mach number of our simulations is however allowed to vary.

3.3.1.1 Shear vectors

To be able to predict the overall shape of collapse, we need to measure the anisotropy of the shear in that region. To do so, we first normalize our velocity matrices V_x , V_y and V_z , such that $V_{x,y,z} = V_{x,y,z} - \bar{V}_{x,y,z}$. Then we calculate the averaged shear matrix (i.e. the averaged deformation gradient tensor $a_{ij} = \frac{\partial \bar{V}_i}{\partial X_j}$).

$$\mathbf{A} = \begin{pmatrix} \frac{\partial \bar{V}_x}{\partial x} & \frac{\partial \bar{V}_x}{\partial y} & \frac{\partial \bar{V}_x}{\partial z} \\ \frac{\partial \bar{V}_y}{\partial x} & \frac{\partial \bar{V}_y}{\partial y} & \frac{\partial \bar{V}_y}{\partial z} \\ \frac{\partial \bar{V}_z}{\partial x} & \frac{\partial \bar{V}_z}{\partial y} & \frac{\partial \bar{V}_z}{\partial z} \end{pmatrix} \quad (3.17)$$

In order to get real eigenvalues, we need \mathbf{A} to be a symmetric matrix, $\mathbf{A} = \mathbf{A}^T$, i.e. $a_{ij} = a_{ji}$. To do so we applied the following transformation:

$$a_{ij} = \frac{a_{ij} + a_{ji}}{2} \quad (3.18)$$

Then we calculate the eigenvalues and eigenvectors, using the IDL standard function *la_eigenproblem* which is based on the standard LAPACK rou-

tines. This function solves the problem $\mathbf{A}\vec{X}_{1,2,3} = \lambda_{1,2,3}\vec{X}_{1,2,3}$ and returns the eigenvectors $\vec{X}_{1,2,3}$ which represent the new base of orthogonal vectors, and the eigenvalues $\lambda_{1,2,3}$ which represent the amount of shear in those directions.

3.3.1.2 Anisotropic collapse shapes

Positive shear in a given direction in our simulations will translate into an expansion and a negative value into a contraction. We can imagine 3 different shapes for the anisotropic collapses: filament, sheet and ribbon. A filamentary collapse would happen if we get expansion in one direction, and contraction in the other 2 orthogonal directions, see figure 3.2 a). A sheet shaped collapse would happen if we get expansion in 2 orthogonal directions and a compression in the other direction (figure 3.2 b)). And a ribbon shaped collapse would happen if we have expansion in one direction, compression in an other and no shear at all in the other (figure 3.2 c)).

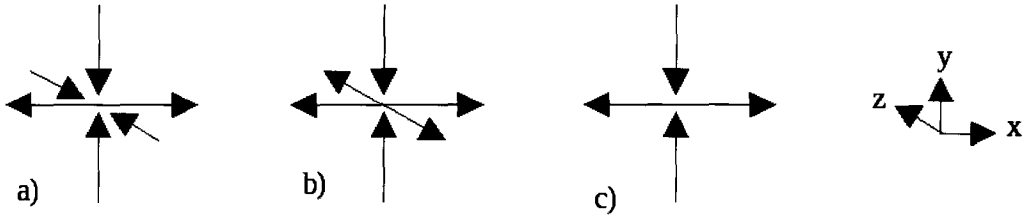


Figure 3.2 Schematic view of the 3 possible configurations of shear vectors. Configuration a) represents a filament collapse, b) a sheet and c) the ribbon case.

For incompressible modes, the sum of the 3 eigenvalues is zero ($\lambda_1 + \lambda_2 + \lambda_3 = 0$) and if we normalize them we get $(\lambda_1, \lambda_2, \lambda_3) = (1, -0.5, -0.5)$ for the ideal filament case, $(0.5, 0.5, -1)$ for the sheet and $(1, 0, -1)$ for the ribbon.

3.3.1.3 Large and small scale turbulence

To be able to make a statistical study of the anisotropy (see section 3.3.1.4), we want to create a set (20,000) of randomly generated initial conditions. To generate so many in a reasonable amount of time, we need to use a lower resolution, but for the initial conditions we will run the simulations with, we need the full resolution. Therefore, we want to be able to create turbulence grids at different resolutions and keep the same shear values, for a given random seed. The IDL random number generator function *randomu* provide a fixed list of pseudo-random numbers for a given seed value. This is very useful to us since we can easily reproduce the same turbulence field; if we use the same seed, the same pseudo-random values will be returned.

Since the overall shear is dictated by the large scale turbulence, we need to make sure all the larger scale modes get created with the same random numbers no matter which resolution is used. To do so we use 2 seeds, *seed1* for the large scale modes and *seed2* for the smaller scale. Basically, *seed1* covers all the modes generated in a 64^3 grid and *seed2* covers all the smaller modes added when we increase the grid resolution. We kept the same *seed2* for every initial conditions we created, in order to avoid the random effect the small scale turbulence could have on the simulations. Note that with this method the small scale turbulence would change if we modify the resolution, because the random numbers returned by *seed2* wouldn't coincide to the same modes. However, this was not something we had to worry about, since we only need the large modes, defining the anisotropy, to be the same when using better resolution.

3.3.1.4 Statistical study of anisotropy

Assuming molecular clouds have random turbulence with modes larger than the whole cloud, we can determine which of these ideal cases is most likely to be observed. We created a set of 20,000 initial conditions with low resolution random initial velocity fields. We then measured the global shear vectors for each one of them. On figure 3.3 we plot the shear vectors λ_1 vs λ_3 for each realisation, and this represents all the shear information since $\lambda_2 = -(\lambda_1 + \lambda_3)$. The vectors are in Mach units and the overall RMS Mach number of the velocity fields was set to 6.37. We set $\lambda_1 > \lambda_2 > \lambda_3$ and this way we can look at the statistical distribution of the shear. The ideal ribbon case would lie where $\lambda_1 = -\lambda_3$ and $\lambda_2 = 0$, therefore near the middle of the distribution. The ribbon initial conditions we choose for our simulation is identified by the filled square. The ideal filament case would have a large expansion vector (λ_1) and two approximately equivalent contraction vectors (λ_2 and λ_3). This case is located on the top right of the distribution, the upside down filled triangle represent our choice for our filament initial conditions. The ideal sheet case would have a large contraction vector (λ_3) and two approximately equivalent expansion vectors (λ_1 and λ_2). This case is located at the bottom left of the distribution. Our choice of sheet initial conditions is represented by the filled triangle. The ideal spherical case would obviously have the smallest shear vectors as possible and would therefore be located at the bottom right corner of the distribution.

The contour lines of the distribution clearly show that the most likely scenario is the ribbon collapse. For the filament and the sheet initial conditions, we choose reasonable cases at $\sim 2\sigma$, but for the spherical case we

choose an extreme case (empty circle) at more than 4σ from the maximum to represent the case with minimal shear.

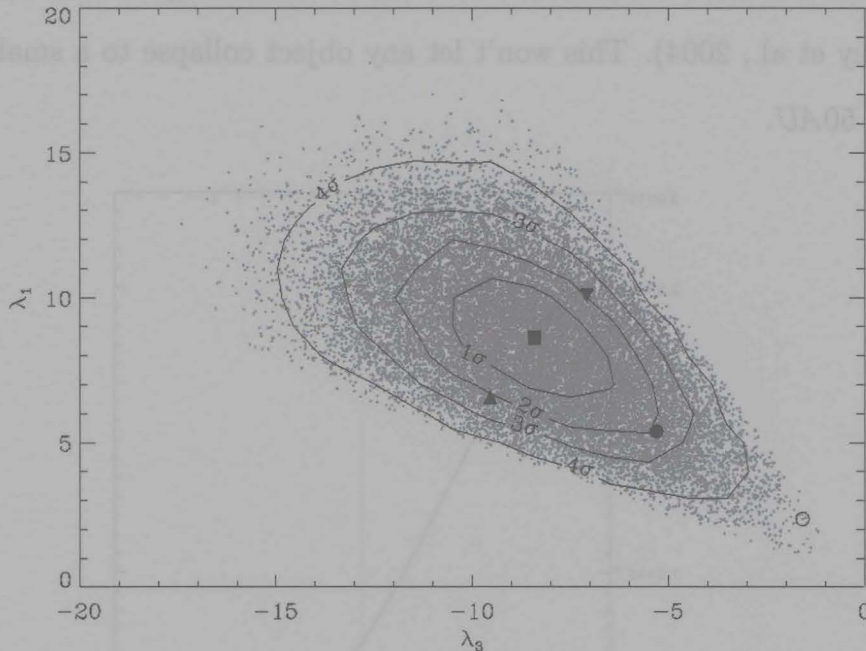


Figure 3.3 Statistical distribution of the shear vectors λ_1 and λ_3 , where $\lambda_1 > \lambda_2 > \lambda_3$ and $\lambda_1 + \lambda_2 + \lambda_3 = 0$. The contour lines show the variations of a standard deviation from the maximum likelihood. The filled square represent the initial conditions chosen for the ribbon case, the filled upside down triangle represent the filament case, the filled triangle represent the sheet case and the open circle represent the spherical case.

3.3.2 Resolution Limit for Density Peaks

We wish to avoid the simulations reaching very high densities in the cores, slowing down the code tremendously. We also wish to avoid the potential “numerical errors” created by using “sink particles”, see section 2.1.5. We choose to limit our gravitational resolution (softening; $\epsilon_{Soft} = 50AU$). This way, the gravitational forces between two particles closer than 50 AU from

each other won't be calculated, but fixed by the softening profile (see equation 2.8 and figure 3.4). In GASOLINE, the softening profile is a spline function, which has the same form as the SPH kernel used for gas forces calculations (Wadsley et al., 2004). This won't let any object collapse to a smaller radius than $\sim 50AU$.

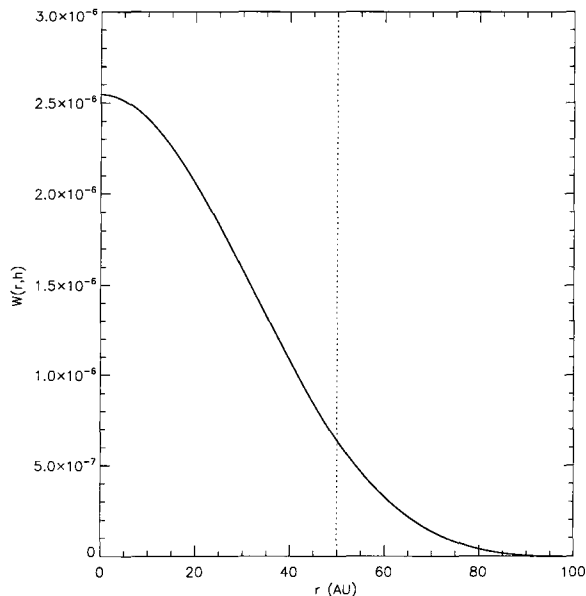


Figure 3.4 Kernel function used by GASOLINE for the smoothing and softening profiles. The softening or smoothing chosen here is $h = 50AU$ shown by the dotted line.

However, this can still let density increase significantly within that object. As mention in section 2.1.5, when density increases the smoothing length decreases, and the timestep decreases with the smoothing length. So we had to impose a constraint on the minimal smoothing length (h_{min}) also.

$$h_{min} = \epsilon_{Soft} = 50AU \quad (3.19)$$

This will enable us to continue running the simulations further, after

the first core is formed. Given that observations of star forming cores today have resolution ranging around ~ 1000 AU, we still have enough resolution to be able to compare our simulations to the observations.

This change will not affect the dynamics of the low density gas. Only the very dense self-gravitating regions of radius ~ 50 AU would be unresolved. Such an object would not be able to collapse any further, it could however still accumulate mass. The density range where this kind of effect would be important is where there is one or more particle(s) per $(50\text{AU})^3$, $n_{max} \approx 4 \times 10^7 \text{ cm}^{-3}$. The typical density reached in shocks is in the range 10^{4-5} cm^{-3} , quite far from this critical density. Figure 3.5 shows the maximal density resolved

$$n_{max} = \frac{3M_{ptcle}}{4\pi h^3} \quad (3.20)$$

in function of h , the softening resolution. Our choice of 50 AU is indicated by the dotted lines. The dash-dot lines represent the typical range of density reached by the shocks. The bottom panel shows the minimal Jeans mass

$$M_J^{min} = \frac{\pi c_s^3}{6\sqrt{G^3 n_{max}}} \quad (3.21)$$

we can resolve. A resolution of 50 AU, therefore allow us to resolve objects with Jeans masses as low as $\sim 0.01M_\odot$. At the resolution limit, fragmentation is suppressed, we therefore avoid “artificial fragmentation” (Truelove et al., 1997) issues. And given our intention to compare to observations of cores, this is not problematic.

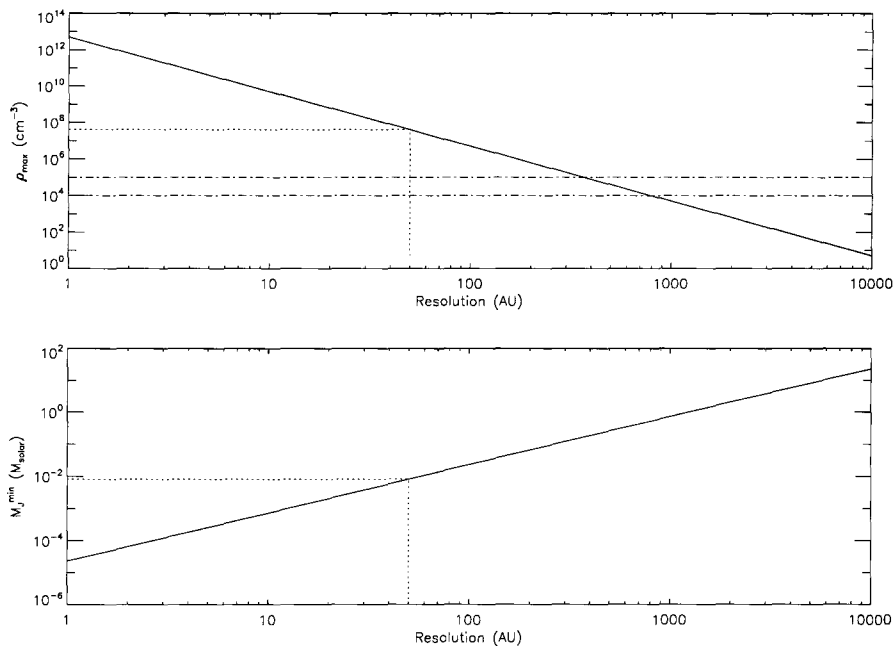


Figure 3.5 Maximal density resolved in function the softening resolution. Our choice of 50 AU is indicated by the dotted lines. The dash-dot lines represent the typical range of density reached by the shocks. The bottom panel shows the minimal Jeans mass we can resolve.

3.4 Results

3.4.1 Turbulence Magnitude Evolution

We first investigate how the magnitude of turbulence evolves in time. We plot in figure 3.6 (top panel) the RMS Mach number for the 4 simulations: spherical, ribbon, filament and sheet. Each initial condition were created from velocity fields with the same RMS Mach number. When we selected only a section of the velocity field to create the anisotropy, the resulting RMS Mach number could vary slightly, because turbulence is not uniform. We found our initial RMS Mach number values ranging between 6.2 to 7.7. The spherical case has a particularly low initial value and the other 3 cases have similar

initial values. This should however not be an issue, as long as our initial turbulence is supersonic and below the energy balance. That would require a Mach number of 13.42 (see equation 3.16). This is to insure that the cloud is bounded and undergo gravitational collapse. An interesting feature this allow us to observe is that every simulation, regardless of their initial turbulence, ends up around a Mach number of ~ 8 , which is around 60% of the energy balance value.

Figure 3.6 (bottom panel) shows the evolution of the half mass radius ($R_{M/2}$), and we see that the clouds are indeed under gravitational collapse. One thing that stands out of this figure is that the run with lower kinetic energy, the spherical case, also has the fastest rate of collapse.

To investigate the relation between the magnitude of turbulence and the rate of collapse further we ran 2 more simulations, with identical initial conditions to the spherical case, but with different initial RMS Mach number values, one lower (0.9 Mach) and one higher (13.5 Mach). The results are shown on figure 3.7. The run with lower Mach number collapses at a significantly higher rate and also, due to the low turbulence, it doesn't undergo turbulent fragmentation and form cores, slowing down the simulation, until much later (~ 185 kyr).

The situation is much different for the run with higher Mach number. The turbulence is decaying slowly over time and since the kinetic energy is higher than gravitational energy, the cloud is expanding instead of collapsing.

These 3 simulations also all converge around a Mach number of ~ 8 . However we can't run the simulations long enough to see if the simulations would start to oscillate and converge around this value. This would really indicate a preferential value for molecular clouds undergoing gravitational col-

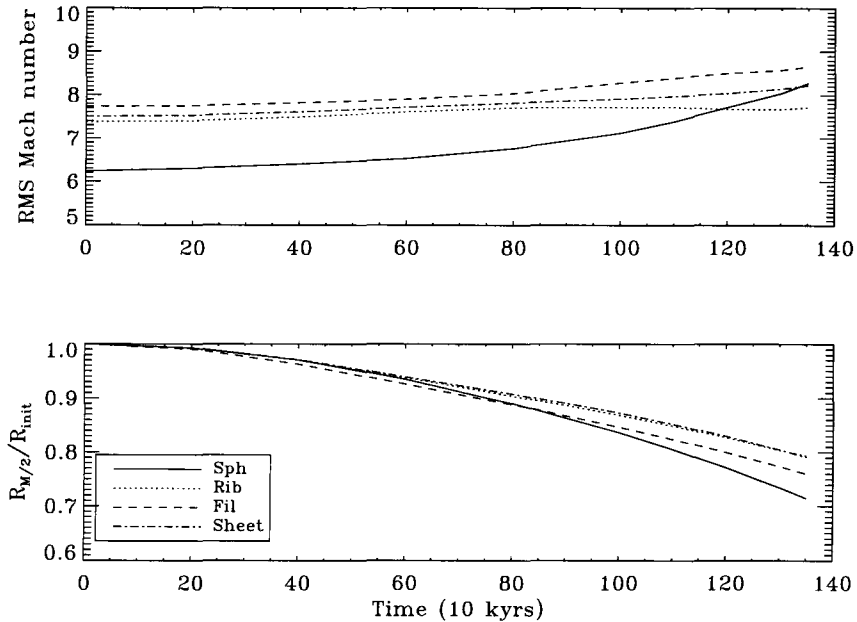


Figure 3.6 Evolution of the RMS Mach number (top panel) and of the half mass radius (bottom panel) for each simulation: the spherical case (full line), the ribbon case (dotted line), the filament case (dashed line) and the sheet case (dashed dot line). This figure shows how the potential energy is converted during the collapse to maintain or even increase the turbulent kinetic energy.

lapse.

Figure 3.6 and 3.7 shows that gravitational collapse can inject a significant amount of kinetic energy back to the cloud. If the energy ratio E_{Kin}/E_{Grav} is $\ll 1$ the cloud will undergo gravitational collapse at a rate close to freefall and a large amount of kinetic energy will be re-injected to the cloud. It's unclear however if this low turbulence situation can realistically happen in nature. A cloud with an energy ratio > 1 , will expand at least until its turbulence decays to reach the energy ratio of 1. However the high initial level of turbulence will stimulate turbulent fragmentation and at least locally form dense cores even earlier (~ 115 kyr for our run with 13.5 Mach).

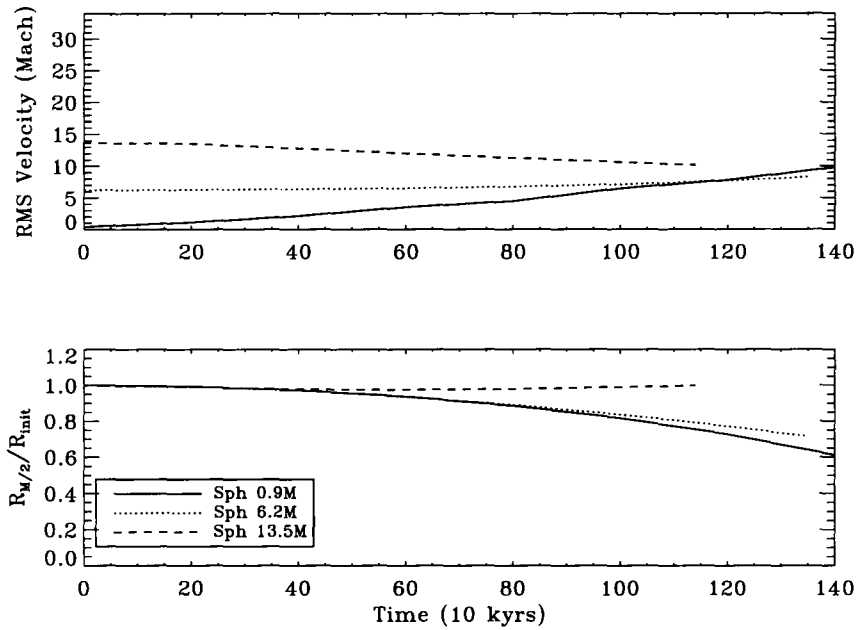


Figure 3.7 Evolution of the RMS Mach number (top panel) and of the half mass radius (bottom panel) for the spherical case with RMS Mach number 0.9 (full line), 6.2 (dotted line) and 13.5 (dashed line).

For a cloud with an energy ratio close to, but slightly lower than 1, we find that the gravitational collapse can maintain or increase significantly the turbulence Mach number. Turbulence in return slows down the rate of collapse of the cloud by providing support to the cloud. This implies that gravitationally bounded molecular clouds turbulence can be largely driven by gravitation alone.

To find out whether this kinetic energy increase is purely due to the infall motion or if it is real turbulence, we will look at more properties of the clouds.

3.4.2 Energy distribution

We investigate where the kinetic energy is distributed in the simulation. We want to find out if it is dominated by the rotation or the translation movements of very dense objects, by the in-fall or drift of the low density gas or if it is well distributed on all density scales. The later would be expected from a turbulent gas.

We plot in figure 3.8 the Mach number as a function of the density for each particle of the spherical case simulation. Since every particle has the same mass, the velocity is directly tracking the kinetic energy. Figure 3.8 shows a log-normal density distribution. The Mach number distribution has no bias toward high or lower density gas. This distribution is in very good qualitative agreement with the isothermal supersonic turbulence simulations by Kritsuk et al. (2007).

In figure 3.9 we plotted the same properties on a log-linear scale and for each simulation. For the spherical case, we get a clear normal distribution of the Mach number, which is consistent with what is known about isothermal supersonic turbulence. We expect a log-normal density PDF of width scaling approximately linear with the Mach number (Nordlund & Padoan, 1999).

A similar distribution is observed for the 3 anisotropic cases, except they all exhibit a slight tilt, with dense regions having lower Mach number and low density regions having higher Mach number. This is due to the anisotropic nature of the initial turbulence. The large scale shear forcing regions of the cloud to shock would create the increase in dense gas with low kinetic energy. And the large scale shear forcing regions of the cloud to expand would create the increase in low density gas with high kinetic energy.

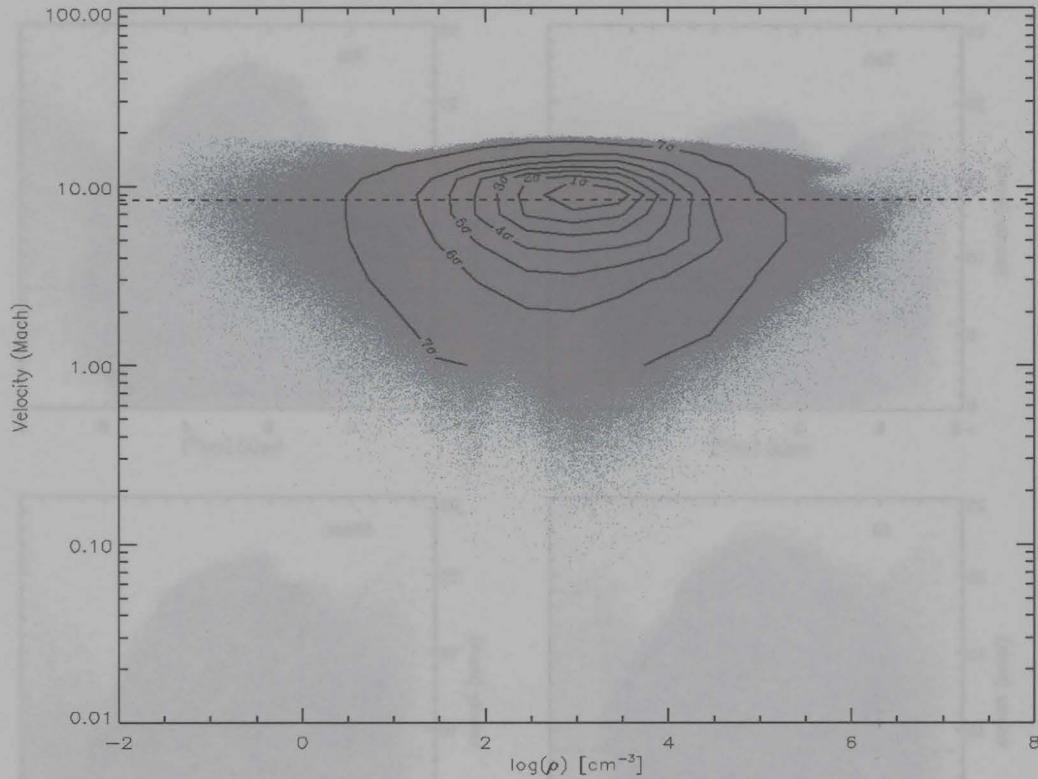


Figure 3.8 Mach number distribution of the gas particles in function of density. Every particle of the spherical case simulation is plotted on a log-log scale and the 1σ contour lines are over-plotted. The RMS mach number is represented by the dashed line.

3.4.3 Probability Distribution Function (PDF)

The density PDF allow us to trace the density distribution of the gas throughout the simulation. In figure 3.10, we fit the density PDF at the final stage of each run (135 kyr) with a log-normal (dashed line). The best fit values for the mean μ and the standard deviation σ are indicated on each plot. The fit was done with a \sqrt{N} statistical weighting. The spherical case fit a log-normal with $\sigma_{PDF} = 0.813552$ almost perfectly, except in the low density range. Every density PDF has an excess in low density particles, due to the open boundary of the simulation. These are the very low density particles escaping the cloud

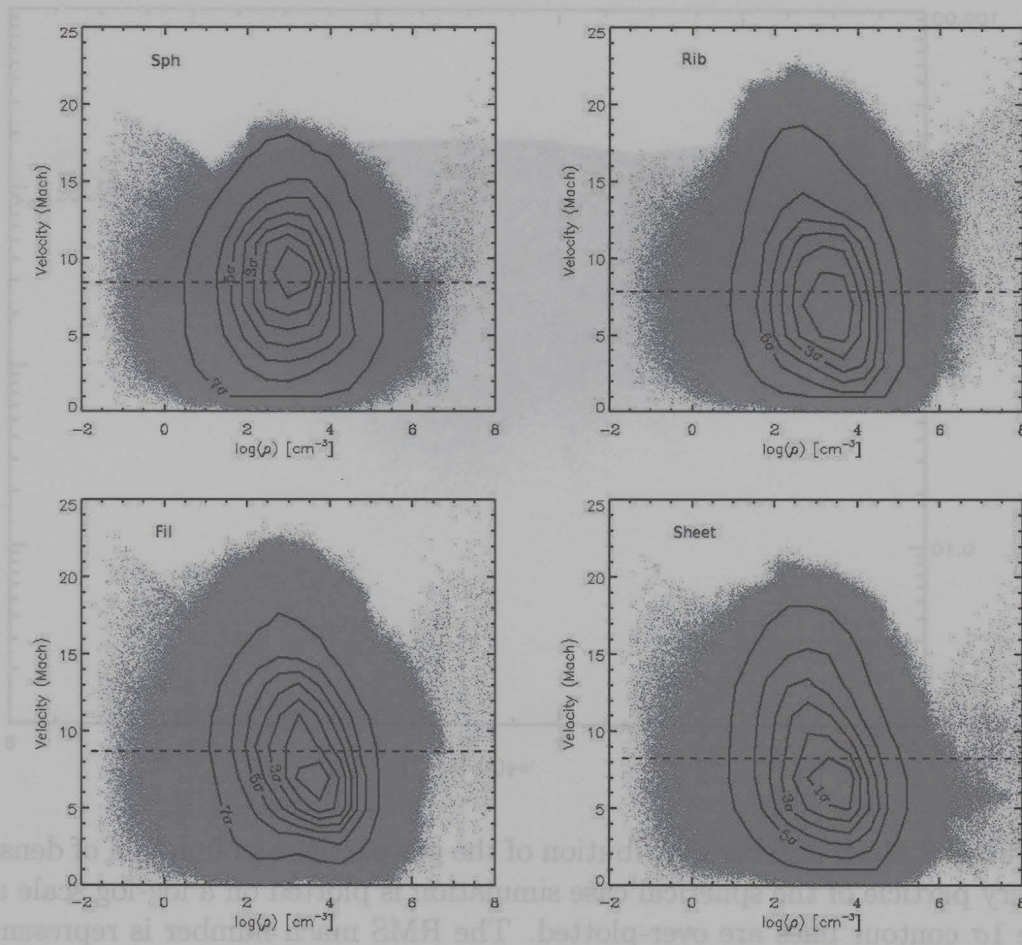


Figure 3.9 Mach number distribution of the gas particles in function of density for the spherical case (top left), the ribbon case (top right), the filament case (bottom left) and the sheet case (bottom right). Every particle of the simulation is plotted on a log-linear scale and the 1σ contour lines are over-plotted. The RMS Mach number is represented by the dashed line.

near the edges.

The 3 simulations with anisotropic turbulence show a density PDF that is close to log-normal, but with a negative skew. This is consistent with what was observed in figure 3.9 and is likely due to the same phenomena. The large scale shock created by the anisotropy generates an excess in high density gas. A negative skew in the density PDF was also observed by Schmidt et al. (2008)

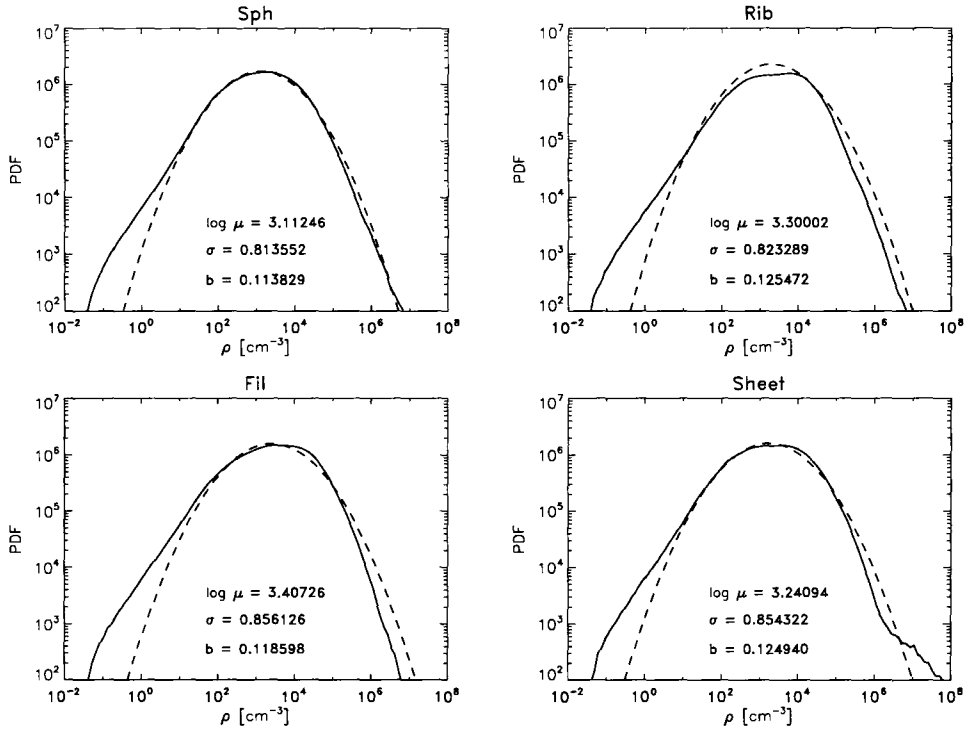


Figure 3.10 Density PDF at the final timestep (135 kyr), for each simulations: spherical, ribbon, filament and sheet cases. The dashed lines represent the best fit of a log-normal with mean μ and standard deviation σ , the parameter b is also calculated for each run.

in simulations of compressively driven isothermal turbulence. This feature was attributed to the compressive nature of turbulence generating more dense regions than transverse turbulence. Our results are therefore in qualitative agreement, since our simulations with larger anisotropy necessarily had more compressive turbulence and showed a skewed density PDF.

The parameter $b = \sqrt{(e^{\sigma^2} - 1)/M^2}$ (see equation 3.13) is also calculated for each run, where M is the RMS Mach number. Our results vary between 0.11 and 0.13.

A group in Potsdam is conducting a comparative study of turbulence decay simulations (<http://www.aip.de/~spsyros/turbulence/>) using differ-

ent grid and particle codes (Spyros Kitsionas, Ralf Klessen and Katharina Jappsen (GADGET), Wolfram Schmidt and Jens Niemeyer (PROMETHEUS), Jonathan Dursi (FLASH A), Jongsoo Kim (TVD), Rob Piontek (ZEUS), Christoph Federrath (ENZO), Daniel Price (PHANTOM), Steffi Walch and Pawel Ciecielag (FLASH B), Steffi Walch and Matthias Gritschneider (VINE). Their initial condition is a fully established isothermal supersonic turbulence with a Mach number of 3.2 and a power spectrum of $P(k) \propto k^{-2}$. We used their initial conditions to compare, and fit a log-normal to the density PDF. We found the best fit with $\sigma_{PDF} \approx 0.55$ leading to a $b \approx 0.1857$. This is smaller than the value found by Kritsuk et al. (2007), $b \approx 0.260$. Our b values are comparable, but even smaller than the Potsdam value.

To investigate this discrepancy, we also looked at the time evolution of the density PDF, see figure 3.11. From light grey to black we plotted the density PDF at 20, 60, 100, 120 and 135 kyr. The distribution is very peaked initially since we start with a uniform density and then it widens to be approximately log-normal.

In figure 3.12 we plotted the evolution of the standard deviation as a function of the Mach number. Every simulation shows a quick initial increase in σ_{PDF} as it leaves the state of uniform density. Then 3 of the simulations (spherical, filament and sheet cases) shows a linear increase. However the slopes, representing approximately the parameter b , are very different, ranging from 0.18 to 0.73. The ribbon case doesn't increase its RMS Mach number, but its σ_{PDF} keeps increasing nonetheless. It seems from this, that our turbulence is not fully developed; the turbulence is not in a equilibrium state with its driving force and the statistical measures, like the Mach number or the density PDF, are still changing with time. This would probably explain why our b

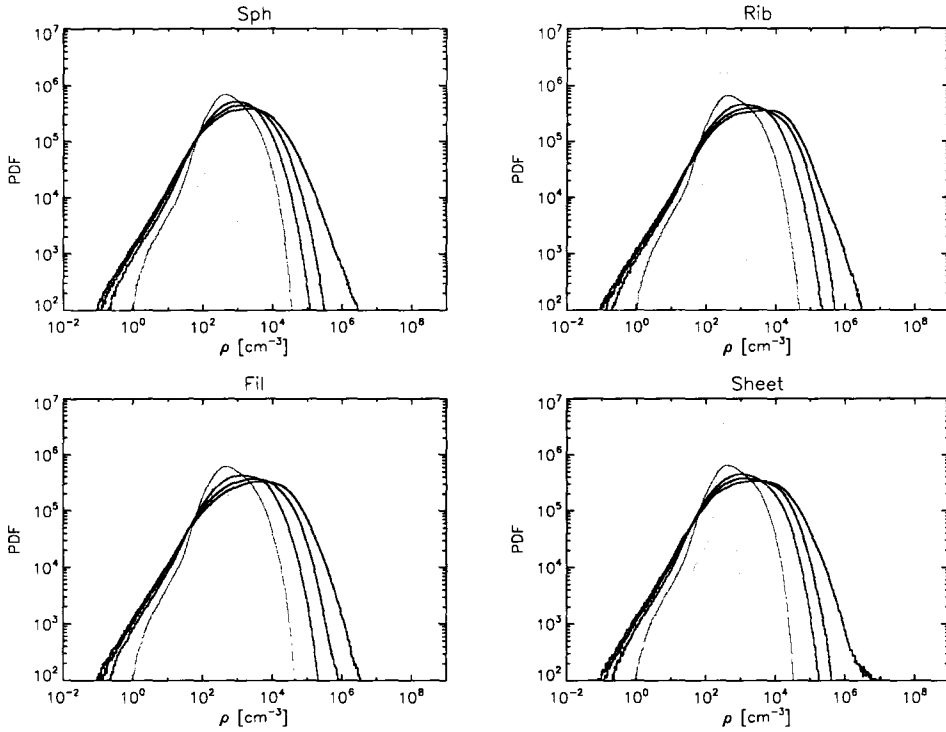


Figure 3.11 Density PDF evolution for each simulations: spherical, ribbon, filament and sheet cases. The evolution goes from light grey to black and the timesteps represented are 20, 60, 100, 120 and 135 kyr.

values are low (figure 3.10), since a larger σ_{PDF} for a given Mach number would give us a larger b . The Potsdam group reported that their initial conditions that were driven for $2 t_{ff}$ were not fully developed. They had to drive it for $4 t_{ff}$ for the turbulence to be fully developed. The turbulence in our simulation is therefore certainly not fully developed even though most of its properties are already in good agreement with the turbulence theory.

3.4.4 Velocity Structure Functions

The velocity structure function is another observable of turbulence. The index α in the observed velocity dispersion and size relation ($\Delta v \propto l^\alpha$), is considered

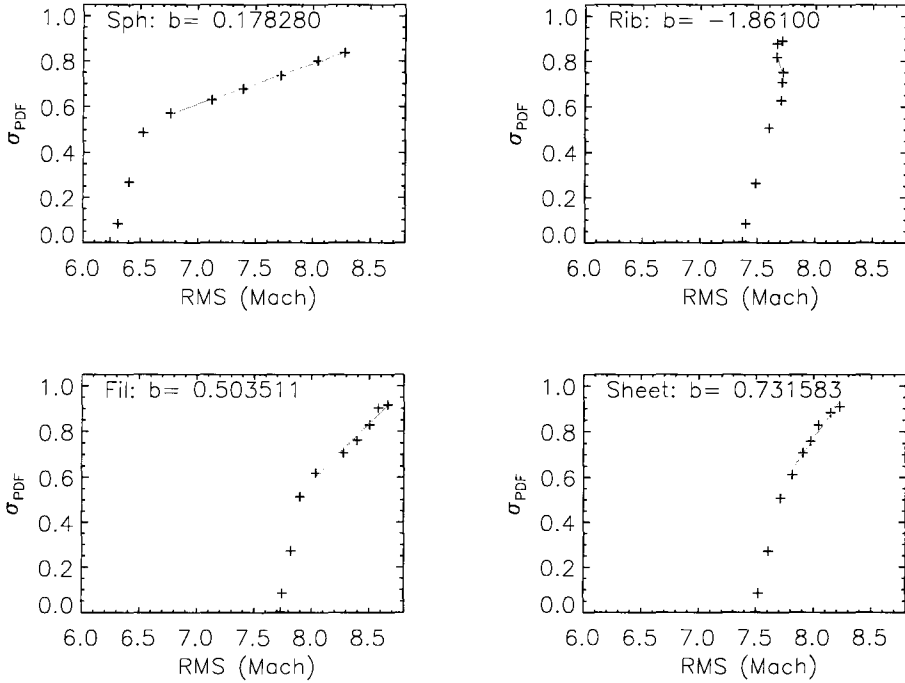


Figure 3.12 The standard deviation of the density PDFs in function of the Mach number for each simulations. The crosses represent the timesteps: 0, 20, 40, 60, 80, 100, 110, 120, 130 and 135 kyr. The dashed line represent the linear fit to the last 6 data points, the slope (b) is also indicated.

equivalent to the structure function scaling exponent (γ), see section 3.2.5. And the most direct relation is with the second order structure function scaling exponent $\gamma = \zeta_2/2$.

The velocity structure function is a measure of the velocity difference, to the power p , in function of the spatial displacement (l), see section 3.2.4. The averaging here is performed over the volume. In order to not over-represent the dense regions containing more particles, we had to weight the velocity difference moments (δv) by the density of the particles.

$$\delta v = |\mathbf{v}(\mathbf{r} + \mathbf{l}) - \mathbf{v}(\mathbf{r})| \quad (3.22)$$

Table 3.1. List of the fit to the slopes of the transverse (ζ_p^\perp) and longitudinal (ζ_p^\parallel) structure functions ($p = 1, 2$ and 3) for the initial and final stage of each simulations.

Case	Time (kyr)	ζ_1^\perp	ζ_1^\parallel	$\zeta_1^\perp/\zeta_1^\parallel$	ζ_2^\perp	ζ_2^\parallel	$\zeta_2^\perp/\zeta_2^\parallel$	ζ_3^\perp	ζ_3^\parallel	$\zeta_3^\perp/\zeta_3^\parallel$
Sph	0	0.54	0.59	2.14	1.09	1.18	4.14	1.63	1.77	6.83
Sph	135	0.67	0.74	1.46	1.29	1.27	2.45	1.65	1.58	3.49
Rib	0	0.61	0.56	2.09	1.22	1.12	3.98	1.82	1.68	6.45
Rib	135	0.62	0.62	1.62	1.05	0.99	2.75	1.29	1.20	3.95
Fil	0	0.62	0.57	2.04	1.24	1.15	3.83	1.85	1.72	6.13
Fil	135	0.73	0.75	1.45	1.35	1.27	2.47	1.66	1.52	3.53
Sheet	0	0.61	0.57	2.10	1.22	1.15	4.06	1.82	1.73	6.65
Sheet	135	0.67	0.74	1.51	1.19	1.18	2.59	1.48	1.43	3.67

$$\delta v^\parallel = \left| \frac{(\mathbf{v}(\mathbf{r} + \mathbf{l}) - \mathbf{v}(\mathbf{r})) \cdot \mathbf{l}}{|\mathbf{l}|} \right| \quad (3.23)$$

$$S_p(l) \equiv \sum_i \left[\left(\frac{\sum_j \left(\frac{(\delta v)^p}{\rho_j} \right)}{\sum_j (1/\rho_j)} \right) / \rho_i \right] / \sum_i (1/\rho_i) \quad (3.24)$$

We calculated three orders of the structure functions ($p = 1, 2$ and 3) for the transverse and longitudinal velocity components. The results for each simulation are shown in the figures 3.13 to 3.16. All the functions are very straight, so we could fit them to find the scaling exponent. We chose to fit a region of the function which is statistically best represented $l = 1/32$ to $1/4 L_{init}$, where L_{init} is the initial size of the simulation. The results for the initial and final stage of each case are shown in table 3.1.

The second order velocity structure functions are of special interest since they are the Fourier transform of the velocity power spectrum. We

therefore expect $\beta = \zeta_2 + 1$. Considering both ζ_2^\perp and ζ_2^\parallel , we found $\beta = 1.99 - 2.35$, which is in good agreement with observed values and also consistent with Burgers turbulence.

The transverse and longitudinal structure functions are all very close to parallel. The ratios $\zeta^\perp/\zeta^\parallel$ clearly decrease with time as expected. The turbulence driver here is the gravitational collapse and it is driving the longitudinal component. However the transverse component always dominates, fed by the longitudinal counterpart. For the second order, we found $\zeta_2^\perp/\zeta_2^\parallel = 2.45 - 2.75$, which is larger than what was found numerically for isothermal supersonic turbulence by Kritsuk et al. (2007); $\zeta_2^\perp/\zeta_2^\parallel = 1.27$, and also more than what was predicted by Kolmogorov (1941); $\zeta_2^\perp/\zeta_2^\parallel = 4/3$. This is not very surprising since our simulations are not fully established turbulence and in our initial conditions $\zeta_2^\perp/\zeta_2^\parallel$ is large, due to the lack of compressible modes.

The first order exponents $\zeta_1^\perp = 0.62 - 0.73$ and $\zeta_1^\parallel = 0.62 - 0.75$ are also in very good agreement with the observed values 0.4 - 0.8 (Brunt et al., 2003).

3.5 Conclusion

In this chapter we first reviewed the observables of turbulent motions in molecular clouds. We then discussed statistically the anisotropy in the turbulent velocity field generated by including large scale modes, larger than the initial conditions. We found that a ribbon-like collapse was the most likely outcome.

Then we compared the turbulence, generated by the gravitational collapse, to the observed, predicted and simulated driven turbulence properties (power spectrum, density PDF and energy distribution). We show that molec-

ular clouds under gravitational collapse naturally develop and maintain turbulence with properties consistent with the current observational and theoretical picture. It is the first time serious arguments are shown in favor of this driving mechanism, since the suggestion by Elmegreen (1993).

Turbulence is a very complex process to simulate accurately, therefore grid-based simulations often chose to focus on a uniform periodic box that could represent the central region of a molecular cloud. This allows better resolution of the gas, but it neglects the effect of the overall collapse. This inflow of gas can generate (or drive) random local motions, which we found to have every characteristics of the observed turbulent motions.

Gravitationally driven turbulence can naturally explain, for self-gravitating structures, the apparent universality of turbulence in the molecular interstellar medium on multiple scales (0.03 - 50 pc)(Brunt et al., 2003). This feature is hard to explain with other driving mechanism, e.g. stellar feedback.

Gravitational collapse driving the turbulence limits the lifetime of molecular clouds to be of the order of the free-fall time. However some support against collapse is provided by the gravitationally driven turbulence. The extra energy provided by stellar feedback can also provide further support against collapse, and help the cloud potentially reach a turbulent equilibrium. This picture is consistent with a rather rapid collapse formation scenario for molecular clouds (see Elmegreen (2007) and references therein). It is also in agreement with the observations of infalling motions at large radii, 0.1 pc (Tafalla et al., 1998; Williams & Myers, 1999; Wu et al., 2005; Walsh et al., 2006). It is unclear if the level of larger scale collapse we observe in our simulation could be measured observationally.

This is an exciting conclusion that provide a missing piece to the puzzle

of the star formation process. The observed turbulence *is* driven, continuously over orders of magnitudes in scales, by gravity.

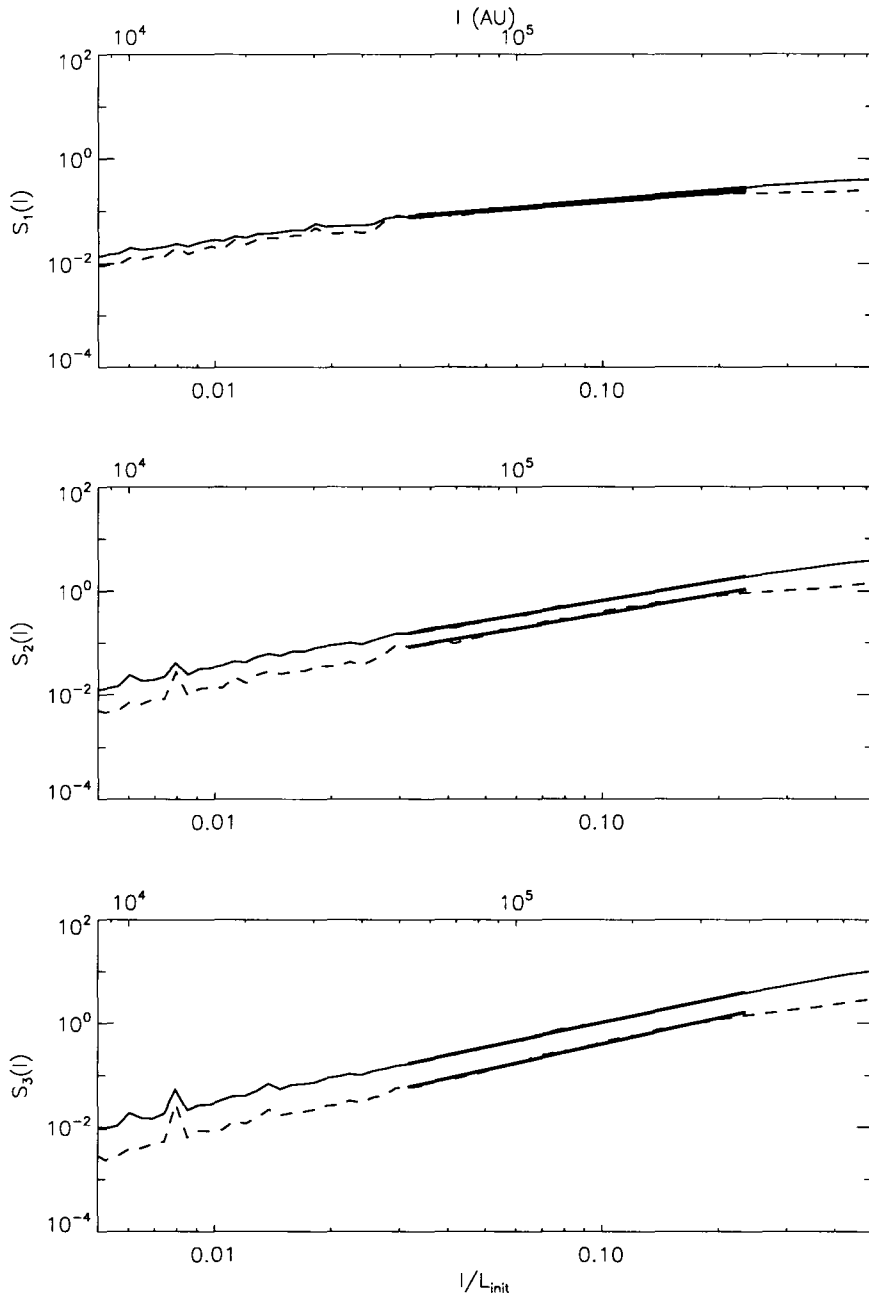


Figure 3.13 Structure functions of the transverse velocities (full line) and the longitudinal velocities (dashed line) for the spherical case. The first (top panel), second (middle panel) and third (bottom panel) order are shown. The bottom axis of each plot is showing the spacing (l) in units of the initial size of the simulation. The best fits to each structure function are over-plotted in grey.

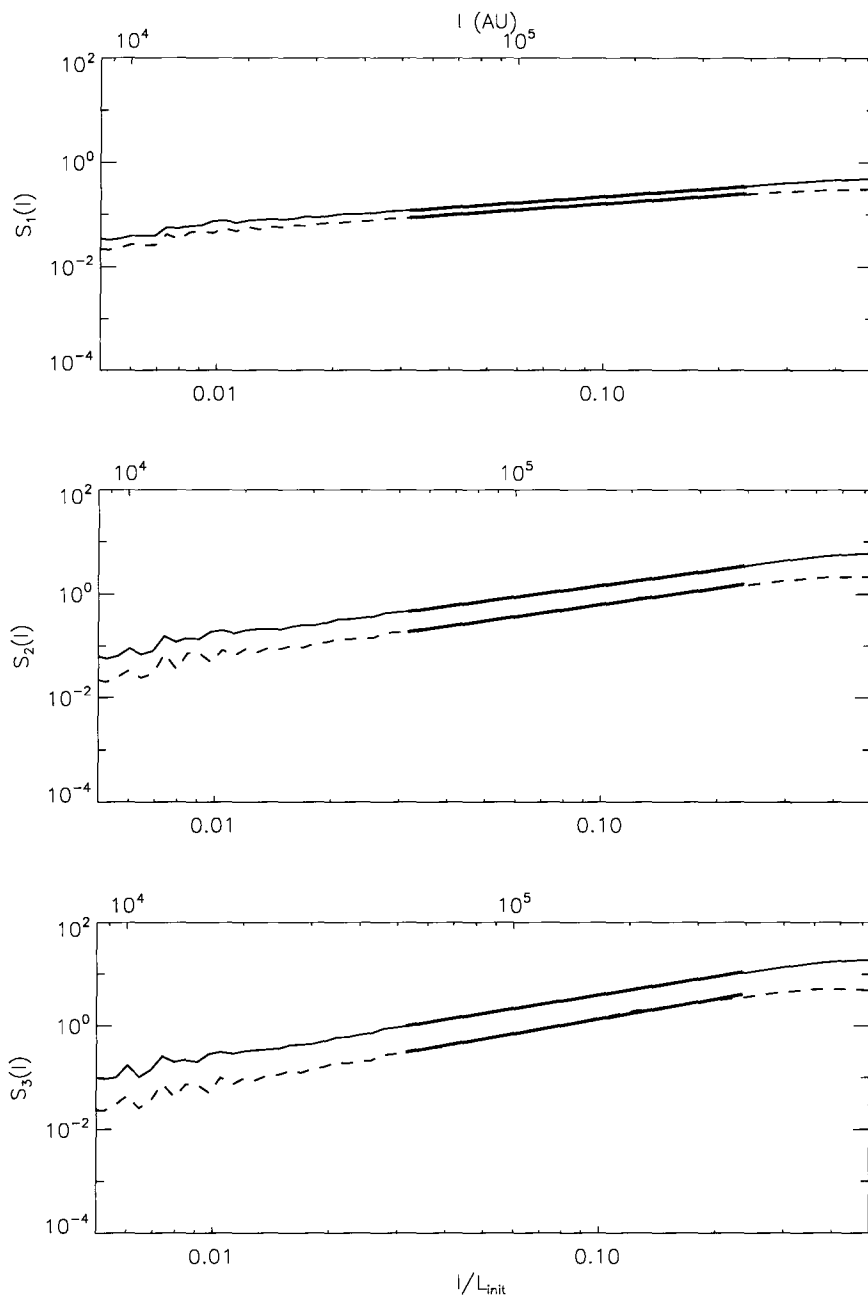


Figure 3.14 Structure functions similar to figure 3.13, but for the ribbon case.

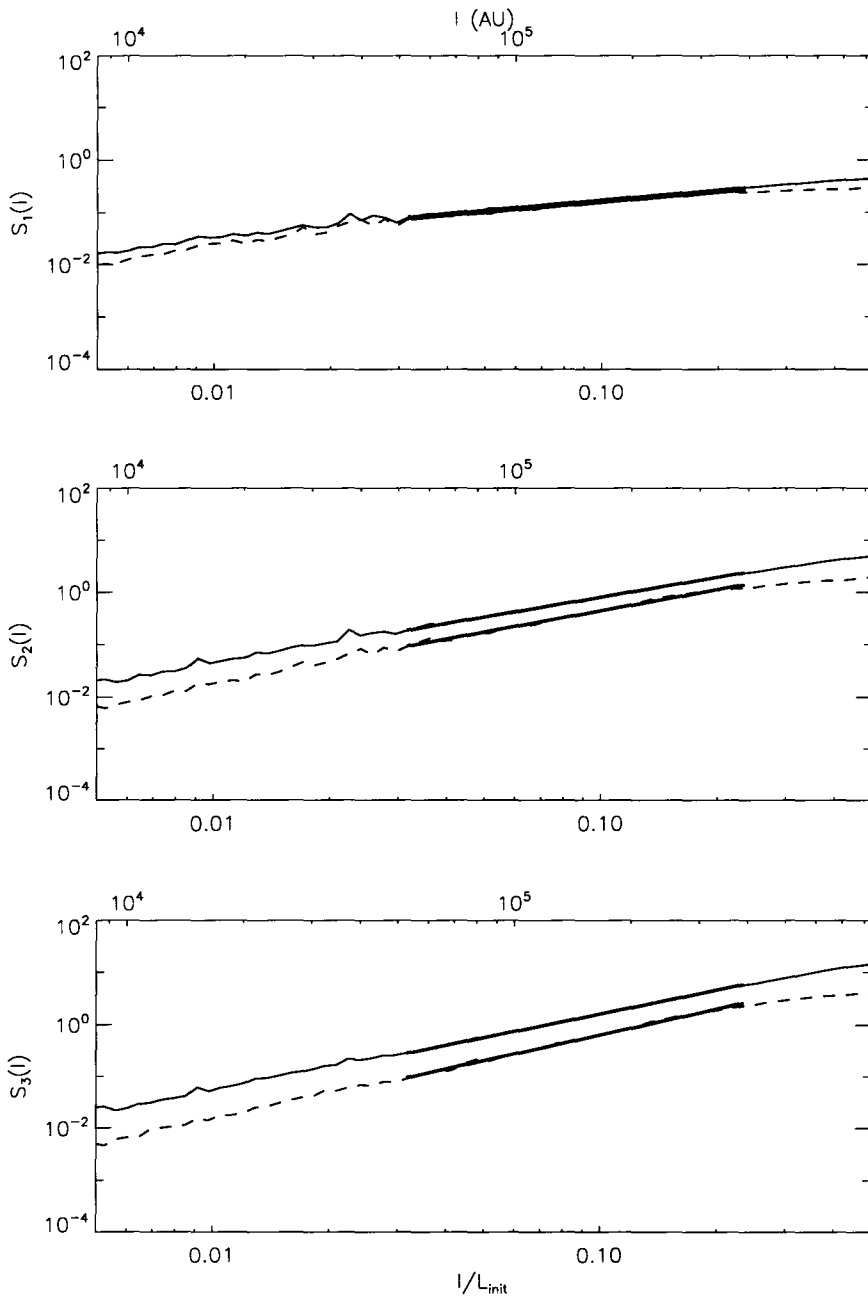


Figure 3.15 Structure functions similar to figure 3.13, but for the filament case.

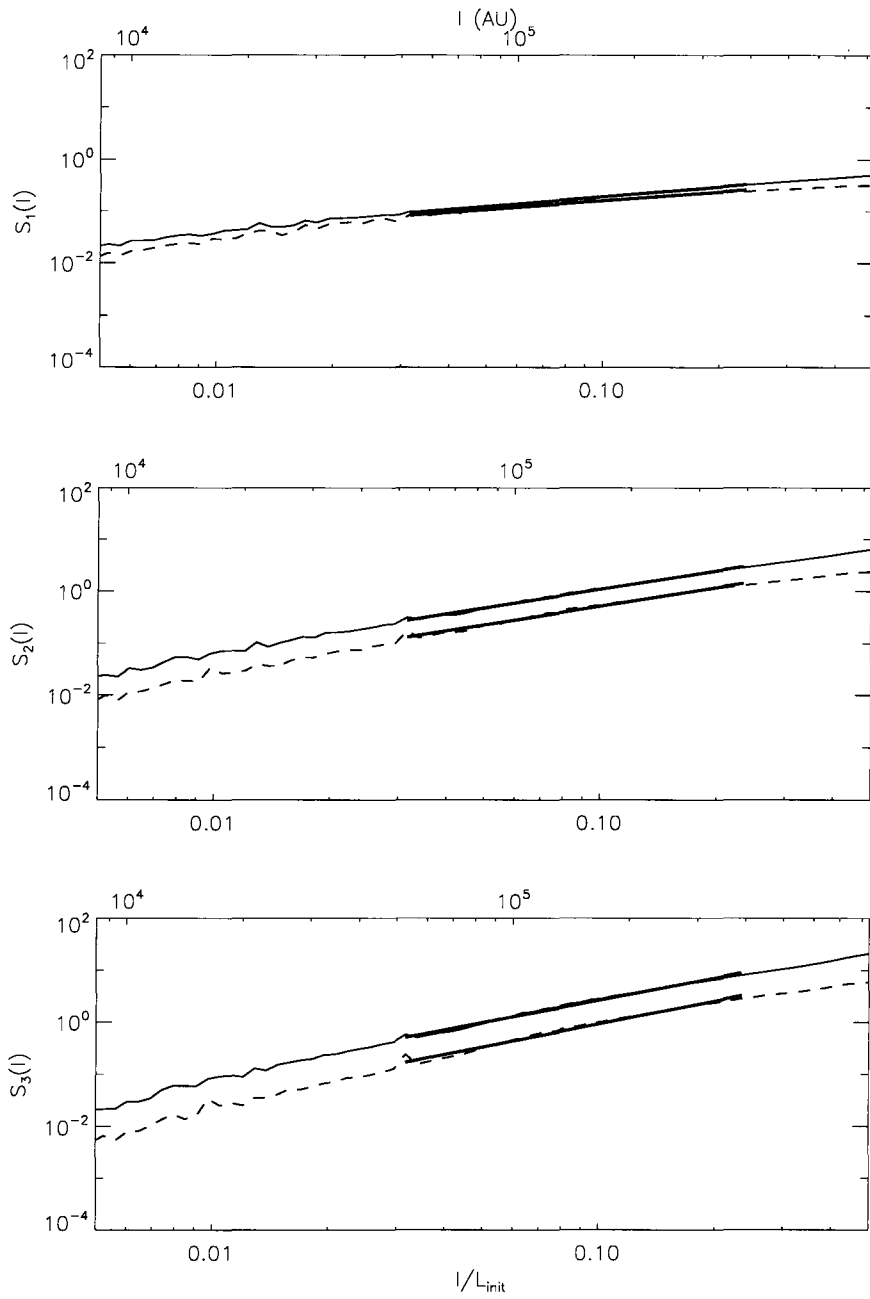


Figure 3.16 Structure functions similar to figure 3.13, but for the sheet case.

Bibliography

- André, P., Basu, S., & Inutsuka, S.-i. 2008, ArXiv e-prints, 801, arXiv:0801.4210
- de Avillez, M. A. 2000, MNRAS, 315, 479
- de Avillez, M. A., & Breitschwerdt, D. 2004, A&A, 425, 899
- de Avillez, M., & Breitschwerdt, D. 2004, Ap&SS, 292, 207
- Ballesteros-Paredes, J., Hartmann, L., & Vázquez-Semadeni, E. 1999, ApJ, 527, 285
- Ballesteros-Paredes, J., Gazol, A., Kim, J., Klessen, R. S., Jappsen, A.-K., & Tejero, E. 2006, ApJ, 637, 384
- Ballesteros-Paredes, J., Klessen, R. S., Mac Low, M.-M., & Vazquez-Semadeni, E. 2007, Protostars and Planets V, 63
- Banerjee, R., Klessen, R. S., & Fendt, C. 2007, ApJ, 668, 1028
- Basu, S., & Murali, C. 2001, ApJ, 551, 743
- Bataille, F. and Zhou, Ye 1999, PhysRev, 59, 5417

- Bate, M. R., Bonnell, I. A., & Price, N. M. 1995, MNRAS, 277, 362
- Bate, M. R., Bonnell, I. A., & Bromm, V. 2002, MNRAS, 332, L65
- Bate, M. R. 2008, arXiv:0811.1035
- Bertoldi, F. 1989, ApJ, 346, 735
- Biskamp, D. 2003, Magnetohydrodynamic Turbulence (Cambridge University Press, Cambridge, UK)
- Blitz, L., & Shu, F. H. 1980, ApJ, 238, 148
- Blitz, L. 1993, Protostars and Planets III, 125
- Boldyrev, S., Nordlund, Å., & Padoan, P. 2002a, ApJ, 573, 678
- Boldyrev, S., Nordlund, Å., & Padoan, P. 2002b, Physical Review Letters, 89, 031102
- Bonnell, I. A., Bate, M. R., & Vine, S. G. 2003, MNRAS, 343, 413
- Bonnell, I. A., Vine, S. G., & Bate, M. R. 2004, MNRAS, 349, 735
- Bonnell, I. A., Dobbs, C. L., Robitaille, T. P., & Pringle, J. E. 2006, MNRAS, 365, 37
- Brunt, C. M., & Heyer, M. H. 2002, ApJ, 566, 276
- Brunt, C. M., Heyer, M. H., Vázquez-Semadeni, E., & Pichardo, B. 2003, ApJ, 595, 824
- Burgers, J. M. 1974, The Nonlinear Diffusion Equation (Boston: D. Reidel)

- Carroll, J. J., Frank, A., Blackman, E. G., Cunningham, A. J., & Quillen, A. C. 2008, arXiv:0805.4645
- Cho, J., & Lazarian, A. 2003, MNRAS, 345, 325
- Elmegreen, B. G. 1993, ApJ, 419, L29
- Elmegreen, B. G. 2000, ApJ, 530, 277
- Elmegreen, B. G., & Scalo, J. 2004, ARA&A, 42, 211
- Elmegreen, B. G., Kimura, T., & Tosa, M. 1995, ApJ, 451, 675
- Elmegreen, B. G. 2007, ApJ, 668, 1064
- Falgarone, E., Puget, J.-L., & Perault, M. 1992, A&A, 257, 715
- Fleck, R. C., Jr. 1981, ApJ, 246, L151
- Gammie, C. F., & Ostriker, E. C. 1996, ApJ, 466, 814
- Gammie, C. F., Lin, Y.-T., Stone, J. M., & Ostriker, E. C. 2003, ApJ, 592, 203
- Goldreich, P., & Kwan, J. 1974, ApJ, 189, 441
- Gritschneider, M., Naab, T., Walch, S., Burkert, A., & Heitsch, F. 2009, arXiv:0901.2113
- Hartmann, L., Ballesteros-Paredes, J., & Bergin, E. A. 2001, ApJ, 562, 852
- Hartmann, L. 2003, ApJ, 585, 398
- Heiles, C., & Katz, G. 1976, AJ, 81, 37

- Heiles, C., & Troland, T. H. 2003, *ApJ*, 586, 1067
- Heyer, M. H., & Brunt, C. M. 2004, *ApJ*, 615, L45
- Heyer, M. H., & Brunt, C. 2007, *IAU Symposium*, 237, 9
- Howes, G. G. 2008, *Physics of Plasmas*, 15, 055904
- Jappsen, A.-K., Klessen, R. S., Larson, R. B., Li, Y., & Mac Low, M.-M. 2005, *A&A*, 435, 611
- Kessel-Deynet, O., & Burkert, A. 2003, *MNRAS*, 338, 545
- Kim, J., Balsara, D., & Mac Low, M.-M. 2001, *Journal of Korean Astronomical Society*, 34, 333
- Kim, C.-G., Kim, W.-T., & Ostriker, E. C. 2006, *ApJ*, 649, L13
- Klessen, R. S., Burkert, A., & Bate, M. R. 1998, *ApJ*, 501, L205
- Klessen, R. S. 2001, *ApJ*, 556, 837
- Kolmogorov, A. 1941, *Akademiia Nauk SSSR Doklady*, 30, 301
- Kritsuk, A. G., Norman, M. L., Padoan, P., & Wagner, R. 2007, *ApJ*, 665, 416
- Krumholz, M. R. 2006, *ArXiv Astrophysics e-prints*, arXiv:astro-ph/0610526
- Krumholz, M. R., Matzner, C. D., & McKee, C. F. 2006, *ApJ*, 653, 361
- Larson, R. B. 1981, *MNRAS*, 194, 809
- Li, P. S., Norman, M. L., Mac Low, M.-M., & Heitsch, F. 2004, *ApJ*, 605, 800

- Li, Z.-Y., & Nakamura, F. 2006, *ApJ*, 640, L187
- Mac Low, M.-M., Klessen, R. S., Burkert, A., & Smith, M. D. 1998, *Physical Review Letters*, 80, 2754
- Mac Low, M.-M. 1999, *ApJ*, 524, 169
- Mac Low, M.-M., & Klessen, R. S. 2004, *Reviews of Modern Physics*, 76, 125
- Mac Low, M.-M., Balsara, D. S., Kim, J., & de Avillez, M. A. 2005, *ApJ*, 626, 864
- Matzner, C. D. 2007, *ApJ*, 659, 1394
- McKee, C. F., & Ostriker, E. C. 2007, *ARA&A*, 45, 565
- Merrifield, J. A., Müller, W.-C., Chapman, S. C., & Dendy, R. O. 2005, *Physics of Plasmas*, 12, 022301
- Mizuno, N., et al. 2001, *PASJ*, 53, 971
- Monin, A. S., & Yaglom, A. M. 1975, *Statistical Fluid Mechanics: Mechanics of Turbulence*, Vol. 2 (Cambridge: MIT Press)
- Motte, F., Andre, P., & Neri, R. 1998, *A&A*, 336, 150
- Nakamura, F., & Li, Z.-Y. 2007, *ApJ*, 662, 395
- Nordlund, Å. K., & Padoan, P. 1999, *Interstellar Turbulence*, 218
- Nordlund, Å., & Padoan, P. 2003, *Turbulence and Magnetic Fields in Astrophysics*, 614, 271
- Norman, C. A., & Ferrara, A. 1996, *ApJ*, 467, 280

- Offner, S. S. R., Krumholz, M. R., Klein, R. I., & McKee, C. F. 2008, *AJ*, 136, 404
- Offner, S. S. R., Klein, R. I., & McKee, C. F. 2008, *ApJ*, 686, 1174
- Padoan, P., Nordlund, A., & Jones, B. J. T. 1997, *MNRAS*, 288, 145
- Padoan, P., & Nordlund, Å. 1999, *ApJ*, 526, 279
- Padoan, P., & Nordlund, Å. 2002, *ApJ*, 576, 870
- Padoan, P., Nordlund, Å., Kritsuk, A. G., Norman, M. L., & Li, P. S. 2007, *ApJ*, 661, 972
- Pope, S. B., Ching, E. 1993, *Phys. Fluids A*, 5, 7
- Pope, S. B., *Turbulent Flows*, Cambridge University Press, Cambridge, U.K., 2000, 771 pp.
- Porter, D., Pouquet, A., & Woodward, P. 2002, *Phys. Rev. E*, 66, 026301
- Rosen, A., Bregman, J. N., & Norman, M. L. 1993, *ApJ*, 413, 137
- Rosen, A., & Bregman, J. N. 1995, *ApJ*, 440, 634
- Sasao, T. 1973, *PASJ*, 25, 1
- Schmidt, W., Federrath, C., Hupp, M., Kern, S., & Niemeyer, J. C. 2008, [arXiv:0809.1321](https://arxiv.org/abs/0809.1321)
- Sellwood, J. A., & Balbus, S. A. 1999, *ApJ*, 511, 660
- Solomon, P. M., Rivolo, A. R., Barrett, J., & Yahil, A. 1987, *ApJ*, 319, 730

- Stamatellos, D., Whitworth, A. P., Bisbas, T., & Goodwin, S. 2007, *A&A*, 475, 37
- Stone, J. M., Ostriker, E. C., & Gammie, C. F. 1998, *ApJ*, 508, L99
- Tafalla, M., Mardones, D., Myers, P. C., Caselli, P., Bachiller, R., & Benson, P. J. 1998, *ApJ*, 504, 900
- Tilley, D. A., & Pudritz, R. E. 2004, *MNRAS*, 353, 769
- Truelove, J. K., Klein, R. I., McKee, C. F., Holliman, J. H., II, Howell, L. H., & Greenough, J. A. 1997, *ApJ*, 489, L179
- Vazquez-Semadeni, E. 1994, *ApJ*, 423, 681
- Vazquez-Semadeni, E., Passot, T., & Pouquet, A. 1996, *ApJ*, 473, 881
- Vázquez-Semadeni, E., Gómez, G. C., Jappsen, A. K., Ballesteros-Paredes, J., González, R. F., & Klessen, R. S. 2007, *ApJ*, 657, 870
- Wada, K., & Norman, C. A. 2001, *ApJ*, 547, 172
- Wadsley, J. W., Stadel, J., & Quinn, T. 2004, *New Astronomy*, 9, 137
- Walsh, A. J., Bourke, T. L., & Myers, P. C. 2006, *ApJ*, 637, 860
- Williams, J. P., & Myers, P. C. 1999, *ApJ*, 511, 208
- Wu, Y., Zhu, M., Wei, Y., Xu, D., Zhang, Q., & Fiege, J. D. 2005, *ApJ*, 628, L57
- Zuckerman, B., & Evans, N. J., II 1974, *ApJ*, 192, L149

Chapter 4

Proto-stellar cores

4.1 Introduction

The aim of this chapter is to do direct comparison of our simulations with observations. These simulations are currently the only SPH simulations of dense core formation not using sink particles. Our simulations are resolved down to approximately 100 AU, whereas high resolution observations can have resolution around 1000 AU. This makes them ideal for detailed comparison with observations.

The most relevant observations to compare our simulations to are young molecular clouds with a relatively low mass compared to giant molecular complexes, as our simulations have properties of molecular clouds, with $5\,000 M_{\odot}$ and $n_{init} = 300 \text{ cm}^{-3}$. They should be compared to regions where the feedback (outflow) from the forming stars (especially massive ones) have little effects, since our simulations do not include feedback from the proto-stellar cores.

We produced column density, mean velocity and velocity dispersion maps of our dense cores similar to the one studied by observations of molecular lines emission (e.g. Goodman et al. (1993); Di Francesco et al. (2001); Caselli et al. (2002); Tafalla et al. (2004); Kirk et al. (2007); Chen et al. (2007)). This work enables us to discuss key questions, like what role turbulence, rotation or infall play in the observed velocity dispersion or whether the cores are bounded or not. But more importantly it allow us to identify which observed features (density profiles, velocity dispersion and rotation of the cores, core-core velocity dispersion, core-envelope velocity dispersion, velocity dispersion vs. core size relation and the core mass function) can be reproduced with isothermal hydrodynamics simulations, without adding any extra physics like magnetic fields, outflows, proper equation of state or radiative transfer. We found our simulation to be in good general agreement with observations, but some discrepancies are discussed. We also discuss some observational methods by comparing our conclusions from our simulated observations to our real 3D simulation.

4.2 Simulated observations

To compare our simulations with observation more directly, we produced 2D maps of the column density (N_z), mean velocity ($\langle v_z \rangle$) and velocity dispersion (σ_z) along line of sight (z). The lines of sight are distributed on a uniform grid over a region of interest. To calculate these properties along the lines of sight, we weighted the contribution of each particle, closer than ($\leq 2h$) to a given line of sight, by their SPH smoothing kernel. We made sure no particles were contributing more or less than their total mass when intersecting more

than one line of sight. And for the particles in dense regions, with small h , intersecting no line of sight, we added their contributions to the closest one. The properties calculated are:

$$N = \int \rho dz \quad (4.1)$$

$$\langle v_z \rangle = \frac{\int \rho v_z dz}{\int \rho dz} \quad (4.2)$$

$$\sigma_z^2 = \frac{\int \rho (v_z - \langle v_z \rangle)^2 dz}{\int \rho dz} \quad (4.3)$$

$$\begin{aligned} &= \int \rho v_z^2 dz - 2 \int \rho v_z \langle v_z \rangle dz \\ &\quad + \int \rho \langle v_z \rangle^2 dz \\ &= \frac{\int \rho v_z^2 dz}{\int \rho dz} - \langle v_z \rangle^2 \end{aligned} \quad (4.4)$$

where the integrals are over the line of sight (z). The quantities we can directly calculate are: $\int \rho dz$, $\int \rho v_z dz$ and $\int \rho v_z^2 dz$. This way we don't have to calculate $\langle v_z \rangle$ before doing a second integration for σ_z^2 .

We also choose 3 density ranges to simulate observations with different molecular tracers. The lower density range is $\rho_{C^{18}O}$ for $4.7 \times 10^3 < n < 5 \times 10^4 \text{ cm}^{-3}$, which was chosen to mimic observations of the $C^{18}O$ ($J = 2-1$) transition molecular lines. Depletion of these molecules by freeze out onto grains was observed to occur near this maximal density (Tafalla et al., 2004). These molecules are therefore considered to be tracing the lower density envelope of the cores.

The other density ranges are chosen to simulate observations of the N_2H^+ ($J = 1-0$) and the NH_3 (1,1) transitions. The source of these molecules is molecular nitrogen (N_2), which is very volatile and can remain in gaseous state to high density with the cosmic rays heating the surfaces of grains (Tafalla et al., 2004). These molecules are therefore thought to remain present to very high density $n > 1 \times 10^6 \text{ cm}^{-3}$ (Walmsley et al., 2004). However, the depletion of these molecules has never been observed, we therefore used the very high limit ($5 \times 10^7 \text{ cm}^{-3}$ (Tafalla et al., 2004), containing almost all the densest gas of our simulations. The lower density threshold of every density range are the critical excitation density taken from the Leiden Atomic and Molecular Database ¹ (Schöier et al., 2005). The $\rho_{N_2H^+}$ density range is therefore $6.2 \times 10^4 < n < 5 \times 10^7 \text{ cm}^{-3}$ and the ρ_{NH_3} range is $1.9 \times 10^3 < n < 5 \times 10^7 \text{ cm}^{-3}$.

In Figures 4.1 to 4.4 we show the column density maps for each simulation at the ρ_{NH_3} density range. They show the inner 3.4 pc of the simulated molecular clouds. To simulate a beam size of 1000 AU, we convolved these maps with a Gaussian of FWHM = 1000 AU.

In a first attempt to identify cores, we used the program Clumpfind2D (Williams et al., 1994). Clumpfind2D automatically identify cores from a 2D flux (or column density in our case) map, from a set of user defined contour levels. The peaks are identified on each contour levels. If a peak is identified in more than one contour, they are merged and only one core is created. Observers must use contour levels that differ by at least their noise level in order to avoid false detections. Considering the fact that our images contain very little noise, unlike real observations, we can use many column density contours without the risk of finding “false” cores. We chose 8 contours equally

¹<http://www.strw.leidenuniv.nl/moldata>

spaced in the upper half range of the logarithmic column density map that matched the cores well. The cores found this way are indicated on Figures 4.1 to 4.4 by crosses.

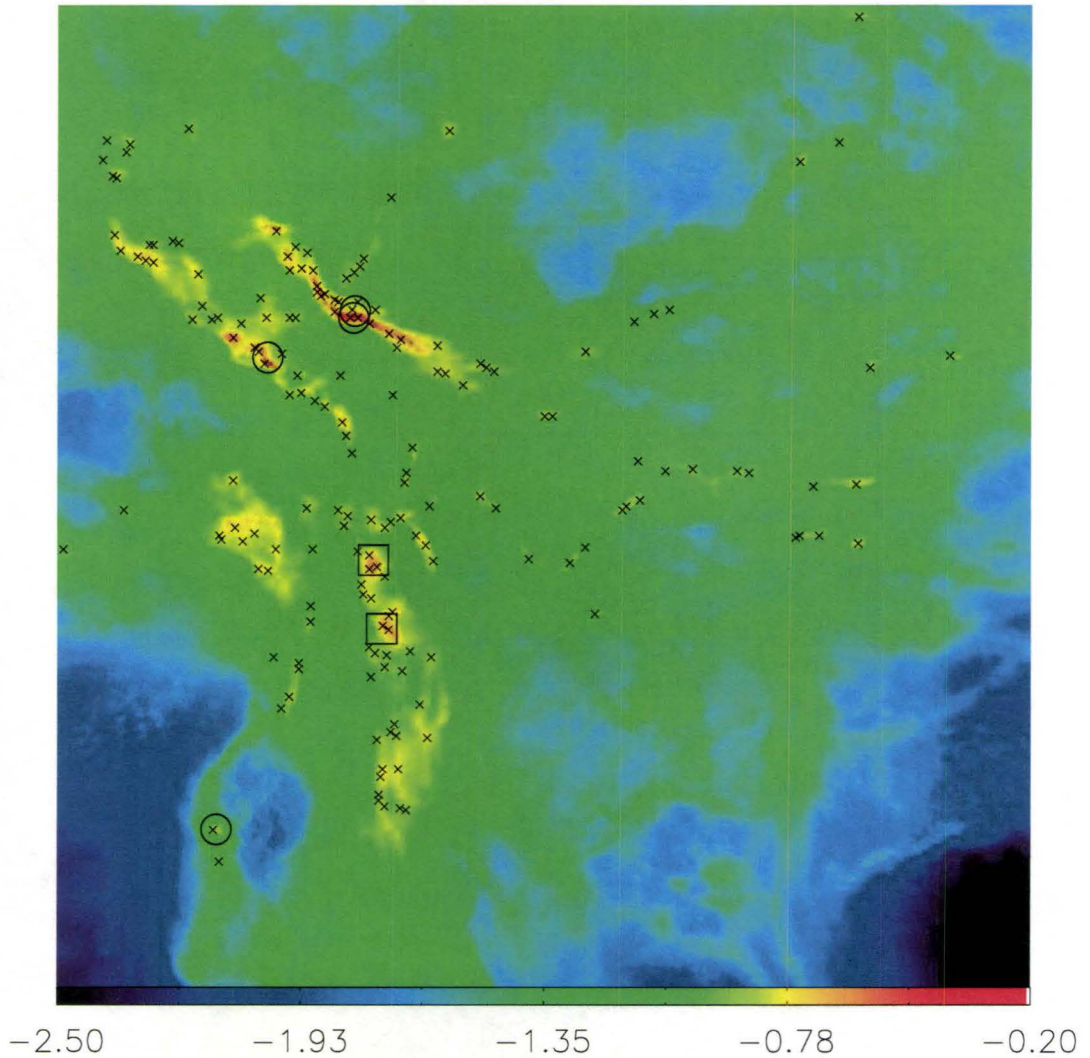


Figure 4.1 Column density maps (500×500 lines of sight) of the spherical case (inner 3.4 pc) seen through the z axis at the final stage (135 kyr). The logarithmic color scale is shown at the bottom, in units of g/cm^2 . The crosses represent all the cores identified by Clumpfind2D and the open circles are cores we looked at in details. The open squares are showing “fake” cores; identified as cores by Clumpfind2D and looked like real cores from the column density map, but they were not when looked in detail in the 3D density distribution.

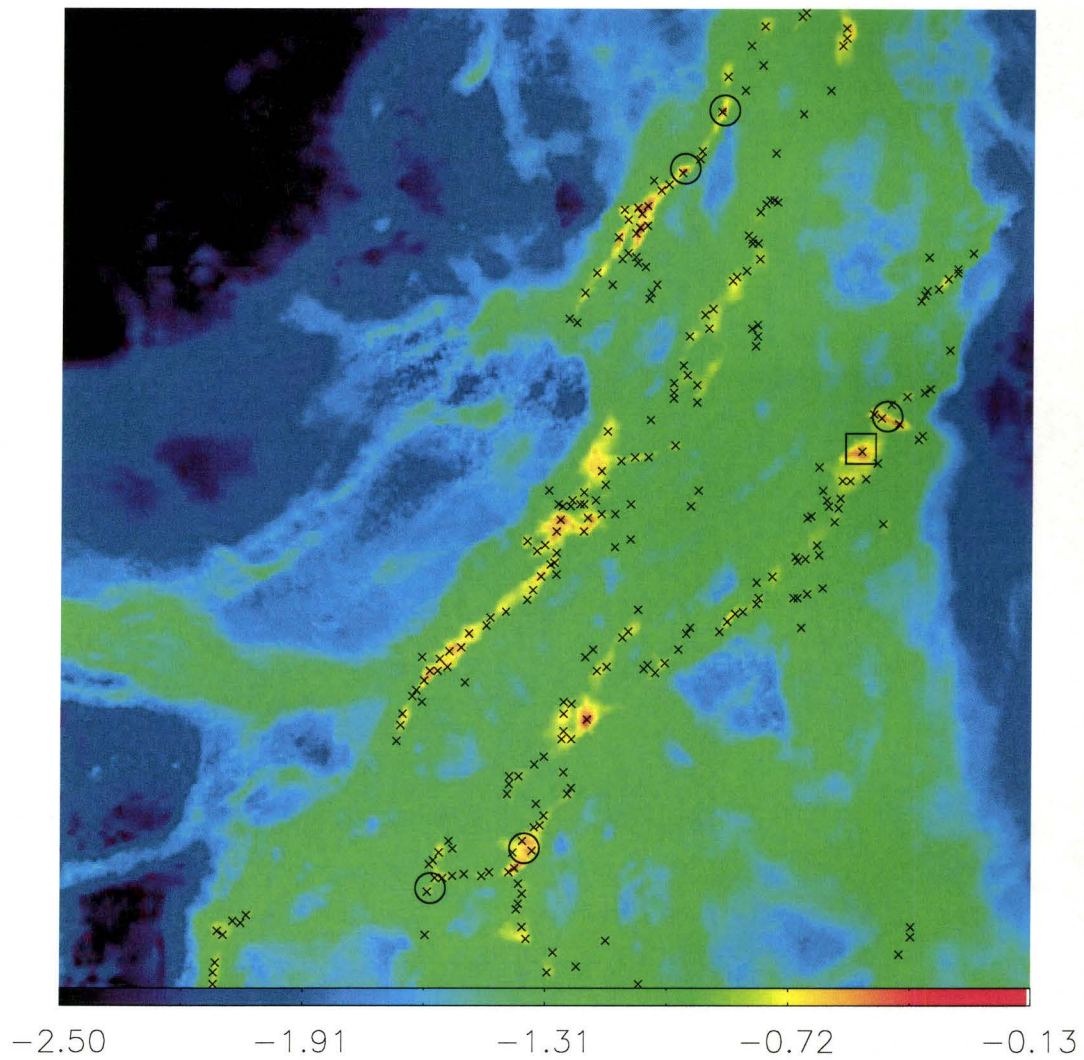


Figure 4.2 Column density maps of the filamentary case seen through the y axis similar to Figure 4.1.

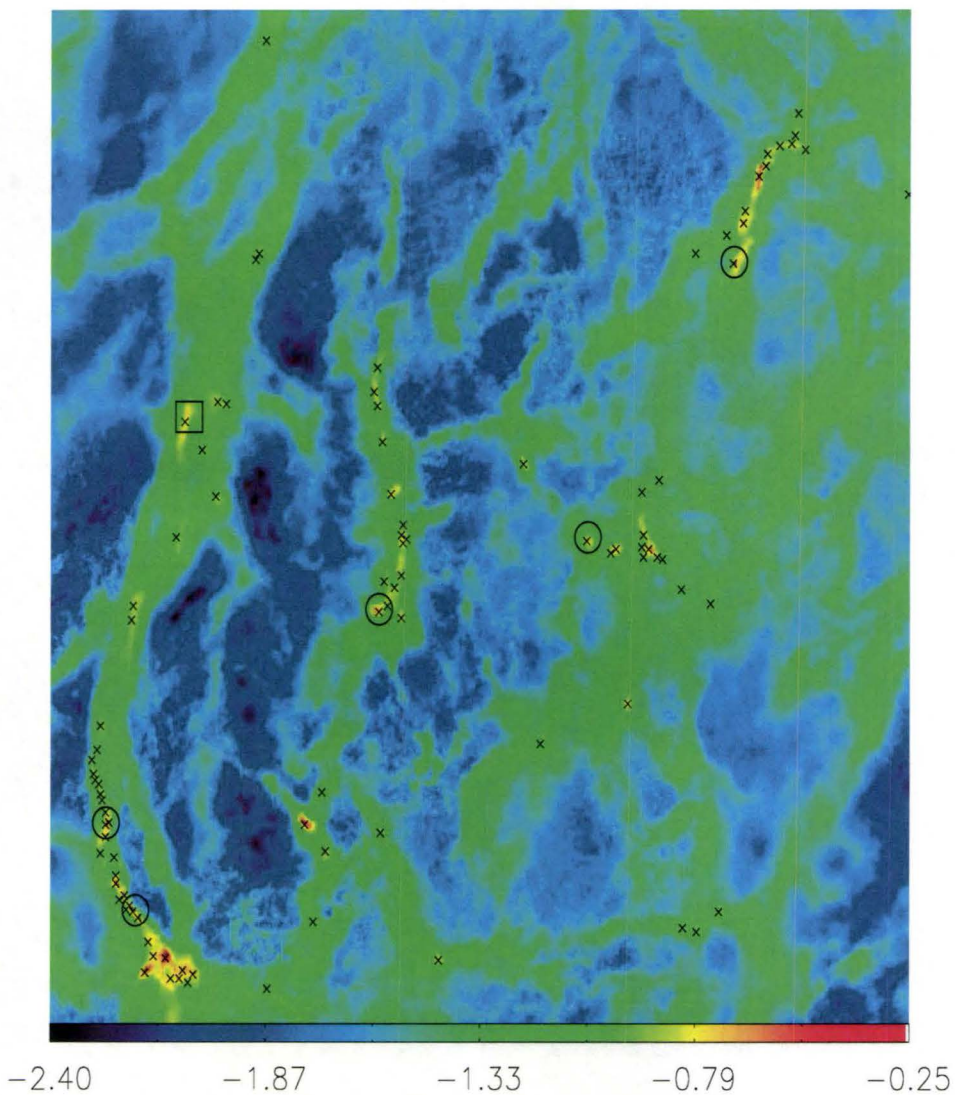


Figure 4.3 Column density maps of the ribbon case seen through the y axis similar to Figure 4.1.

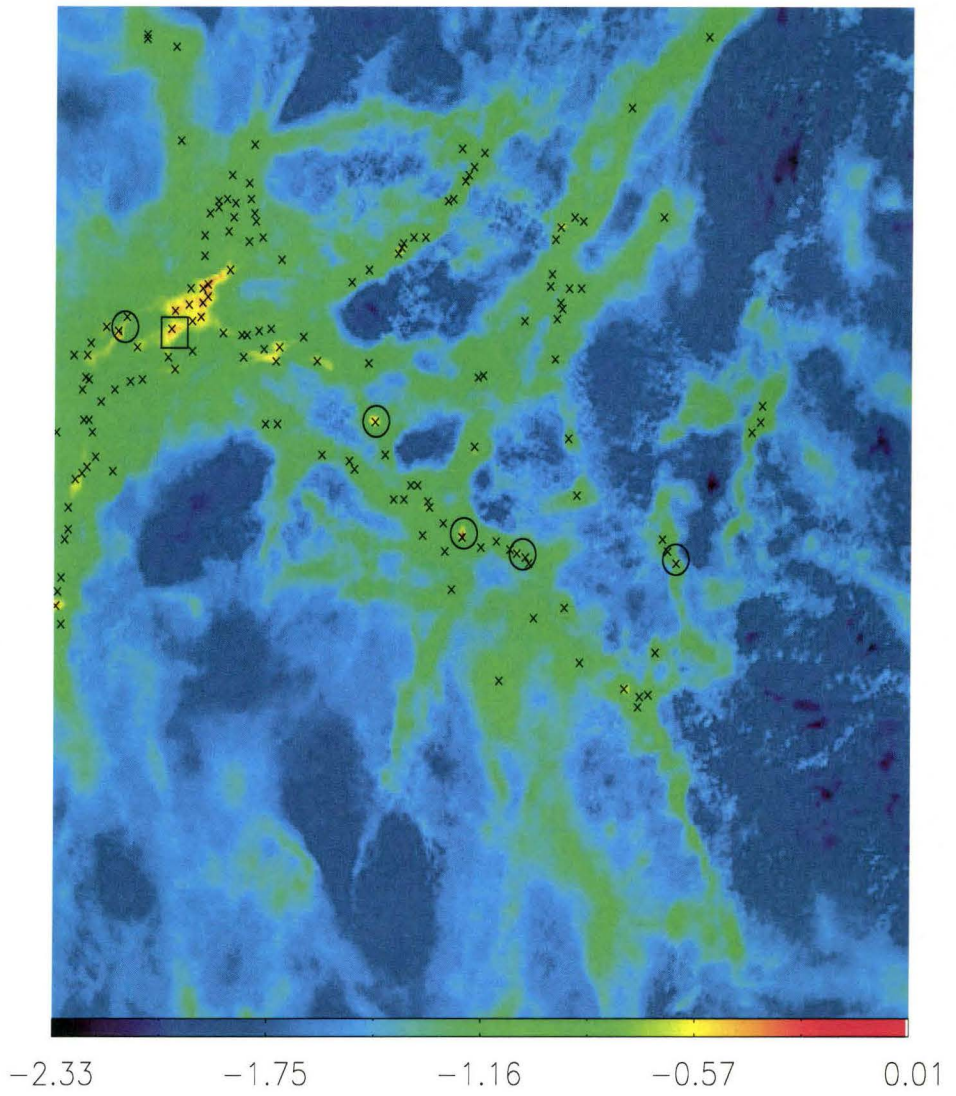


Figure 4.4 Column density maps of the sheet case seen through the y axis similar to Figure 4.1.

4.3 Core formation

From observing the details of the 3D dynamics of the gas around the cores in our simulations, we can infer a general core formation mechanism. We can observe 3 evolution stages of the cores that we named: *compact regions*, *centrally concentrated objects* and *nucleus*. The formation process starts with the collision of gas flows creating a shock. The velocities of the gas flows is reduced dramatically as they shock (Padoan et al., 2001) (see Section 4.7.2) and the gas starts to agglomerate. This form a filamentary or sheet-like over-dense structure. Within this structure, the gas velocity dispersion becomes close to sonic, therefore the gravitational fragmentation can start to operate. What we defined as *compact regions* (CR) can then emerge (see table 4.1) with average diameter $\bar{D} \approx 17400$ AU, average mass of $\approx 3.28M_{\odot}$ and an average density $\bar{n} \approx 1.27 \times 10^5$ cm $^{-3}$. These large but irregular objects stand out from the background density. If the compact objects are bounded they may, under self-gravity, create *centrally concentrated objects* (CC) ($\bar{D} \approx 4767$ AU, $M \approx 0.35M_{\odot}$ and $\bar{n} \approx 9.25 \times 10^5$ cm $^{-3}$, see table 4.2). These smaller objects are differentiable from CR by their denser center and density decrease towards the edges, making them centrally concentrated. There is no significant infall motion at this stage, but the centrally concentrated objects can accrete some more gas and undergo gravitational collapse. This process then forms very dense objects ($\bar{D} \approx 136$ AU, $M \approx 0.90M_{\odot}$ and $\bar{n} \approx 6.95 \times 10^{10}$ cm $^{-3}$, see table 4.3). The central part of these objects are unresolved in our simulations, we define them as *nucleus* (N). They cannot collapse further because of the gravitational softening we used (50 AU). The inner region therefore form a dense ball of gas with radius ≈ 50 AU easily identifiable. At this stage we notice a

strong infall of the surrounding dense gas along the shock generated, surrounding filamentary structures. This dense gas then gains momentum towards the nucleus. This rapid infall motion along the filaments is usually accompanied by some rotation. Before this final stage however, no significant rotation is observed. This way of accumulating mass on the dense core does not generate large momentum built-up. The gas loses its momentum in the initial shock creating the initial filament structure and then the gas infalling along filament will shock again on the dense core. This can significantly reduce the gas momentum compared to gas accreting uniformly without forming shocks.

These three evolution stages are very similar to the three observed evolution stages: starless, prestellar and “Class 0” protostellar cores. However, the classifications are based on different observables. In Sections 4.5 we look at the simulated observations of a few typical examples for each core type. This will enable us to discuss the relation between the two in more details.

4.4 Core sample selection

In our simulations, turbulence generates a large number of density fluctuations. Many of the over-densities observed are not gravitationally bound and transient. Given the fairly early stage in the turbulent fragmentation process of our simulations, only few objects reach a very high density contrast (CC or N) and are very likely to be the site of stellar formation. However, the CR cores are the result of a local shock and are likely to be disrupted. Given their large numbers it seems premature to do a deep investigation for every single one of them, but it is instructive to look at few of them to learn about their general characteristics. We therefore chose to take a sample of cores representative of

the variety of cores (CR, CC and N) found in our simulations.

We identified 6 cores per simulation to look at them in details. We found these cores by visual inspection of the column density maps and of the 3D density distribution, using the visualisation program *Tipsy*. Most cores, but not all, could be identified in both ways. The best way to identify cores was from the 3D density distribution, but we didn't apply a systematic density threshold of interest. This way we would have only identified the densest objects, generally clustered in filamentary structures. We choose cores that were most representative of the spacial distribution, some in the dense filaments and some more isolated. We also chose cores at different density levels.

We looked at all the cores with nucleus (7), and at about half the cores with centrally concentrated objects (6), however there is many more compact regions than the ones we looked at (6), in each simulation. We also identified 5 objects as "*fake*". These objects really looked like dense cores from the column density map. But when we looked at the 3D density distribution, we didn't find a single dense object. We found filaments of low density gas aligned on the line of sight, which looked like a dense core from the column density map. We chose to look at a few of those objects that might be considered as cores by observations.

Our sample of real cores therefore includes 6 or 7 cores of each type, it can be used to compare and define the different characteristics of each type. And by also comparing them with observations, this will ultimately allow us to say if they can be compared to the observed classification of cores.

Table 4.1. Properties of the compact regions, \bar{D} is the average diameter of the object, M is the total mass and $\bar{\rho}$ is the average density.

Object	\bar{D} (AU)	M (M_{\odot})	$\bar{\rho}$ (cm^{-3})
Sph 2	15000	1.86	8.80×10^4
Rib 3	20000	3.70	7.70×10^4
Fil 4	18300	3.23	1.10×10^5
Fil 5	27800	8.40	6.40×10^4
Sheet 4	10000	0.70	1.50×10^5
Sheet 5	13300	1.80	2.75×10^5
Mean	17400	3.28	1.27×10^5
Sigma	5672	3.28	0.72×10^5

Table 4.2. Properties of the centrally concentrated objects, \bar{D} is the average diameter of the object, M is the total mass and $\bar{\rho}$ is the average density.

Object	\bar{D} (AU)	M (M_{\odot})	$\bar{\rho}$ (cm^{-3})
Sph 3	4700	0.29	6.00×10^5
Sph 4	6700	0.42	2.50×10^5
Rib 4	3500	0.13	4.77×10^5
Rib 5	8000	0.68	2.22×10^5
Fil 3	3100	0.32	1.60×10^6
Sheet 3	2600	0.28	2.40×10^6
Mean	4767	0.35	9.25×10^5
Sigma	1969	0.17	8.05×10^5

Table 4.3. Properties of the nucleus, \bar{D} is the average diameter of the object, M is the total mass and $\bar{\rho}$ is the average density.

Object	\bar{D} (AU)	M (M_{\odot})	$\bar{\rho}$ (cm^{-3})
Sph 1	110	1.27	1.57×10^{11}
Rib 1	112	0.38	4.27×10^{10}
Rib 2	124	1.42	2.38×10^{11}
Fil 1	175	1.60	5.67×10^{10}
Fil 2	120	0.92	1.00×10^{11}
Sheet 1a	200	1.24	3.00×10^9
Sheet 1b	100	0.74	7.00×10^9
Sheet 2a	160	0.39	4.20×10^9
Sheet 2b	120	0.12	1.70×10^{10}
Mean	136	0.90	6.95×10^{10}
Sigma	32	0.49	7.69×10^{10}

4.5 Cores map

We produced 2D maps of the column density, mean velocity and velocity dispersion for the 24 cores, in the x, y and z directions at the 3 density ranges. We also investigated the effects, on those maps, of all the gas on the line of sight not belonging to the core itself. To do so, we made maps with the line of sight going through the whole cloud (named as *all*) and another one going through only the core itself. We will show some examples, but the whole set of images can be consulted on the web ².

Figure 4.5 shows the maps of the core Fil5z and Figure 4.6 is for the same core, but the integrations are done through the whole cloud, they demonstrate the effect of the gas on the line of sight. We found that the gas on the

²<http://www.physics.mcmaster.ca/~petitchn/Thesis/combinedCoreImages.pdf>

line of sight had significant effects on the maps for every density ranges. In the $\rho_{N_2H^+}$ and ρ_{NH_3} column density maps, the shape of the cores is generally unaffected, except the core is slightly larger when seen through the whole line of sight. The main difference however is the overall column density which is increased, by a factor ~ 2 . The consequences of this effect are investigated further in Section 4.11.2. The column density maps in the $\rho_{C_{18}O}$ density range is however seriously affected, because the probability of having low density gas along the line of sight is higher.

The contamination of the gas along the line of sight also affects the mean velocity and velocity dispersion maps for every density ranges. This gas is uncorrelated to the core and therefore its velocity can be very different. The mean velocity maps for the $\rho_{C_{18}O}$ density range on figure 4.5 and 4.6 even show very little correlation. The $\rho_{N_2H^+}$ and ρ_{NH_3} maps however, beside the variations, preserve the main feature of the core, a negative mean velocity. A similar argument applies for the velocity dispersion maps that show, as expected, a larger velocity dispersion when seen through the whole line of sight. For now on, we used the maps going only through the cores, unless specified, to avoid these effects and investigate the real properties of the cores.

The different orientations also lead occasionally to a significant difference in size and structure of the cores. A striking example is from the Rib3 core, which has a filamentary structure oriented almost directly along the z axis. This filamentary structure is shown from the x axis in Figure 4.7 and it looks like a spherical object from the z axis in Figure 4.8. We therefore used, for now on, the measures found in each direction independently, as if they were different cores.

To represent what the maps of the 3 different types of cores looks like

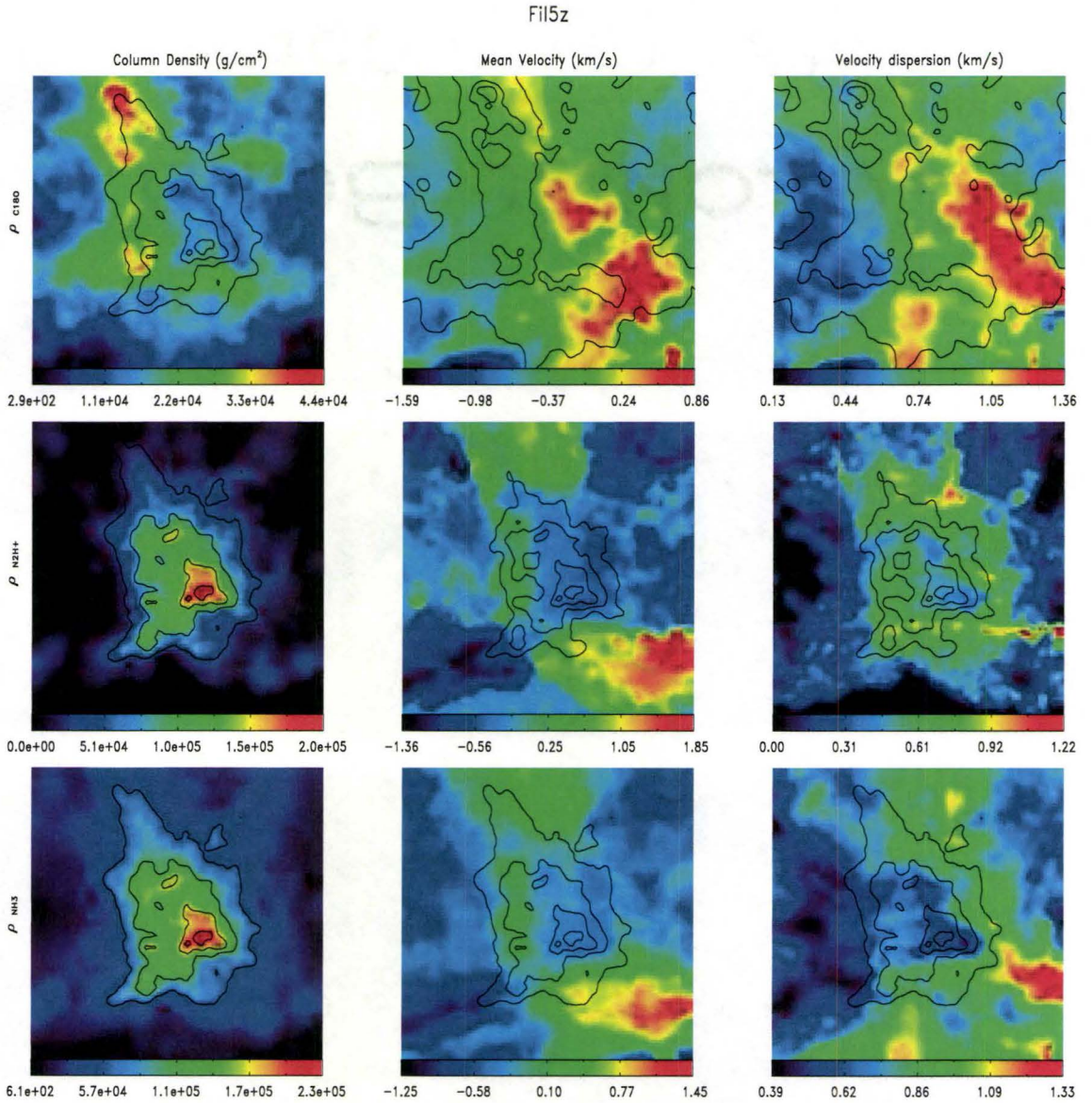


Figure 4.5 2D maps (200×200 lines of sight) for the Fil5 (CR) core seen through the z axis. The size of the images shown is 56000×56000 AU. The left column is showing the column density, the middle one the mean velocity and right one the velocity dispersion. The 3 rows are for 3 density ranges, on top $\rho_{\text{C}18\text{O}}$, in the middle $\rho_{\text{N}2\text{H}^+}$ and at the bottom ρ_{NH_3} . On the left column the contour line shown is for 90, 75, 50 and 25% of the maximum column density of the ρ_{NH_3} map. On the middle and right hand side columns, the contour lines are the same levels but for the maximum column density at their respective density ranges.

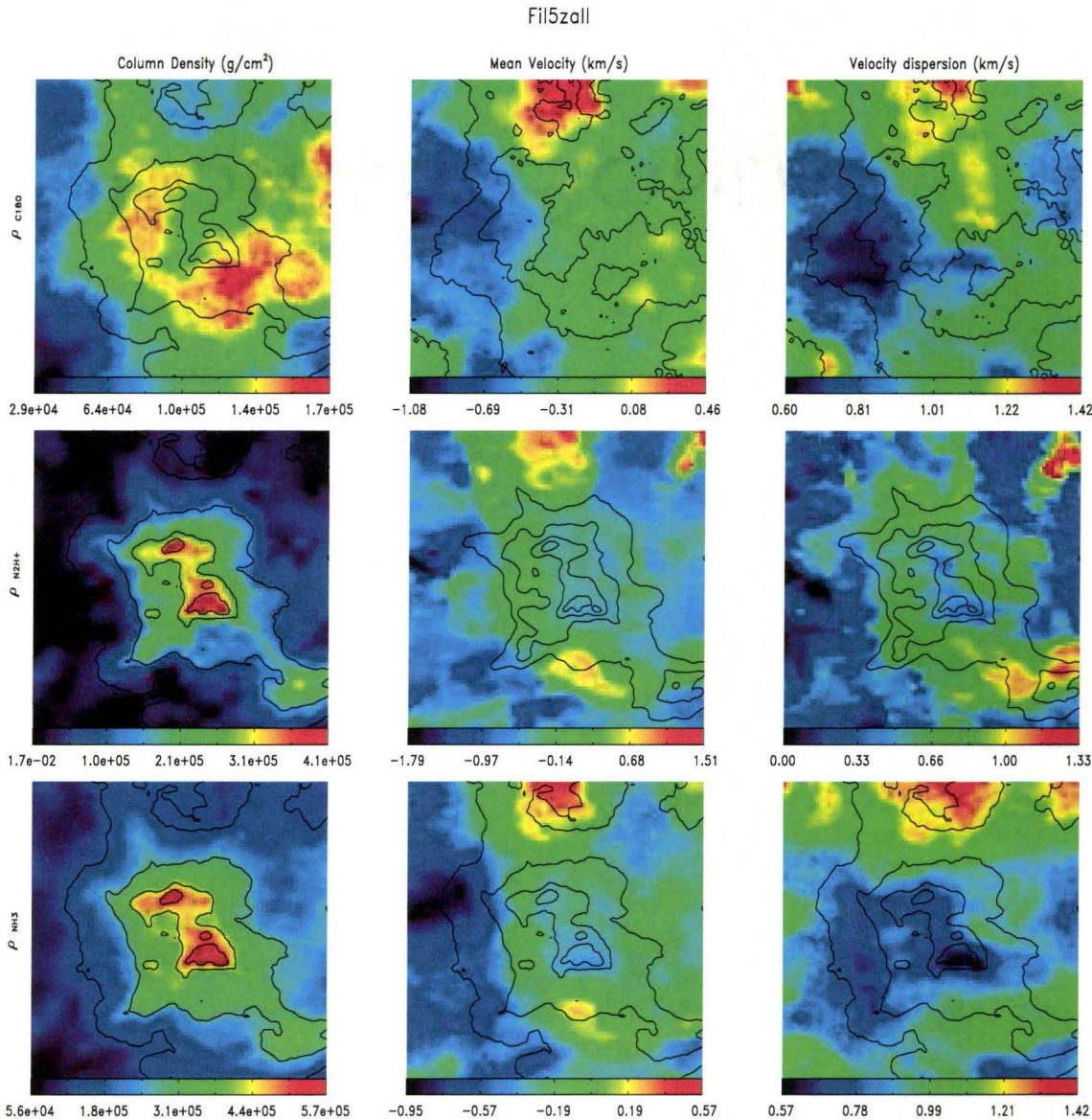


Figure 4.6 Same as Figure 4.5 but this time the lines of sight are going through the whole cloud instead of only the 56000 AU cube box.

we show an example of each (see Figures 4.9, 4.11 and 4.13). These maps are accompanied by radial profiles of the cores (see Figures 4.10, 4.12 and 4.14) describing important features of the typical core cases. They are discussed in more details in Sections 4.6 and 4.7.1. The complete set of radial profiles can

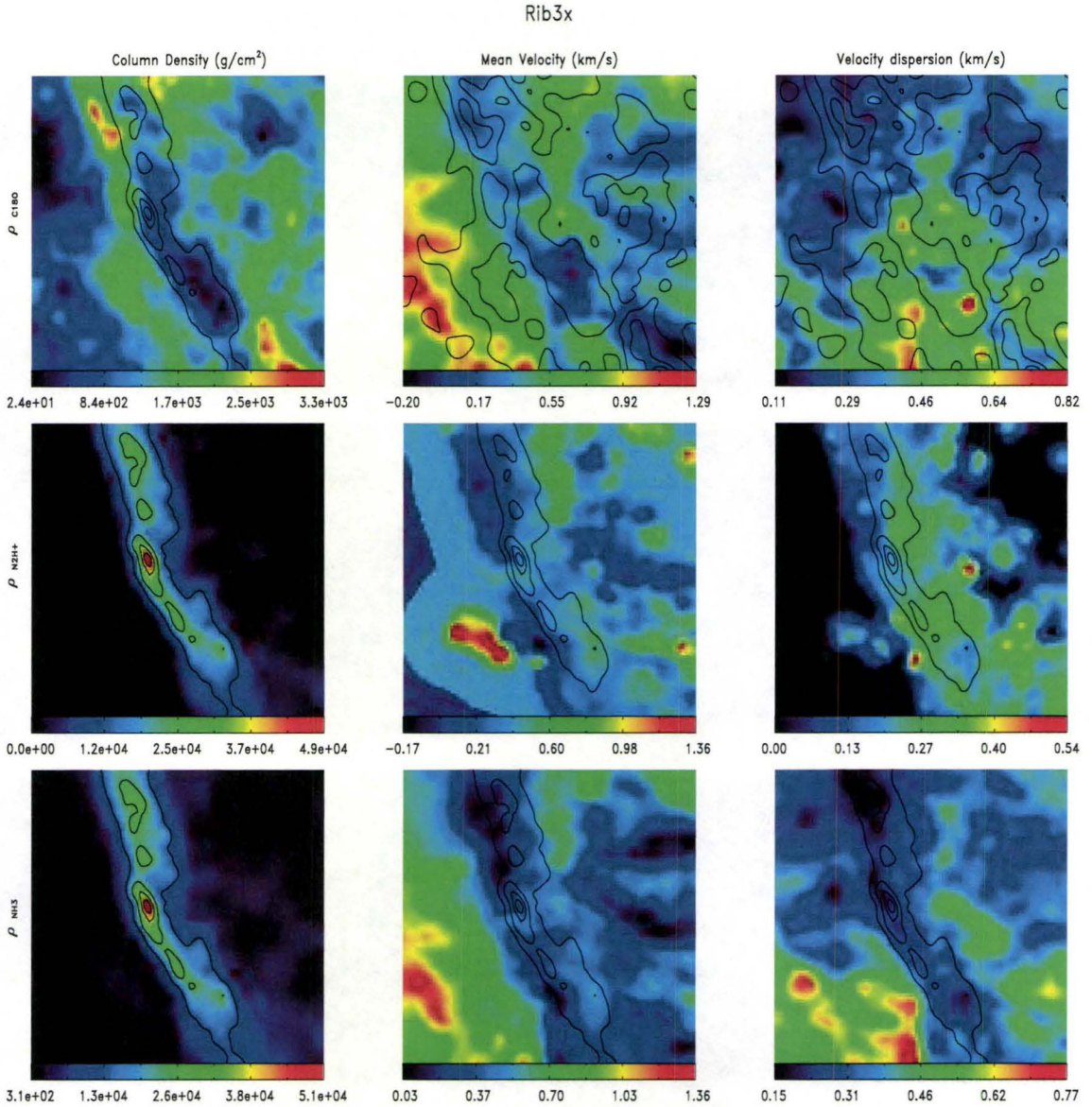


Figure 4.7 Same as Figure 4.5 but for the Rib3 (CR) core seen through the x axis. The image size shown is 34000×34000 AU.

be consulted on the web ³.

The core Fil5 (Figure 4.9) is a good example of a very large irregular and not centrally concentrated structure (CR). The large scale velocity difference on the mean velocity maps is not a sign of rotation but rather of 2

³<http://www.physics.mcmaster.ca/~petitcn/Thesis/combinedRadPlot.pdf>

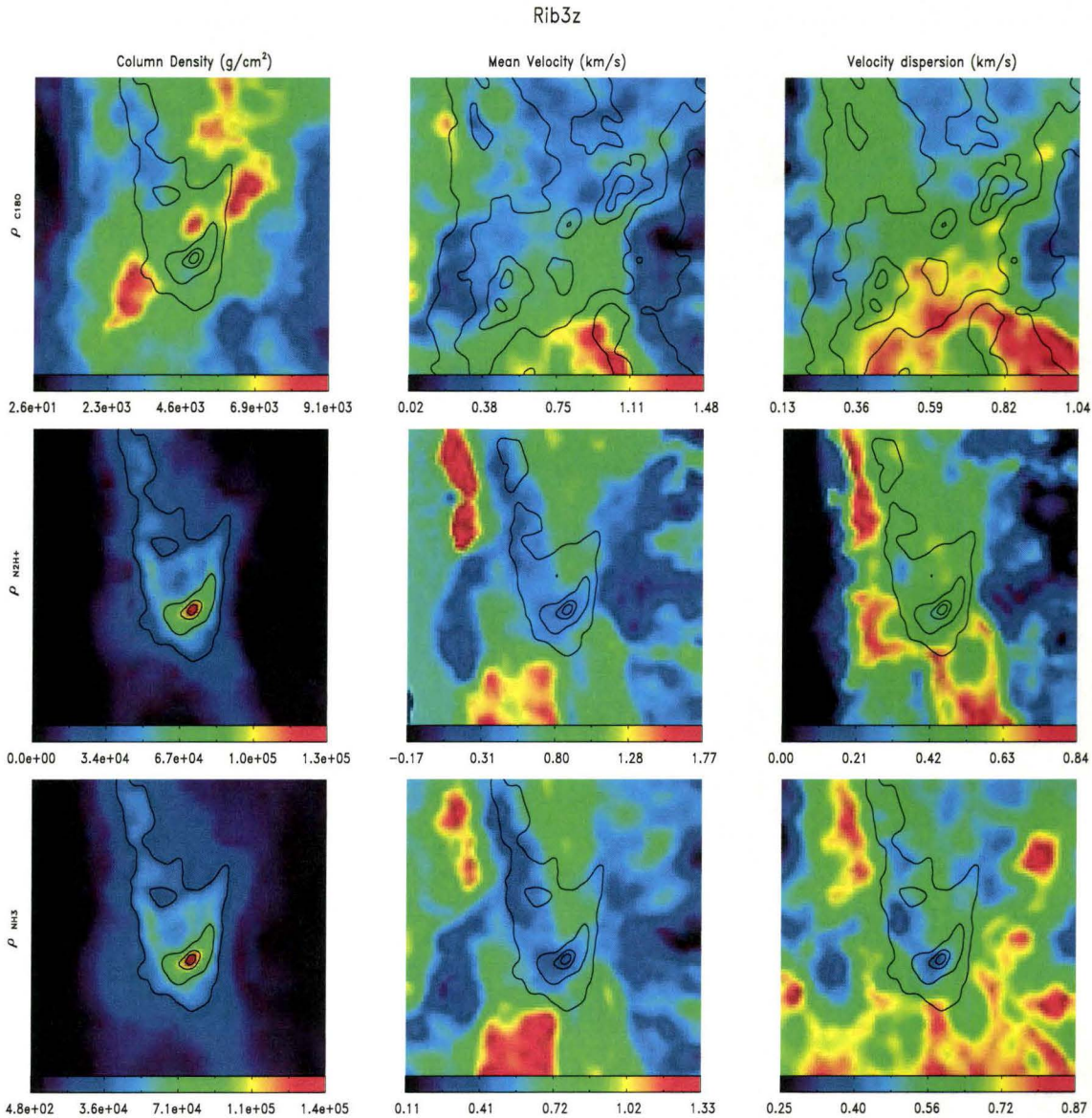


Figure 4.8 Same as Figure 4.7 but this time the lines of sight are going through the z axis. The observed structure is significantly different.

gas flows colliding onto that object. The anti-correlation of velocity dispersion and column density is seen for the $\rho_{N_2H^+}$ and ρ_{NH_3} density ranges. The CR cores are seen in $\rho_{N_2H^+}$, but not in $\rho_{C_{18}O}$. They are therefore already denser objects than the observed starless cores, and would correspond better to young prestellar cores.

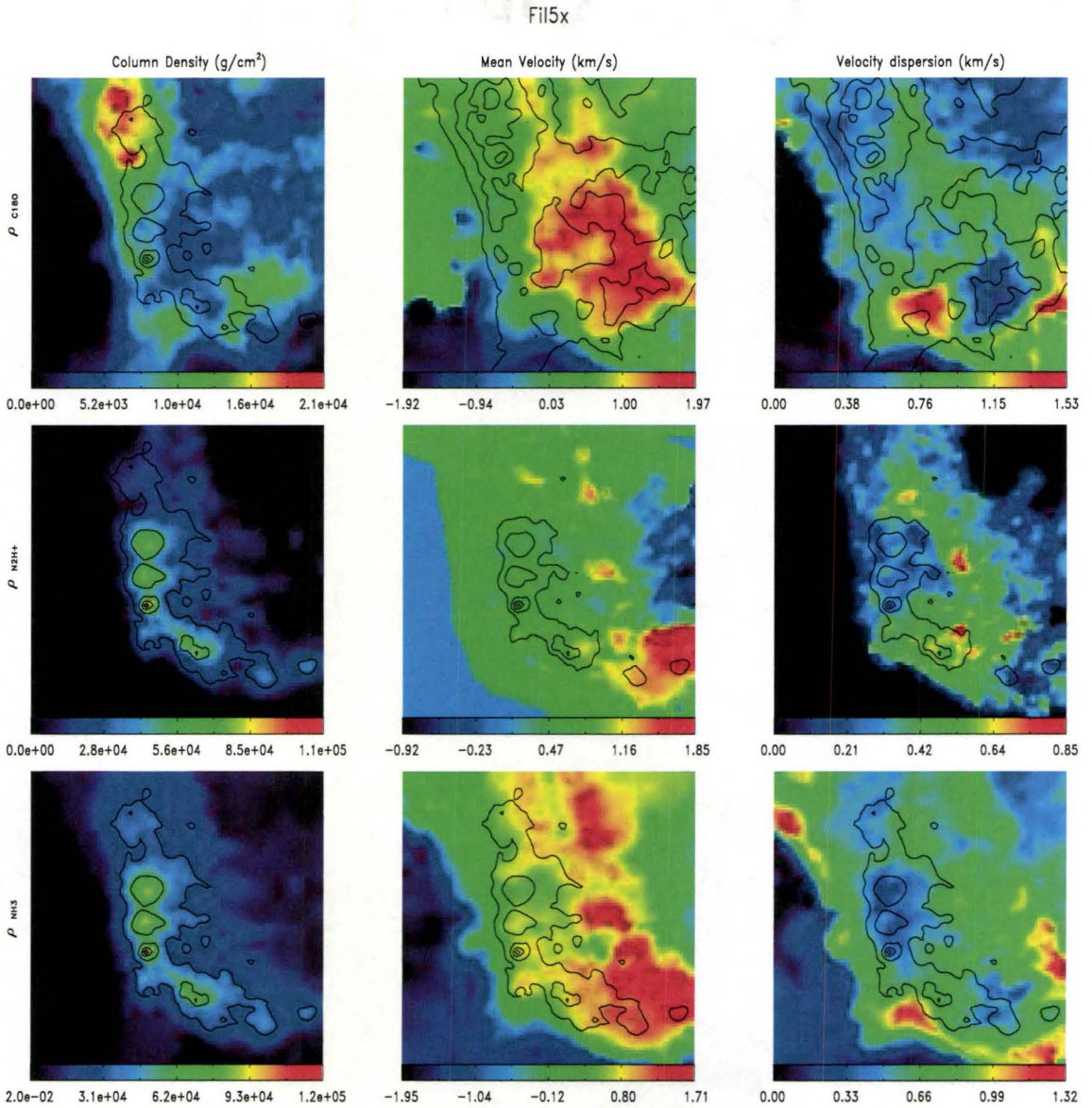


Figure 4.9 Same as Figure 4.7 but for Fil5, a typical CR core, seen through the x axis. The image size shown is 56000×56000 AU.

The core Fil3 (Figure 4.11) is a spherical isolated example of a CC core. There is, again, an anti-correlation of velocity dispersion with column density and no sign of rotation. The CC objects correspond well to the observed prestellar cores.

Figure 4.13 shows the core Fil1, with a dense nucleus (N). The mean ve-

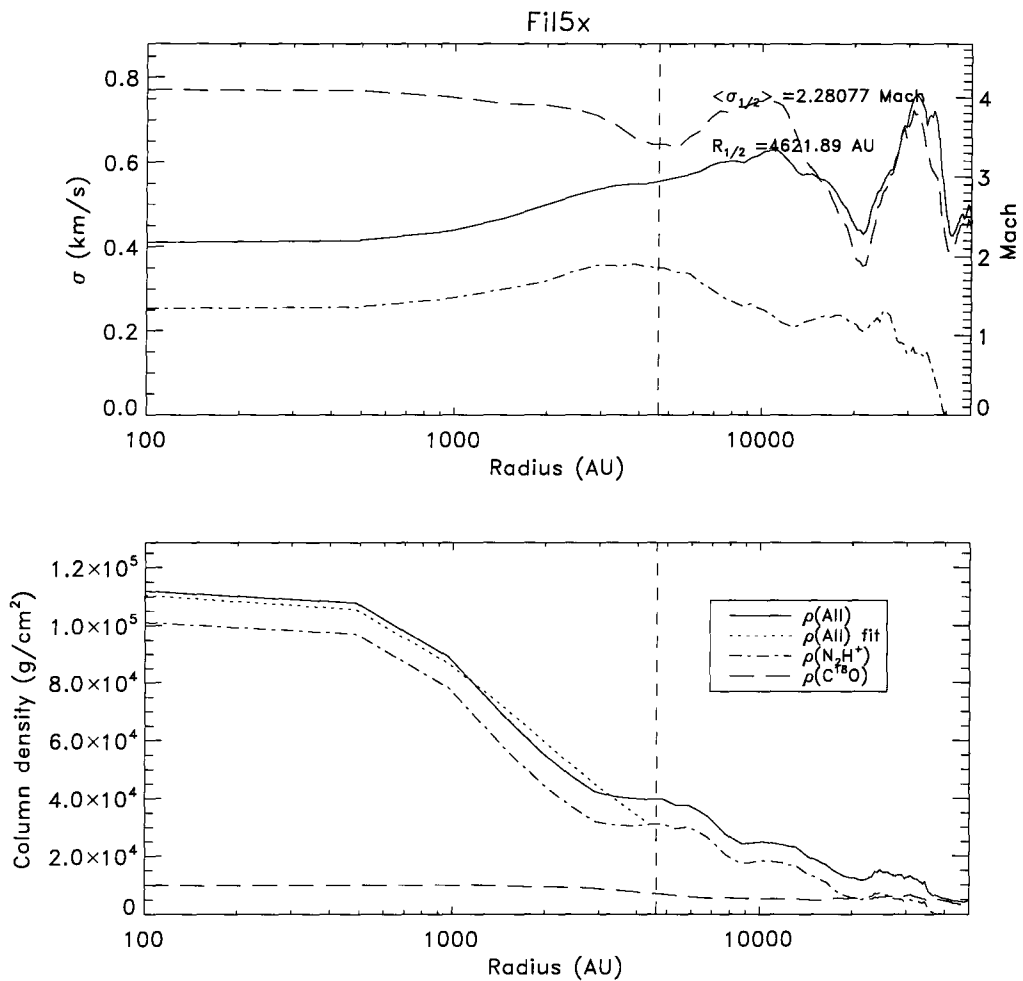


Figure 4.10 Radial profile of the typical CR core Fil5. The top panel shows the radial distribution of velocity dispersion. The bottom panel shows the column density profile. The fit to the density profile for the NH_3 line (labeled as all) is shown by the dotted line. The short dashed vertical line on each panel represent the half-maximum radius ($R_{1/2}$).

locity maps shows small scale rotation near the nucleus. This rotation around the nucleus is generally associated with dense filaments rapidly infalling with a slight rotation. The core Fil1 also shows the velocity dispersion increase at the center created by the gas infalling on the nucleus. The N cores with their central nucleus correspond well to the observed protostellar cores.

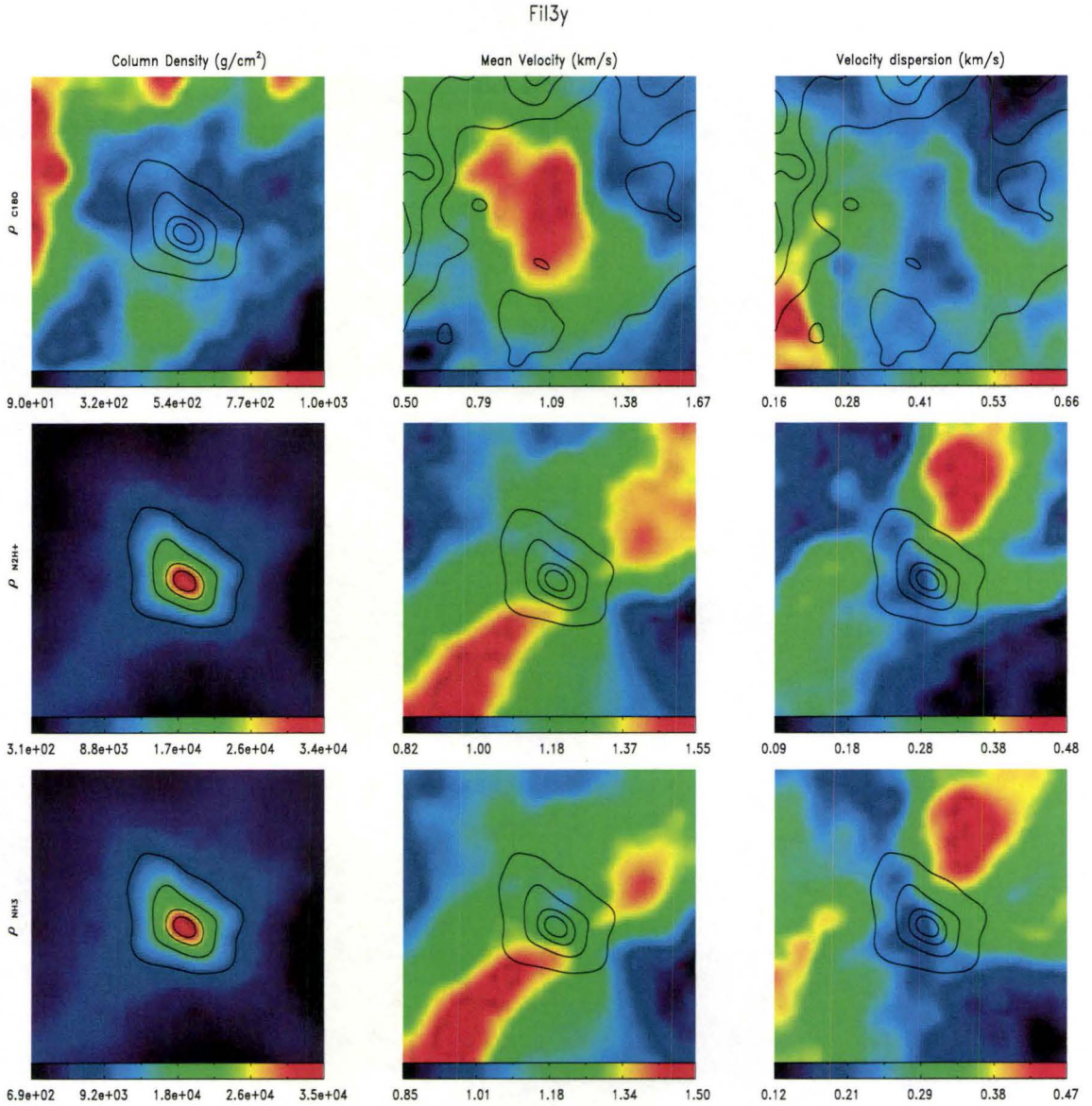


Figure 4.11 Same as Figure 4.5 but for Fil3, a typical CC core, seen through the y axis. The image size shown is 16000×16000 AU.

We also show an example (Rib6) of a *fake* core in Figure 4.16, this “core” is not seen in the $\rho_{N_2H^+}$ density range. However, the same “core” is seen through the whole cloud in Figure 4.15 where it really looks like a dense core. The densest object seen through the line of sight, shown in Figure 4.16 is still very low density and shows a dramatically different structure and

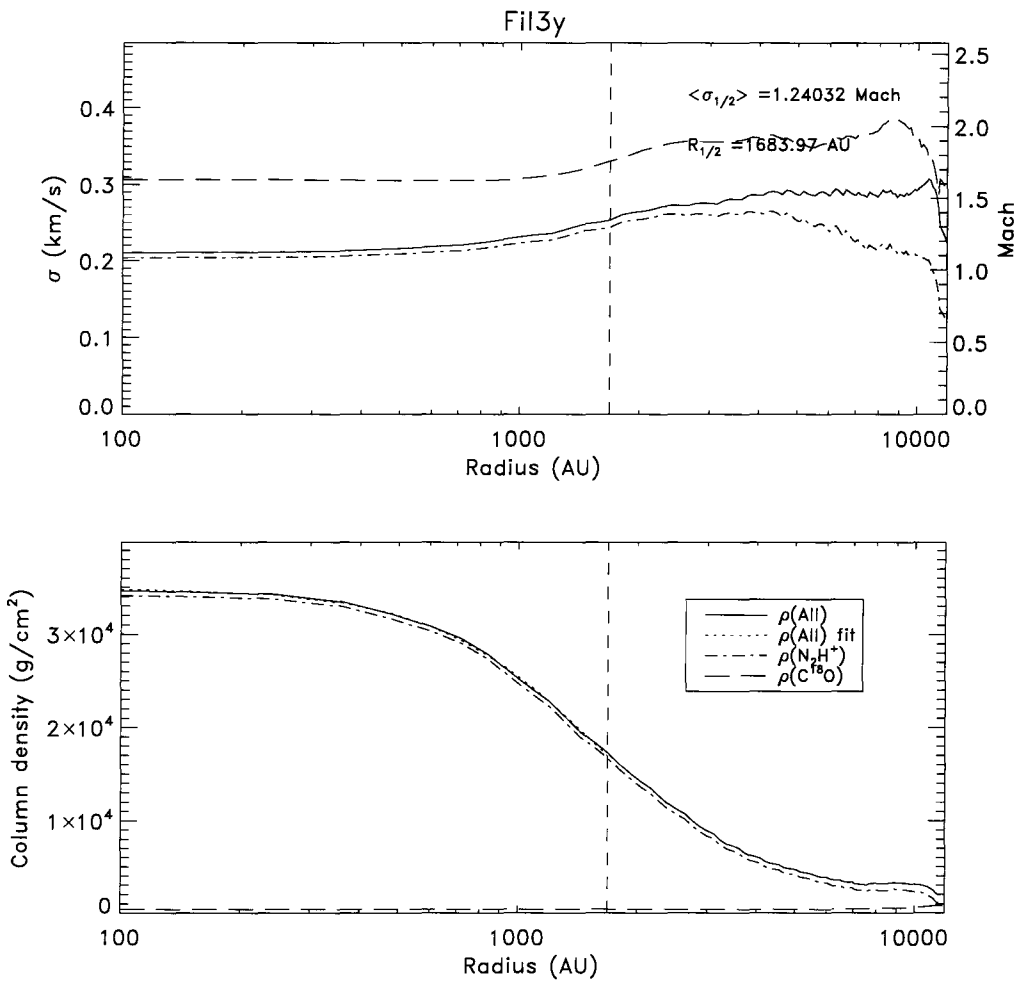


Figure 4.12 Same as Figure 4.10, but for Fil3, a typical CC core, seen through the y axis.

dynamics.

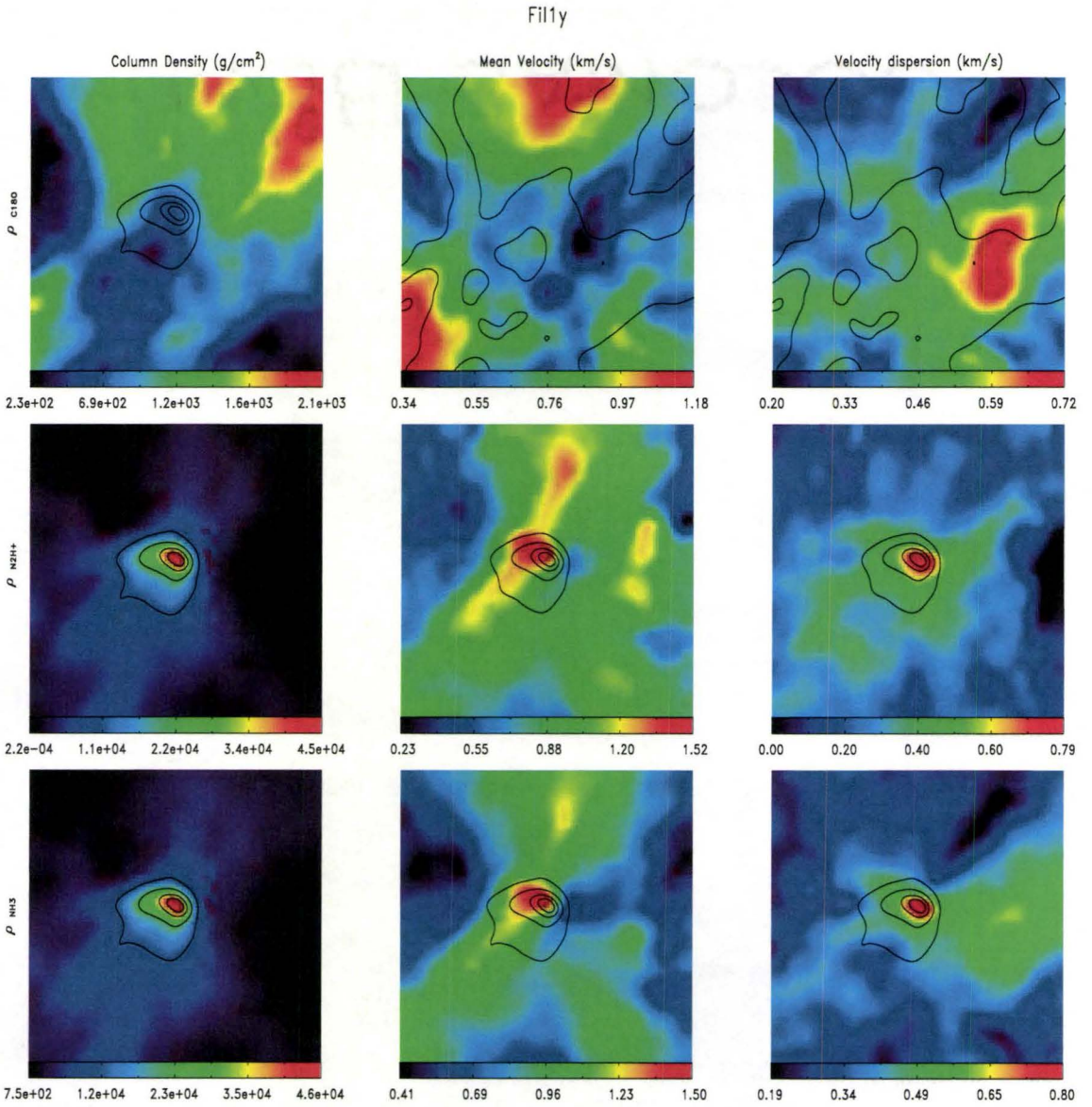


Figure 4.13 Same as Figure 4.5 but for Fil1, a typical N core, seen through the y axis. The image size shown is 20000×20000 AU.

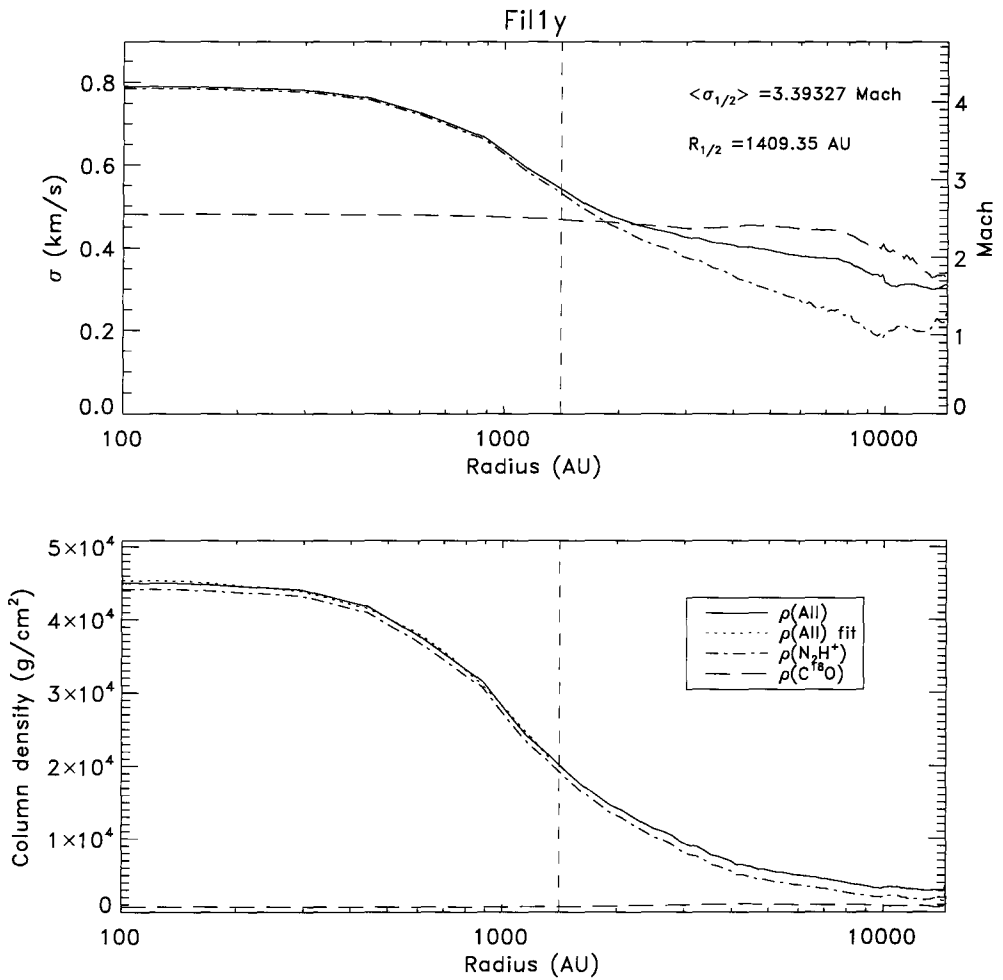


Figure 4.14 Same as Figure 4.10, but for Fil1, a typical N core, seen through the y axis.

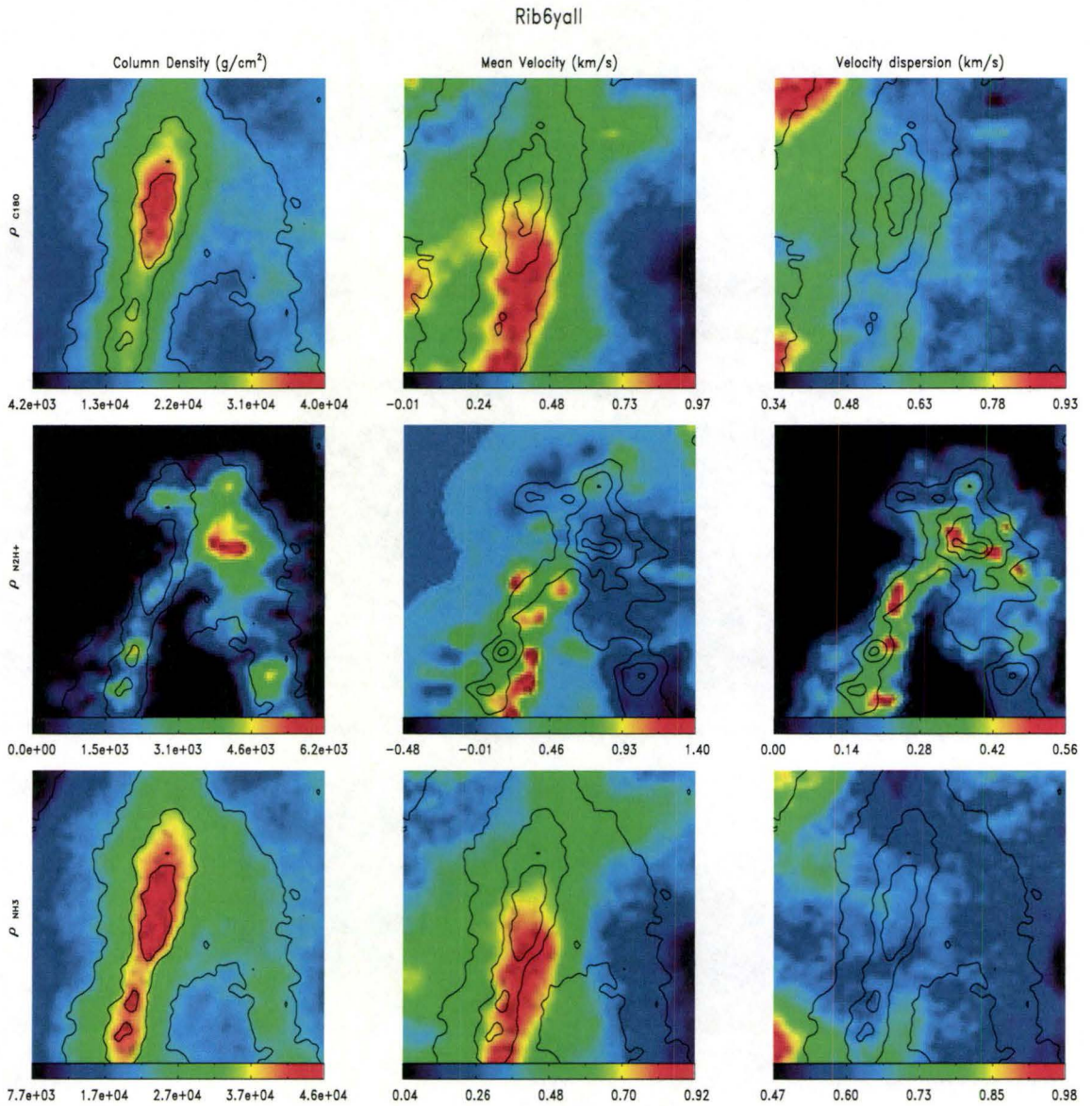


Figure 4.15 Same as Figure 4.6 but for Rib6, a *fake* core showing a structure very similar to a dense core, seen through the y axis. The image size shown is 32000×32000 AU.

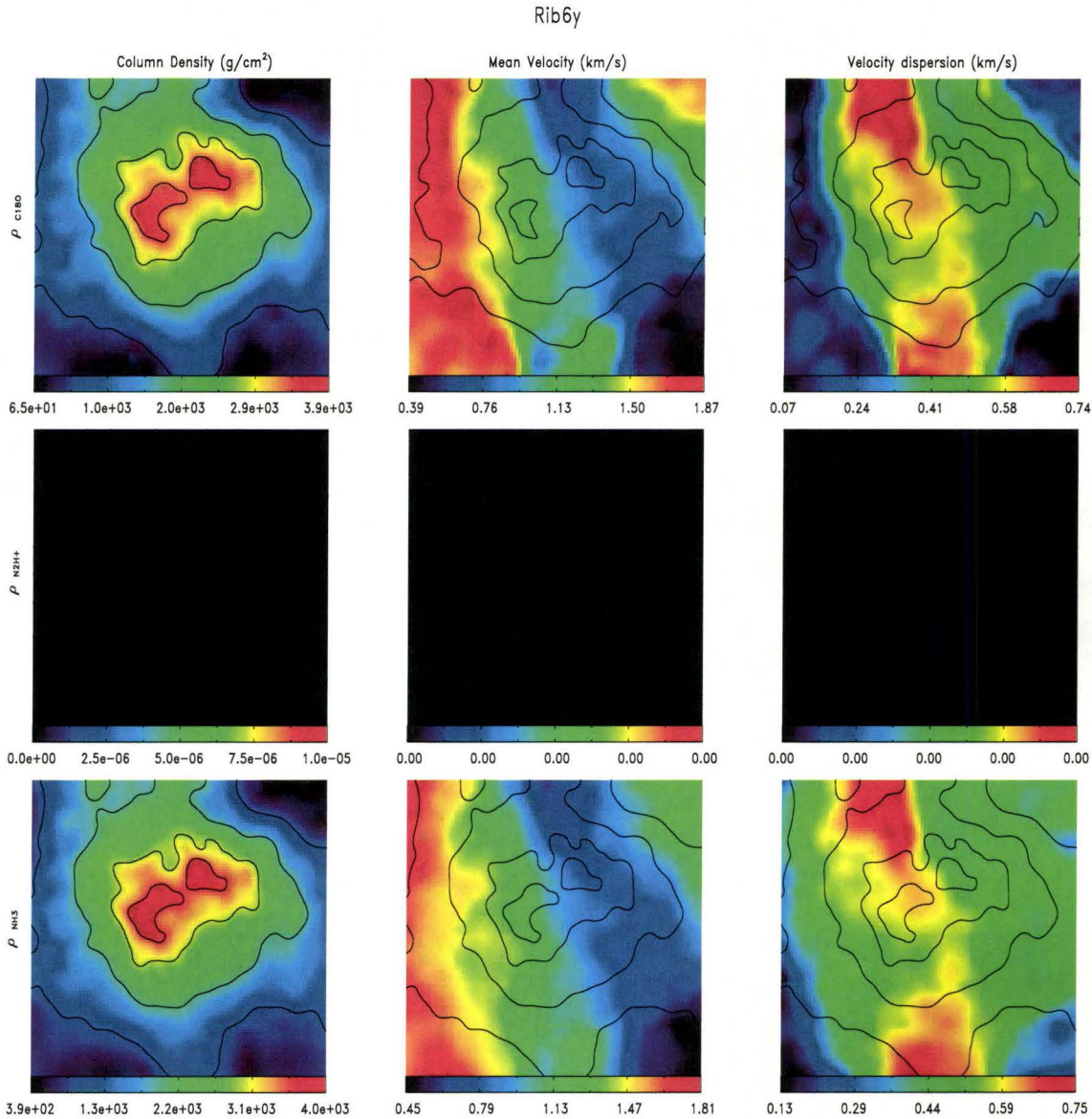


Figure 4.16 Same as Figure 4.15 but here the lines of sight went only through a 32000 AU cube box around what looked the most like an object along the line of sight, which is a fairly low density core. The “object” is not seen at all in the $\rho_{\text{N}_2\text{H}^+}$ density range. The image looks dramatically different from the image 4.15, due to a low density filamentary structure aligned in the line of sight.

4.6 Density profiles

From this section to section 4.11.1, we will do statistics on the 19 real cores we identified previously, seen through 3 orthogonal directions. This sample of cores was chosen as being representative of the variety of cores (CC, CR and N) found in our simulations. The statistical validity of this sample selection is discussed in section 4.4.

From the column density map of the ρ_{NH_3} density range, we investigated the density profiles of the cores. We fit the averaged column density as a function of radius plotted for examples in Figures 4.10, 4.12 and 4.14. We found most cores were very well fit, down to $R_{1/2}$, with the analytical density profile (Tafalla et al., 2002)

$$n(r) = \frac{n_0}{1 + (r/r_0)^\alpha}. \quad (4.5)$$

where the free parameter n_0 is the central density, r_0 is the radius of the “flat” part of the core and α is the asymptotic power index of the decrease in column density near the edges. Even though we simply assumed spherical symmetry in our column density profile, the relation fit every core almost perfectly, except when $R_{1/2}$ is slightly too large and we fit part of the profile turning back towards a flat relation with radius. The fitting parameters for every core are shown in table 4.5. In Figure 4.17, we show the statistical distribution of the fitted parameters for all the cores and also by core types. Note that n_0 and r_0 are distributed on a logarithmic scale. The histograms by core types shows that N cores tends to have steeper decrease in column density near the edges, with larger α , and a smaller “flat” central part, with smaller r_0 . On the

Table 4.4. Mean values and standard deviations of the density profile fit parameters for all cores and for every core type.

Type	α	$\log(r_0 \text{ [AU]})$	$\log(n_0 \text{ [g/cm}^2\text{)})$
All	1.67 ± 0.41	3.38 ± 0.17	4.89 ± 0.31
N	1.87 ± 0.29	3.18 ± 0.14	4.86 ± 0.41
CC	1.82 ± 0.21	3.38 ± 0.19	4.79 ± 0.39
CR	1.27 ± 0.37	3.51 ± 0.18	4.99 ± 0.20

other hand CR cores are generally the opposite with smaller α and larger r_0 , whereas CC core are somewhere in between. From n_0 , we see that CR cores tend to have larger column density, since they are larger objects. The mean values found supporting these arguments are shown in table 4.4. This suggests a density profile evolution from large objects with slowly decreasing density near the edge, to a smaller more centrally concentrated object with sharper density cut at the edges. This trend could potentially be used to estimate the evolution status of observed cores. Obviously, we couldn't include the *fake* cores in this study, since they don't really have a core to fit.

This relation was found to fit observed cores profiles very well (Tafalla et al., 2002, 2004). The observed values of α range from 2 to 3.5 and r_0 ranges from 2700 to 10100 AU. Our α values range from 0.3 to 2.3 with an overall average of 1.67. Our r_0 values range from 943 to 7359 AU with a global average of 2074 AU. Our r_0 values therefore agree fairly well, but our α are smaller. Part of the difference could be caused by our spherical assumption. The irregularities would be smoothing out the column density decrease at the edges. Tafalla et al. (2002) considered an elliptical shape for the cores potentially reducing this effect. Also the more centrally concentrated cores

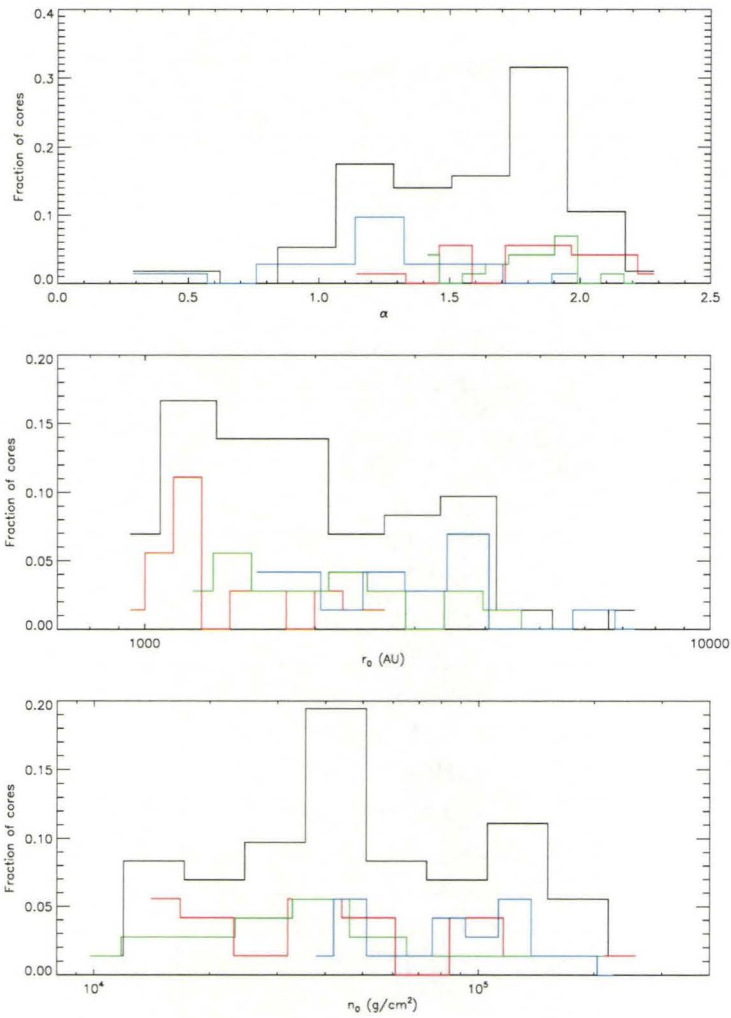


Figure 4.17 Statistical distribution of the density profile parameters. The black histogram is for all the cores, the red one is for N cores, the green one is for CC cores and the blue one is for CR cores.

tend to have larger α values and these cores are more likely to be targeted for observations. Other simulations of turbulent self-gravitating clouds (Tilley & Pudritz, 2004) reported density profiles of ρ^{-2} for very dense cores, but for less concentrated objects they also found a “flat” inner section and a power-law decrease near the edge of $\rho^{-0.5}$.

Table 4.5. Properties and fitting parameters for every core we looked at in details, from the 3 different angles.

Core	Type	M (M_{\odot})	R (AU)	σ_{core} (km/s)	n_0 (g/cm ²)	r_0 (AU)	α
Sph1x	N	2.05624	3843.12	0.387300	103143.	2655.52	1.14307
Sph1y	N	1.92608	2482.43	0.627249	218323.	2158.61	1.52924
Sph1z	N	2.91516	2845.66	0.675625	257083.	2449.96	1.36477
Sph2x	CR	1.28384	4179.57	0.240158	50154.9	3311.34	1.18272
Sph2y	CR	2.09715	4185.66	0.451169	82294.3	3678.32	1.33384
Sph2z	CR	4.98909	6063.92	0.918033	94106.3	4325.81	1.33676
Sph3x	CC	0.303589	1519.92	0.133276	30721.9	1440.27	2.21039
Sph3y	CC	0.744110	1962.21	0.374176	46755.3	1871.01	1.84853
Sph3z	CC	1.41132	2470.92	0.530103	55505.1	2356.81	1.75048
Sph4x	CC	0.655831	2302.14	0.147823	45558.8	2049.08	1.98281
Sph4y	CC	1.02722	2411.54	0.283159	64823.2	2166.61	1.95677
Sph4z	CC	1.75248	2791.46	0.690354	83246.9	2438.62	1.80329
Sph5x	F	0.707741	6058.54	0.469697	4719.35	5236.79	1.12749
Sph5y	F	1.84427	6465.52	0.536509	11090.9	3525.97	0.971496
Sph5z	F	3.39152	7090.39	0.610684	15955.6	5094.67	1.36564
Sph6x	F	0.307619	10840.4	0.149682	1076.37	3589.91	-2.50142
Sph6y	F	0.564329	9789.14	0.316853	2427.39	6138.41	1.08341
Sph6z	F	1.27935	12051.8	0.590000	3103.19	9395.25	0.963246
Fillx	N	0.152215	1139.61	0.675678	18152.5	1157.05	2.24785
Filly	N	0.562668	1409.35	0.638613	45723.8	1238.95	2.22677

Table 4.5 (cont'd)

Core	Type	M (M_{\odot})	R (AU)	σ_{core} (km/s)	n_0 (g/cm ²)	r_0 (AU)	α
Fil1z	N	0.735336	1306.19	0.979906	68463.1	1208.12	2.07906
Fil2x	N	0.203808	1654.53	0.274740	14089.7	942.707	2.09497
Fil2y	N	0.183944	1150.73	1.21812	22902.3	1078.64	2.20776
Fil2z	N	0.368422	1381.98	1.08613	32509.2	1324.92	1.88260
Fil3x	CC	0.620948	1743.41	0.116030	21381.3	1572.57	1.96011
Fil3y	CC	0.952998	1683.97	0.233427	34896.0	1634.62	2.03059
Fil3z	CC	1.52704	1836.73	0.903646	46988.5	1858.39	1.82636
Fil4x	CR	1.27884	3231.19	0.166389	84280.8	2290.57	1.98552
Fil4y	CR	3.16698	4439.57	0.279281	111749.	3096.62	1.64769
Fil4z	CR	4.18473	4456.74	0.434991	144785.	3899.37	1.31259
Fil5x	CR	1.82967	4621.89	0.429241	124734.	1854.96	1.27186
Fil5y	CR	9.49973	9467.85	0.744014	155065.	4313.35	0.653554
Fil5z	CR	16.3758	9976.10	0.677540	224087.	7359.00	1.44122
Fil6x	F	1.02812	3301.83	0.170364	95835.1	2691.55	1.31737
Fil6y	F	2.34865	3929.13	0.310647	162306.	3396.89	1.41780
Fil6z	F	3.88537	4934.64	0.414523	175638.	4131.76	1.24671
Rib1x	N	0.210926	1505.45	0.240816	16494.6	1167.04	1.91284
Rib1y	N	0.554064	1921.56	0.327284	25644.2	1778.29	1.53851
Rib1z	N	1.35669	2451.47	0.356978	39045.2	2196.99	1.63278
Rib2x	N	0.209359	1330.34	0.678855	18680.1	1312.40	1.91956

Table 4.5 (cont'd)

Core	Type	M (M_{\odot})	R (AU)	σ_{core} (km/s)	n_0 (g/cm ²)	r_0 (AU)	α
Rib2y	N	0.441134	1391.16	1.22121	37538.0	1283.01	1.84270
Rib2z	N	0.606373	1372.73	1.23784	53313.0	1290.47	1.89117
Rib3x	CR	0.800511	2928.07	0.217531	50784.2	1577.42	1.72748
Rib3y	CR	3.65423	5921.75	0.548452	57067.5	2125.61	0.989242
Rib3z	CR	1.80569	2537.60	0.474334	142525.	2181.46	1.31959
Rib4x	CC	0.348472	2382.99	0.138242	9797.72	2281.80	1.92088
Rib4y	CC	0.905616	3025.66	0.497930	15656.4	3037.41	1.98735
Rib4z	CC	1.27785	2881.24	0.432090	23875.6	3088.74	1.89357
Rib5x	CC	0.984428	4378.04	0.179144	17013.1	4995.36	1.48486
Rib5y	CC	2.06325	4566.59	0.235746	33512.1	4252.22	1.41605
Rib5z	CC	3.06994	4450.81	0.356490	51530.5	4095.97	1.59654
Rib6x	F	0.512803	8664.07	0.114705	2978.86	8301.34	1.26553
Rib6y	F	1.08258	10398.0	0.557838	3989.19	13206.9	1.10213
Rib6z	F	1.45718	9489.98	0.682751	6682.09	10718.4	1.32643
Sheet1x	N	0.244906	1074.75	0.494544	102881.	1071.00	2.28274
Sheet1y	N	0.589054	1546.83	0.638232	129200.	1216.15	1.64824
Sheet1z	N	1.25517	1883.55	0.713906	182120.	1535.87	2.05847
Sheet2x	N	0.289660	1339.88	0.341983	25258.0	1235.71	1.99337
Sheet2y	N	1.02369	1840.33	0.445917	49288.4	1640.01	1.92463
Sheet2z	N	1.80443	2185.10	0.549375	60173.1	1800.53	1.82206

Table 4.5 (cont'd)

Core	Type	M (M_{\odot})	R (AU)	σ_{core} (km/s)	n_0 (g/cm ²)	r_0 (AU)	α
Sheet3x	CC	0.342695	1236.08	0.180829	147093.	1318.49	1.46381
Sheet3y	CC	0.763668	1718.70	0.362525	174152.	1215.48	1.93190
Sheet3z	CC	1.74403	2451.47	0.669154	212272.	1473.60	1.73680
Sheet4x	CR	0.762103	2857.39	0.324677	37910.3	1670.57	1.43555
Sheet4y	CR	3.14051	4823.08	0.640606	54601.4	2828.27	1.03762
Sheet4z	CR	6.59595	6287.61	0.555054	54394.8	4378.62	0.288555
Sheet5x	CR	1.07901	2679.18	0.378352	84834.7	2204.18	1.38583
Sheet5y	CR	2.16316	3343.58	0.704506	107217.	2994.21	1.29967
Sheet5z	CR	4.18933	4270.11	0.760877	126442.	3858.17	1.21572
Sheet6x	F	0.834040	4659.55	0.172412	11033.0	4146.46	0.964123
Sheet6y	F	2.04885	5788.19	0.935237	18158.6	4465.08	1.04891
Sheet6z	F	2.69781	6111.86	0.885133	20751.2	5505.31	0.982822

4.7 Velocity dispersion

The velocity dispersion inside cores may be generated from various mechanisms: turbulence, infall, outflow, rotation or thermal. The thermal contribution can easily be estimated from $\sigma_{thermal} = \sqrt{kT/m_{molec.}}$. The thermal velocity dispersion is generally considered to be small compared to the observed values. Chen et al. (2007) report a non-thermal average of 0.15 km/s for a thermal contribution of 0.055 km/s from their sample. The mechanisms that dominates the significant non-thermal velocity dispersion is still a matter of debate.

Dense cores are observed to have constant velocity dispersion throughout their inner region. Barranco & Goodman (1998) observed, with NH_3 molecular lines, a constant velocity dispersion inside the cores, but measured an increase at large radius. They suggest a “radius of coherence” ($R_{coh} \sim 20000$ AU) within which the gas becomes coherent, the contribu-

tion of the non-thermal turbulent motions is small and the velocity dispersion approximately constant. Tafalla et al. (2004) made high resolution observations of 2 starless cores and measured a constant subsonic non-thermal velocity dispersion ($\sigma_{NT} \approx 0.048 - 0.051$ km/s) throughout the cores, from $NH_3(1,1)$ and $N_2H^+(1-0)$ molecular lines. They however observed no increase at high radius (9800 - 13300 AU). Chen et al. (2007) observed (using N_2H^+) the velocity dispersion to be roughly constant inside the cores and generally larger near the edges.

As suggested by Figures 4.10, 4.12 and 4.14 the velocity dispersion for $\rho_{N_2H^+}$ of the CR and CC cores are usually near sonic, and sometimes subsonic in the middle. They also show an increase near the edges towards a supersonic surrounding as generally observed. The N cores on the other hand are supersonic inside the core due to infall and rotation and decrease near the edges. However, we saw large variations in the velocity dispersion radial distribution between cores of a given type and even for a given core seen through different axes.

4.7.1 Velocity dispersion with size of cores

To measure the velocity dispersion inside our cores, we first defined the size of our objects from the column density maps, in a similar way to the method observers use. We took all the pixels with a column density larger than half the maximum value minus the minimum value (acting as the equivalent of a noise level for our images). Then we measured the total area covered by these pixels and defined the radius of a circle covering that area as our half maximum radius ($R_{1/2}$). Similarly, we define the velocity dispersion of cores (σ_{core}) as

the averaged velocity dispersion of the pixels with a column density above the half-maximum value. The velocity dispersion is generally flat in the center of the core and increase near the edges. The $R_{1/2}$ we defined are generally close to the point where the velocity dispersion starts to really increase, see Figures 4.10, 4.12 and 4.14 for examples. Therefore the averaged value is close to the minimum value observed at the center of the core.

In Figure 4.18 we plotted σ_{core} as a function of $R_{1/2}$. We compared our data to the observed power-law relation (Caselli et al., 2002) $\sigma_{core} \propto size^{0.51}$ (dotted line) for N_2H^+ cores of size ranging from 3700 to 33800 AU. Such a trend is not seen in our data. Chen et al. (2007) measured no such trend either from their observations of smaller objects (1000 to 4000 AU). They suggest that cores becomes “coherent” at size below 10000 AU. Our results are in agreement with this transition.

The average velocity dispersion for cores smaller than 10000 AU (dashed line) is 0.50 km/s, which is supersonic (2.66 Mach). Many cores have sub- or trans-sonic velocity dispersions, in agreement with observations (Goodman et al., 1993; Caselli et al., 2002; Tafalla et al., 2004; Chen et al., 2007). However, we also found many cores at supersonic values larger than observed. Most of these cores are small and their high velocity dispersion could be explained by the accretion/rotation around a dense central object. These processes may not be resolved by observations, or prevented from happening by an physical source of support not included in our simulations.

This discrepancy is also noticed in most core formation simulations (Tilley & Pudritz, 2004; Klessen et al., 2005; Offner et al., 2008). Simulated cores tends to have trans- to super-sonic velocity dispersions. A proposed argument (Offner et al., 2008) to explain this issue for almost perfectly protostars

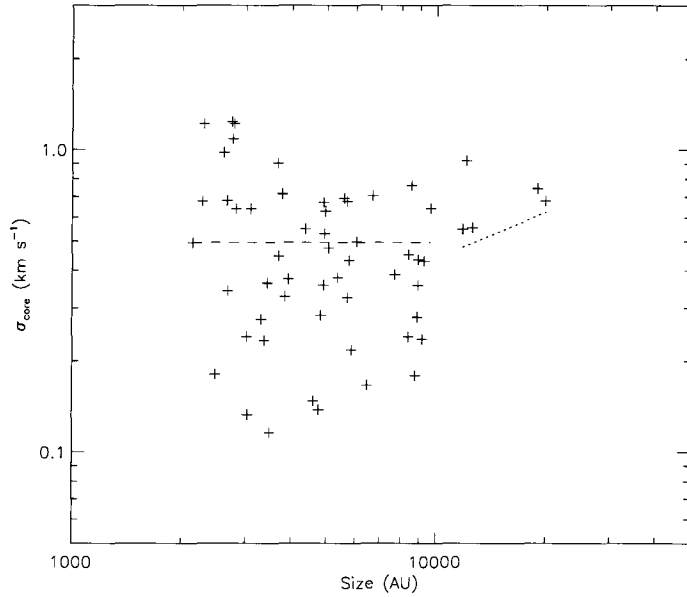


Figure 4.18 Mean velocity dispersion inside the cores in function of their size. The observed power-law, from Caselli et al. (2002) data, is also shown (dotted line). The average velocity dispersion for cores smaller than 10000 AU is also shown (dashed line).

showing strong gas infall is the lack of outflow in the simulations. The outflows could significantly reduce the mass of the forming objects and therefore reduce the infall motion to the protostar. However, the problem with prestellar objects remain and outflows could also increase the velocity dispersion depending on the viewing angle. They also mention the lack of magnetic support. The specific effects of magnetic fields in core formation remain uncertain, but it is likely to slow down the collapse, giving more time for the gas to become “coherent” before any significant infall happens. This could significantly reduce the observed velocity dispersion of cores.

Another possible explanation for this would be a departure from the optically thin assumption near the central dense object. Since most of the infall

and rotation motions in our simulations were observed to be constrained to very small scales around the nucleus, only localized departure from optically thin conditions could explain the lack of observational evidences for these motions.

4.7.2 Velocity dispersion vs. Density relation

The 2D $(N_z, \langle v_z \rangle, \sigma_z)$ maps of our cores shows a general feature: an anti-correlation between column density and velocity dispersion, (see Figures 4.10, 4.12 and 4.14). This feature was also seen in simulations by Padoan et al. (2001), where it was shown to match $C_{13}O$ (1-0) observations. It can be explained by shocks in a supersonic turbulent gas. When two opposite flows of gas shock, they will naturally lose velocity and gain density. This leads to a velocity dispersion-density relation, which can be observed as a column density-velocity dispersion relation.

We found these relations to be approximately power laws ($\sigma \propto \rho^\eta$). In an attempt to quantify this relation in the context of core formation we plotted all the cores on the same $\log(\sigma)$ vs. $\log(\rho)$ plot (Figure 4.19). We did a linear fit to the averaged relation in the density range $2 \times 10^4 \leq n \leq 2 \times 10^6 \text{ cm}^{-3}$ and found $\eta = -0.222$.

We also looked to see if the 3 types of cores had different slopes or amplitude. In Figures 4.20 to 4.22 we plotted the relation for the cores of each type separately. The results of the fits are shown in table 4.6. We see a slightly steeper slope for the CR cores and a shallower one for the N cores. The CR cores have the highest average density and the N cores have the lowest average density. The shallower slope for the N cores can be explained by a significant

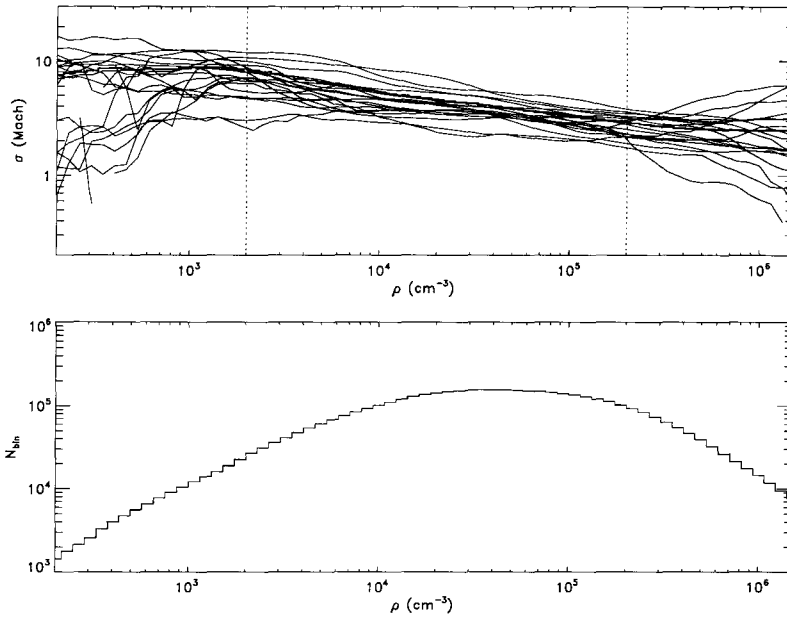


Figure 4.19 Velocity dispersion of density bins for each cores (in grey) and the averaged relation (in black). The range of density included in the fit is indicated by the dashed lines. The linear fit to the mean relation yield a slope $\eta = -0.222$. The total number of particles per density bin is shown in the bottom panel.

increase in the velocity dispersion at high density due to the infall motion of the gas. The gravitational effects can be significant in these cases because of the very dense central nucleus. The CR cores have a higher average velocity dispersion, which contributes to widen the distribution. This suggest that CR cores are “younger” objects, where the gas velocity is not yet relaxed and the gas flow is still actively shocking. Nevertheless, these differences are minor overall, and this relation seems to apply in general to shock-induced cores.

The work of Padoan et al. (2001) on turbulent shocks and our analysis of cores forming within shocks show a $\sigma - \rho$ relation. This relation is the result of the shocks in supersonic turbulent gas, naturally slowing down the

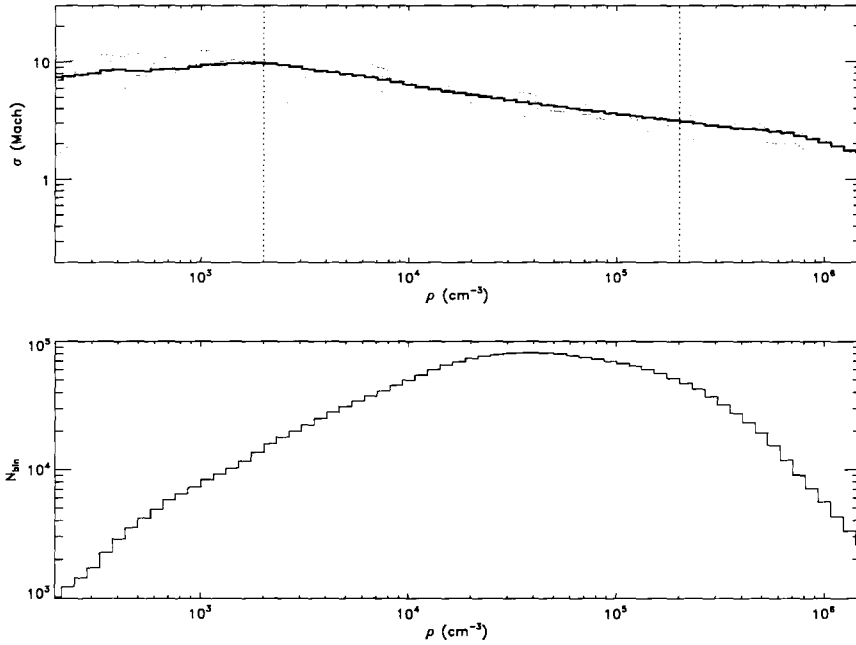


Figure 4.20 Velocity dispersion of density bins for the CR cores (in grey) and the averaged relation (in black), similar to Figure 4.19. The linear fit to the mean relation yield a slope $\eta = -0.253$.

Table 4.6. List of the fit to the $\log \sigma - \log \rho$ relation for each core type. The parameters are for a linear fit with $A + Bx$, where the 1σ uncertainty are for the fit of the averaged relation weighted by the total number of particles in each density bin ($1/\sqrt{N_{\rho_i}}$).

Cores	A	$1\sigma_A$	B	$1\sigma_B$
CR	1.817	0.007	-0.253	0.002
CC	1.43	0.01	-0.203	0.002
N	1.307	0.009	-0.160	0.002
All	1.625	0.005	-0.222	0.001

dense gas forming within it. If we combine this relation with the $\sigma \propto R^\beta$ Larson’s law (Larson, 1981), we get a $\rho - R$ relation ($\rho \propto R^{\beta/\eta}$). This relation is similar to another Larson’s law that is thought to be an observational artifact

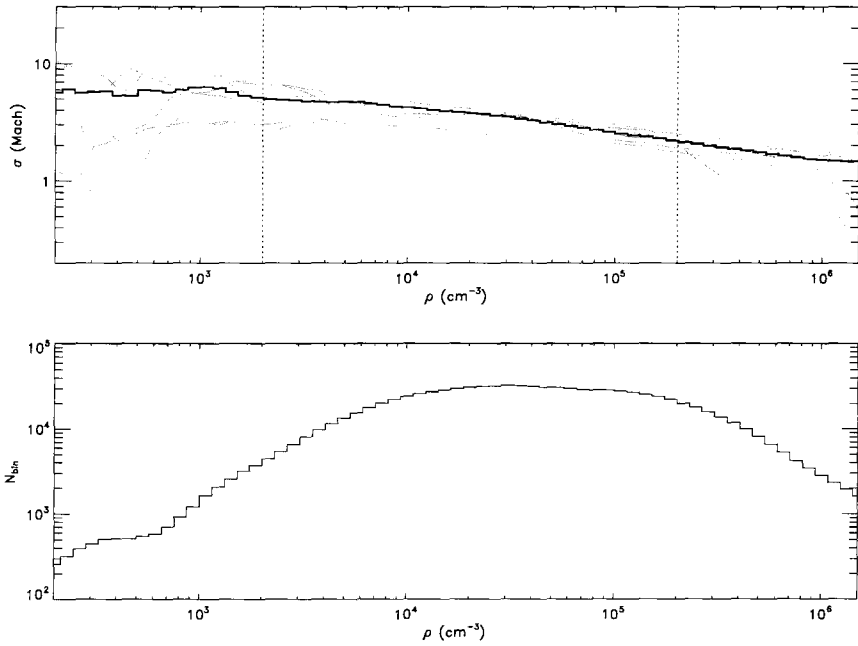


Figure 4.21 Velocity dispersion of density bins for the CC cores (in grey) and the averaged relation (in black), similar to Figure 4.19. The linear fit to the mean relation yield a slope $\eta = -0.203$.

(Kegel, 1989; Scalo, 1990). They claim that observations of molecular data in particular are restricted to regions where the column density is large enough for the molecules to be shielded from the external photo-dissociating radiation, but small enough to be optically thin. Therefore surveys tend to observe regions of approximately constant column density that would naturally lead to $\rho \propto R^{-1}$, see Mac Low & Klessen (2004) for a review.

However, the $\sigma - R$ Larson's law is believed to be a real physical consequence of the supersonic turbulent cascade (Mac Low & Klessen, 2004). The $\rho - R$ relation therefore seems hard to avoid. It may be hard to observe, but it seems to be physically motivated.

If we combine the two original Larson's laws ($\alpha = -1.1$, $\beta = 0.38$)

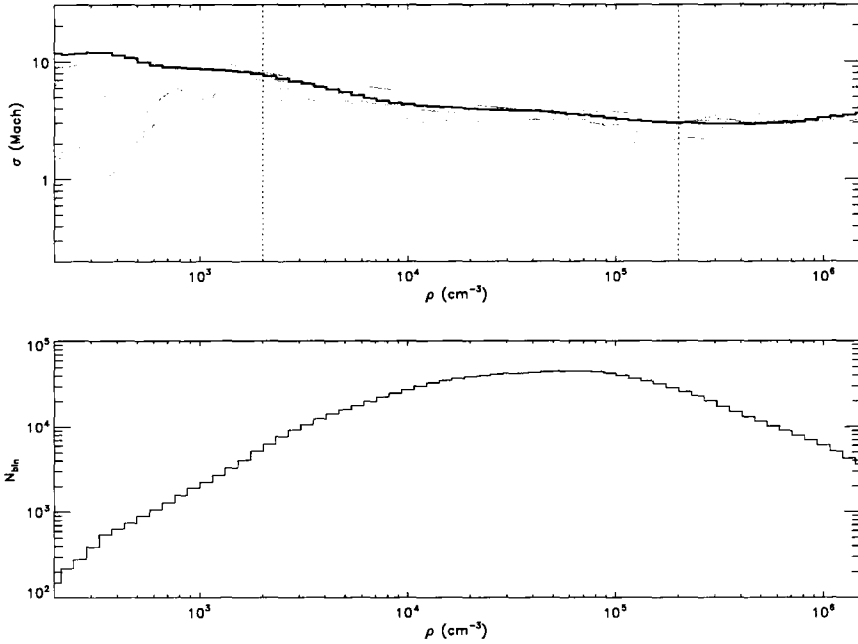


Figure 4.22 Velocity dispersion of density bins for the N cores (in grey) and the averaged relation (in black), similar to Figure 4.19. The linear fit to the mean relation yield a slope $\eta = -0.160$.

together, we get $\eta = \beta/\alpha = -0.345$, which is not too far off from our value considering the significant divergence observed in the measures of β alone.

4.8 Mean velocity

The core kinematics can also be studied with the mean velocity along the lines of sight (v_z) maps. The velocity dispersion provide information on infall motions and turbulence within the cores, but rotation can produce a systematic velocity gradient measurable from mean velocity maps.

Observations of low-mass cores have shown little (Chen et al., 2007) to no signs (Di Francesco et al., 2001; Caselli et al., 2002; Tafalla et al., 2004) of systematic variations indicating rotation. This is in good agreement with

what is seen in our mean velocity maps. For most of the cores, we see complex motions and no clear velocity gradient across the cores. Only N type cores show clear signs of rotation, as the gas quickly accretes and rotates in a more or less coherent pattern. This is perhaps what explains the clear rotation observed in massive protostellar objects (Beltrán et al., 2004). The large amount of surrounding gas can rotate as it is infalling onto the dense central protostellar object. However, our simulation cannot be directly compared to these massive objects.

To measure the velocity gradients throughout the maps we followed the method used by Goodman et al. (1993) that was also used for other observations (Tafalla et al., 2004; Caselli et al., 2002; Chen et al., 2007). The method consists of fitting a linear gradient (∇v_z) to the whole velocity map. We therefore performed a least mean square fit to the function

$$v_z = v_0 + a\delta x + b\delta y \quad (4.6)$$

where v_0 is the bulk velocity of the core, and a and b are the velocity gradients on the x and y axis of the map respectively. We can then measure the magnitude of the global velocity gradient of the map from

$$|\nabla v_{los}| = \sqrt{(a^2 + b^2)}. \quad (4.7)$$

We fitted the velocity maps of the 19 “real” cores in 3 perpendicular directions (x, y, z) for the 3 density ranges. For $\rho_{C^{18}O}$, we found a typical velocity gradient of $3.58 \text{ km s}^{-1} \text{ pc}^{-1}$ and values ranging from 0.45 to $11.49 \text{ km s}^{-1} \text{ pc}^{-1}$, see Figure 4.23 for the distribution. For $\rho_{H_2H^+}$, we found a mean velocity gradient of $2.85 \text{ km s}^{-1} \text{ pc}^{-1}$ and values ranging from 0.27 to 15.23

$\text{km s}^{-1} \text{pc}^{-1}$ and for ρ_{NH_3} , we found a mean velocity gradient of $3.17 \text{ km s}^{-1} \text{pc}^{-1}$ and values ranging from 0.34 to $9.10 \text{ km s}^{-1} \text{pc}^{-1}$. Figure 4.23 shows that the three distributions are similar and peaked below or around $1 \text{ km s}^{-1} \text{pc}^{-1}$.

Goodman et al. (1993) found gradients ranging from 0.3 to $2.5 \text{ km s}^{-1} \text{pc}^{-1}$ from NH_3 molecular lines. Observations of the same cores with N_2H^+ molecular lines (Caselli et al., 2002) however showed no correlation of the gradients measured with the 2 tracers. But most cores had a larger gradient in N_2H^+ , leading to a averaged gradient ratio $\langle |\nabla v_{N_2H^+}| / |\nabla v_{NH_3}| \rangle = 1.6 \pm 1.0$. A possible explanation for the larger gradient in the N_2H^+ observations is given by their finer resolution. A larger beam would smooth out the velocity variation across the map, decreasing the observed gradient. Caselli et al. (2002) however found consistent velocity gradients in N_2H^+ and NH_3 for 2 objects using the same instrument. These measurements were also in good general agreement with the values from Goodman et al. (1993) and Caselli et al. (2002).

The resolution is probably also the reason why our measured gradients are higher for some cases. Our convolved velocity maps simulate a beam size of 1000 AU , and the N_2H^+ observations were performed with beam size $\approx 20000 \text{ AU}$.

In Figure 4.24 we compare the gradients measured at $\rho_{C^{18}O}$ and $\rho_{N_2H^+}$, tracing the low and high density gas respectively. The gradients are not correlated. The gradient is often larger for $\rho_{C^{18}O}$ with a averaged gradient ratio, $\langle |\nabla v(\rho_{C^{18}O})| / |\nabla v(\rho_{N_2H^+})| \rangle = 2.31$.

Making the same assumption as Goodman et al. (1993), Caselli et al. (2002) and Chen et al. (2007) we can measure the specific angular momentum

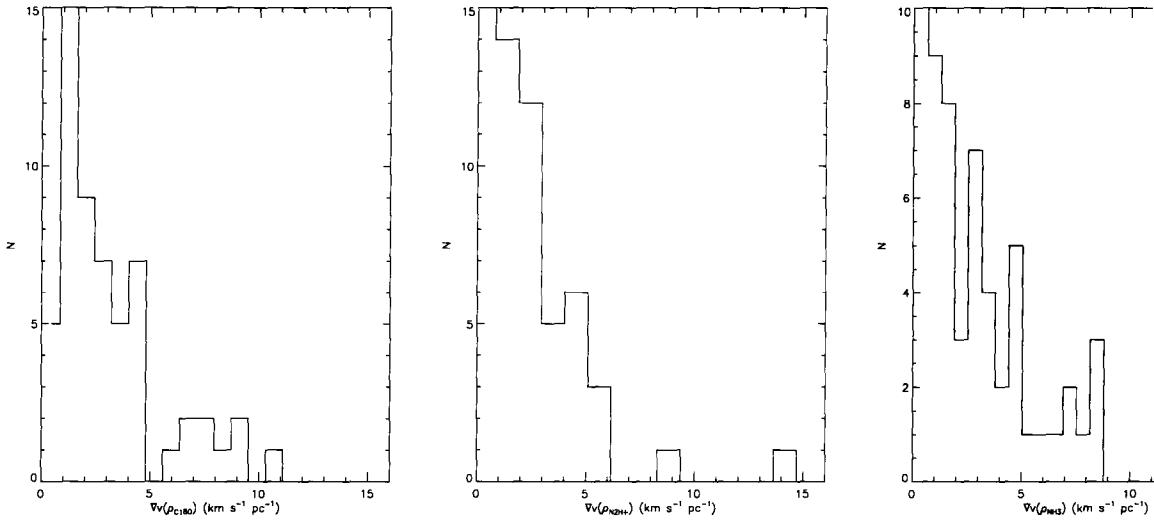


Figure 4.23 Distribution of the measured gradients for the $\rho_{C^{18}O}$ (left) and the $\rho_{N_2H^+}$ (right) density ranges of the 19 cores in the 3 perpendicular directions (x, y, z).

(J/M) and the rotation energy ratio $\beta_{rot} = E_{rot}/E_{grav}$. The specific angular momentum is $J/M = I\omega/M$, where I is the moment of inertia and ω the angular velocity. If we assume a uniform density sphere, we know that $I = 2MR^2/5$. If we neglect the effect of the inclination angle i on the angular velocity we get $\omega = |\nabla v_{los}|/\sin i \approx |\nabla v_{los}|$.

$$\frac{J}{M} \approx \frac{2}{5} |\nabla v_{los}| R^2 \quad (4.8)$$

The typical specific angular momentum we obtain this way is similar for the low density and higher density ranges: $J/M \approx 0.018$ and 0.017 respectively.

The rotation energy is $E_{rot} = I\omega^2/2 \approx MR^2|\nabla v_{los}|^2/5$ making the same approximations. Also, for a uniform density sphere the gravitational energy is $E_{grav} = (3/5)(GM^2/R)$, so the rotation energy ratio becomes

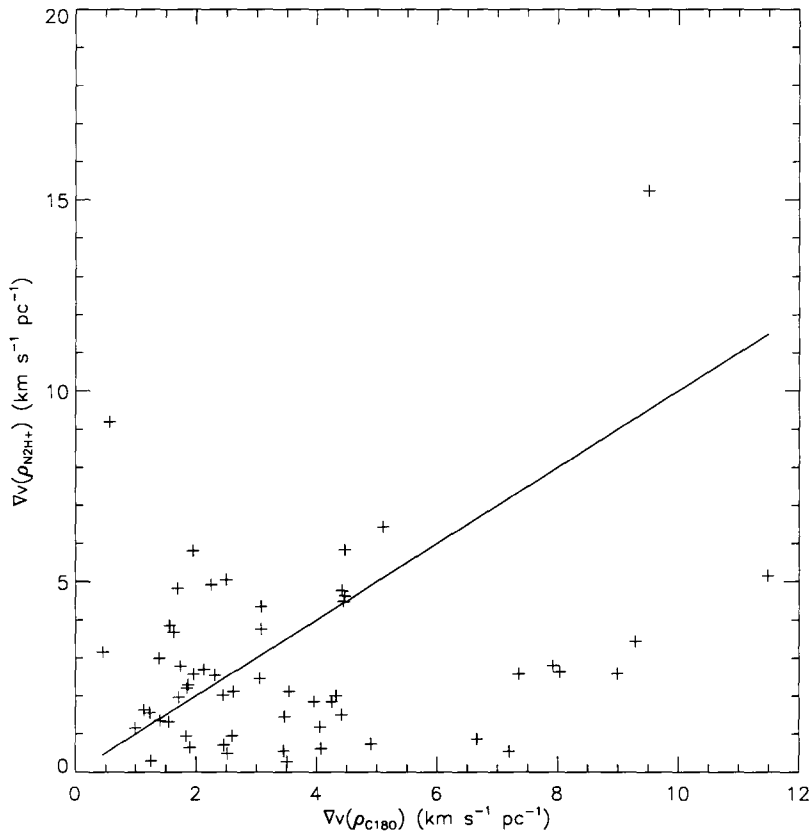


Figure 4.24 Comparison of the velocity gradients measured for each core in the density ranges $\rho_{C^{18}O}$ and $\rho_{N_2H^+}$. The straight line represent the case where both gradients are identical.

$$\beta_{rot} \approx \frac{R^3 |\nabla v_{los}|^2}{3GM}. \quad (4.9)$$

The ratios (β_{rot}) we found for $\rho_{C^{18}O}$ are less than 0.040. For $\rho_{N_2H^+}$ we found ratios less than 0.028 and for ρ_{NH_3} less than 0.075. Figure 4.25 shows the distributions of the ratios is similar for each density range and it spans 3 orders of magnitude.

Barranco & Goodman (1998) found all their cores had $\beta \leq 0.18$ and that most were below 0.05, with 1 outlier at 1.4 and a lowest value of 0.0012.

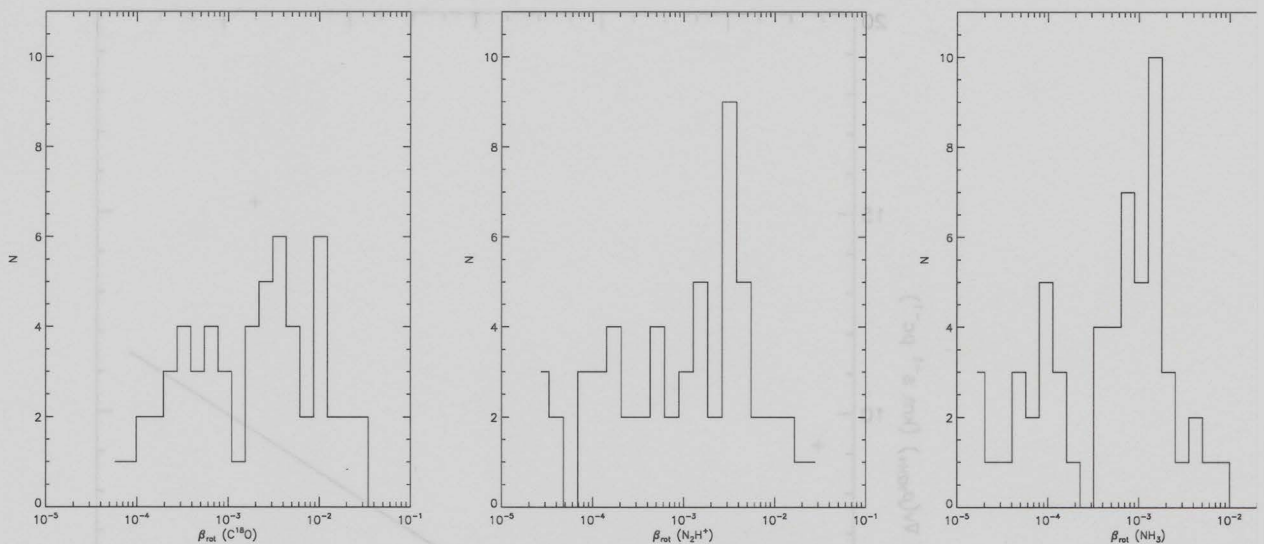


Figure 4.25 Distribution of the measured rotation energy ratio in the $\rho_{C^{18}O}$ (left) and the $\rho_{N_2H^+}$ (right) ranges.

Caselli et al. (2002) found that the N_2H^+ cores had similar β values to the cores also observed in NH_3 with an average of ~ 0.02 and ~ 0.03 respectively.

So our measurement are in good agreement with the observations. We found no cores with $\beta \geq 1$, where rotation would dominate and only a few above 0.01, where rotation may have an effect. But for most cores the rotation observed would be insignificant.

We compared the ratios measured at $\rho_{C^{18}O}$ and $\rho_{N_2H^+}$ in Figure 4.26. The ratios are weakly correlated, with a significant spread. No clear deviation is observed, but the averaged ratio of the ratios, $\langle \beta_{rot}(C^{18}O) / \beta_{rot}(N_2H^+) \rangle = 12.62$, indicates a larger ratio for $\rho_{C^{18}O}$.

Goodman et al. (1993) also observed a relation of these parameters with the size of the objects. Even though the scatter in the data is rather large they found that $J/M \propto R^{1.6}$ and $\nabla v \propto R^{-0.4}$ and that β is independent of size ($\beta \propto R^0$).

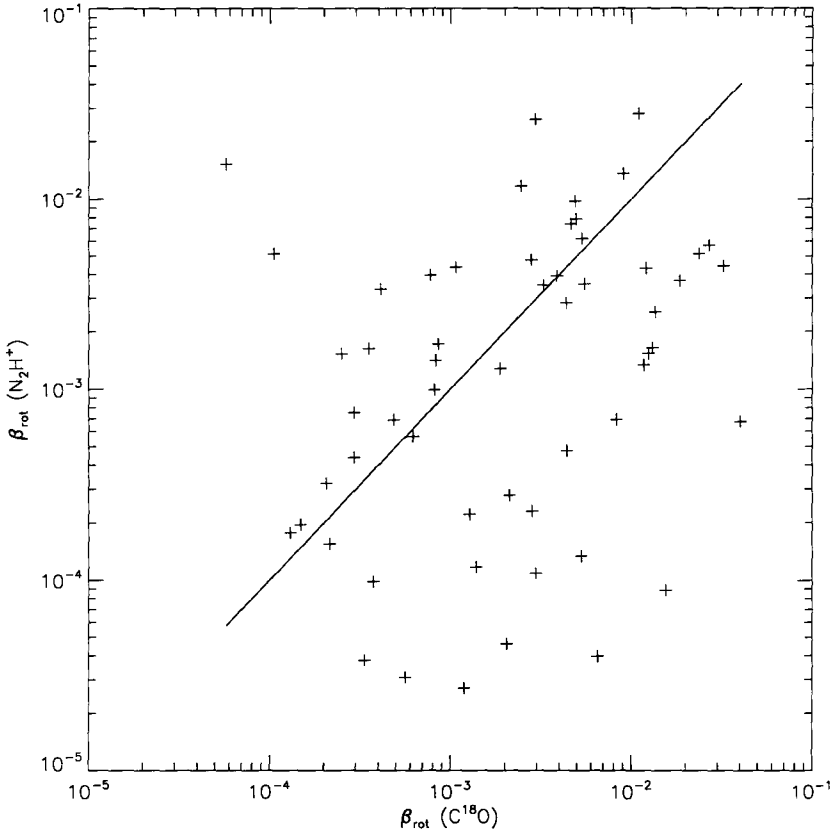


Figure 4.26 Comparison of the rotation energy ratios measured for each core in the density ranges $\rho_{C^{18}O}$ and $\rho_{N_2H^+}$. The straight line represent the case where both ratios are identical.

Figure 4.27 to 4.29 show our results for $\rho_{C^{18}O}$, $\rho_{N_2H^+}$ and ρ_{NH_3} respectively. The slope is fitted and the uncertainty is on the fit only. The results does not differ significantly between density ranges. The power laws we found for J/M are 1.8 ± 0.2 , 1.7 ± 0.2 and 1.8 ± 0.2 , and for ∇v we found -0.2 ± 0.2 , -0.3 ± 0.2 and -0.2 ± 0.2 respectively. These are all in agreement with the observed values (Goodman et al., 1993). However, the power laws we found for β_{rot} , 0.9 ± 0.4 , 0.7 ± 0.5 and 1.0 ± 0.5 respectively, are different than the observed values.

To investigate this discrepancy, we measured directly the specific angular momentum of the cores from the SPH particles. From this we then calculated the velocity gradient and β using the same equations as previously.

We found a typical velocity gradient of $0.247 \text{ km s}^{-1} \text{ pc}^{-1}$ and values ranging from 0.022 to $1.7 \text{ km s}^{-1} \text{ pc}^{-1}$ which is about a magnitude smaller than using the other technique. The plane fitting technique therefore seems to overestimate the measured velocity gradients.

The β we found range from 6.3×10^{-6} to 0.09 , which is similar to the values we found by plane fitting. This confirms that rotation is not dynamically important at such early stages of star formation and that the plane fitting technique give reasonable results.

The results for the scaling with size are shown in Figure 4.30. We found $J/M \propto R^{1.2 \pm 0.4}$ and $\nabla v \propto R^{-0.8 \pm 0.4}$, which are again reasonably close to the observed values considering the uncertainty. But this time β is remarkably independent of size ($\beta \propto R^{0.03 \pm 0.8}$).

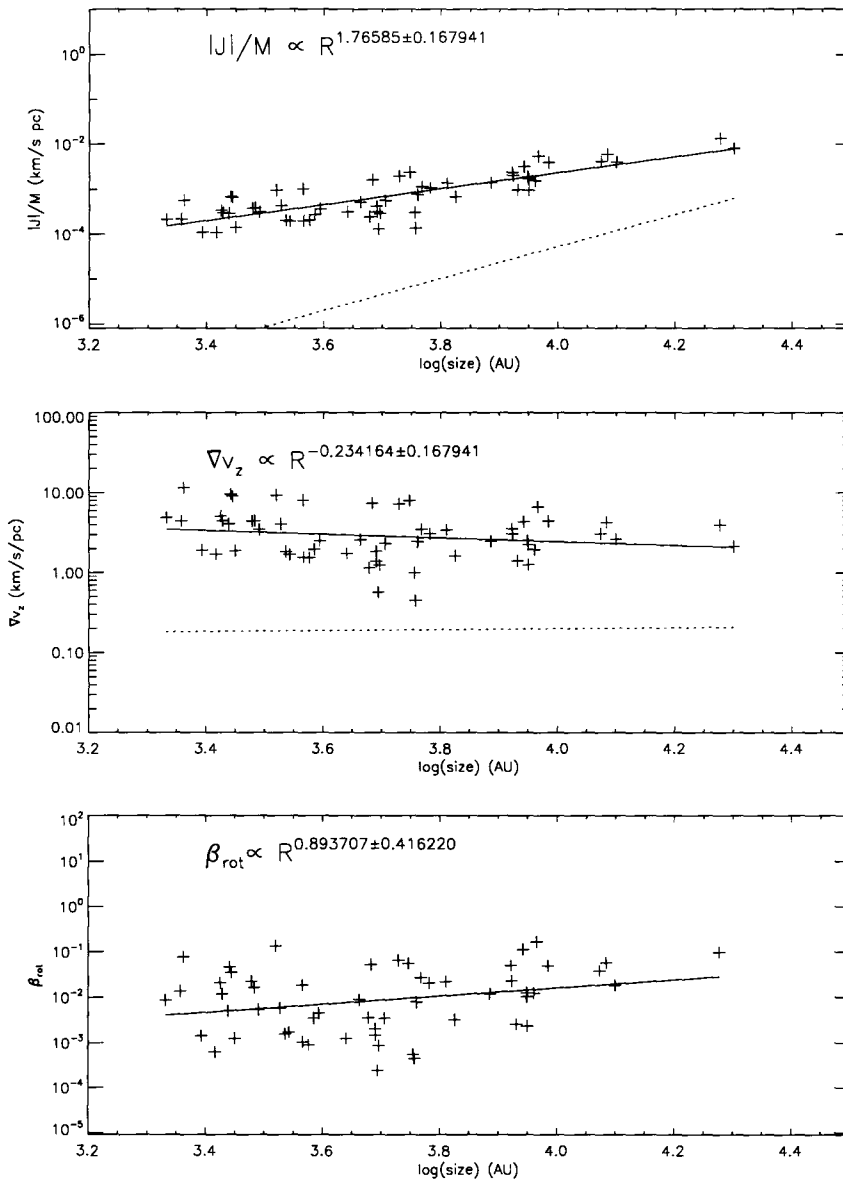


Figure 4.27 Specific angular momentum in function of size (top panel) for each core from 3 perpendicular perspectives. The best linear fit to the data is shown (full line) and also the observed relation by Goodman et al. (1993) $J/M \propto R^{1.6}$ (dotted line). The angular momentum in each direction (x,y,z) have been calculated using the 2D maps of mean velocity for the low density tracers ($\rho_{C^{18}O}$), using a similar technique to Goodman et al. (1993). From the measured velocity gradients (middle panel), we calculated the specific angular momentum ($\nabla v \approx 5(J/M)/2R^2$) and compared to the observed relation $\nabla v \propto R^{-0.4}$ (dotted line). On the bottom panel we plotted the rotation energy ratio, $\beta_{\text{rot}} = E_{\text{rot}}/E_{\text{grav}}$ for which no significant slope is observed.

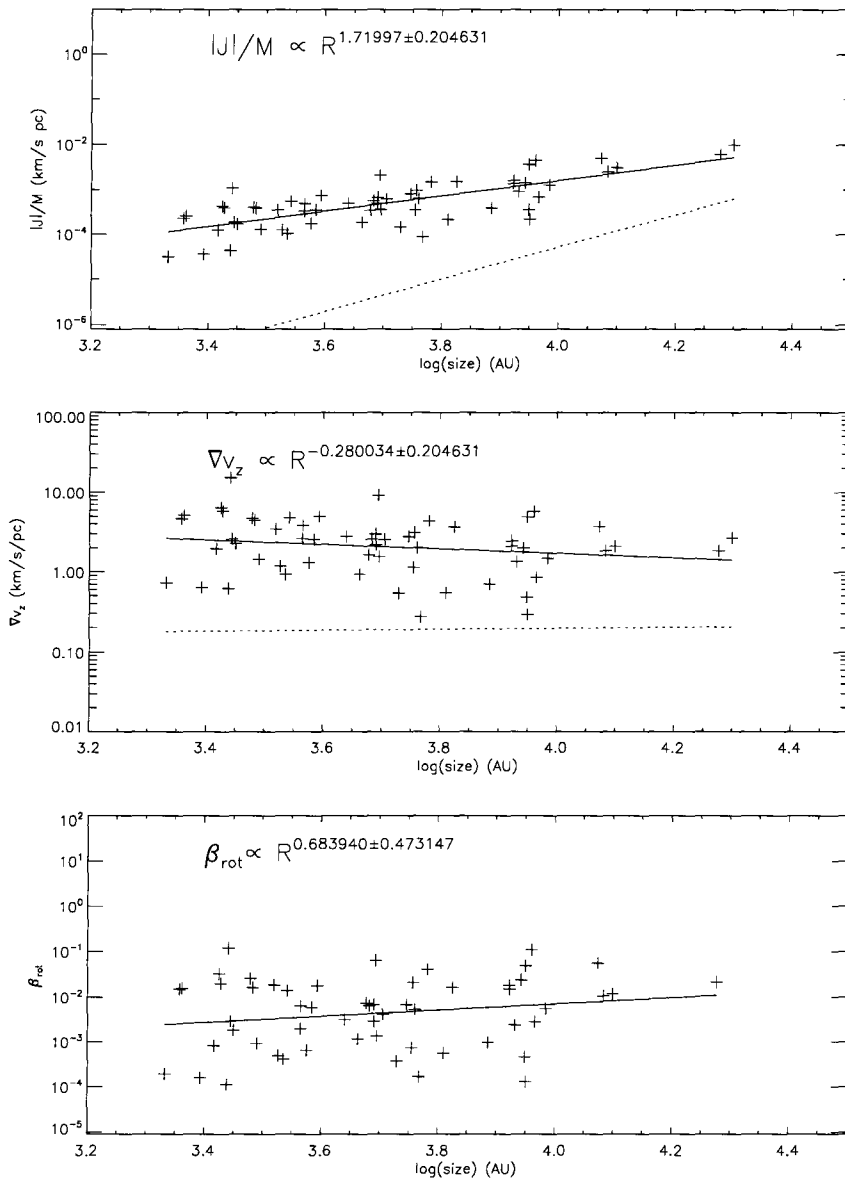


Figure 4.28 Same as Figure 4.27, but for the medium density range ($\rho_{N_2H^+}$).

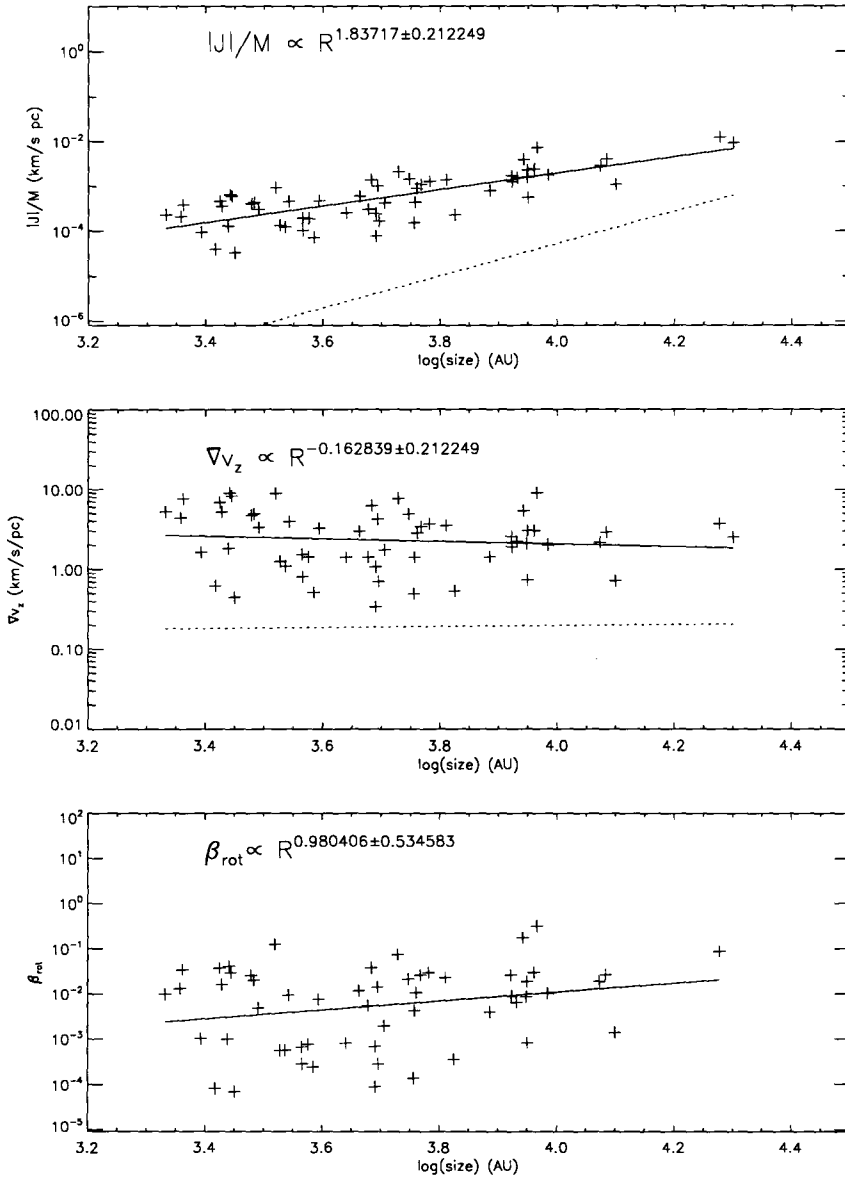


Figure 4.29 Same as Figure 4.27, but for the high density range (ρ_{NH_3}).

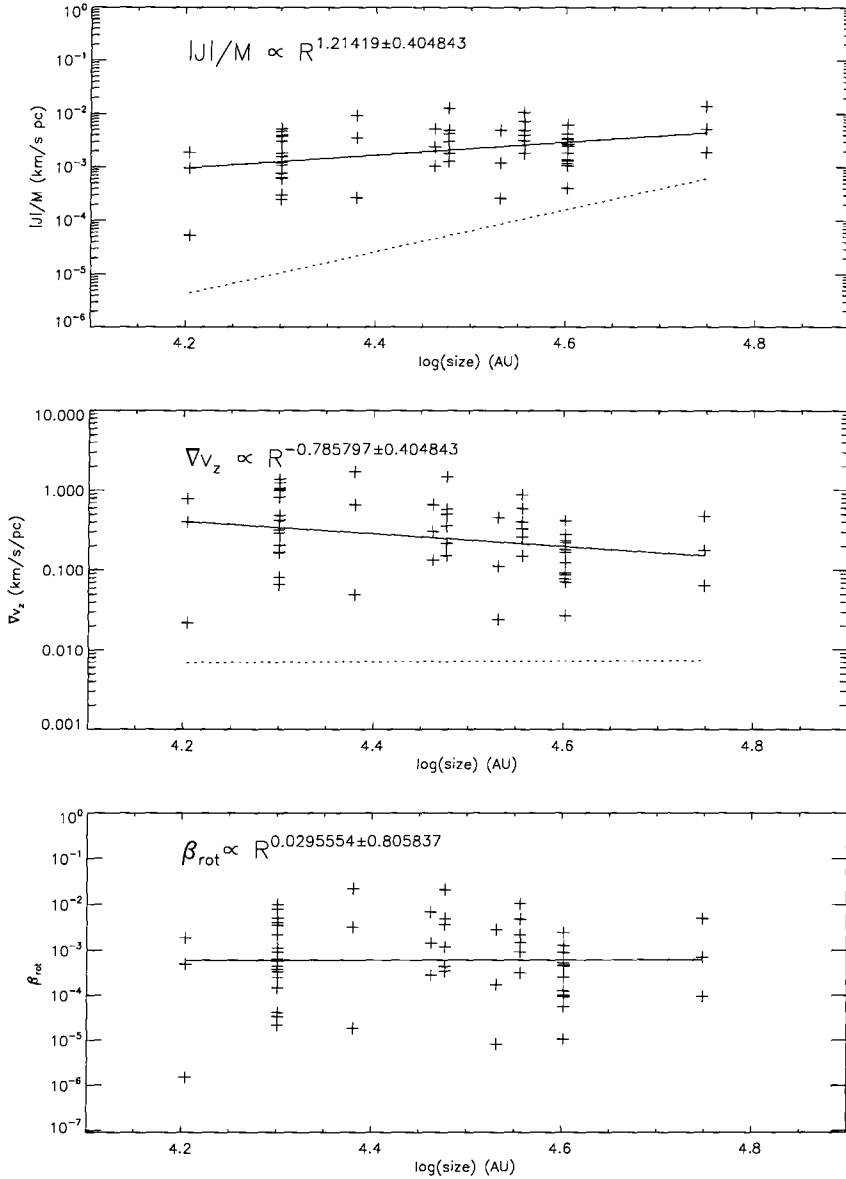


Figure 4.30 Same properties shown in Figure 4.27, but here the specific angular momentum is calculated directly from the sum of all the core particles. We then calculated the velocity gradient and rotation energy ratio from the same formulas used previously.

4.9 Core-Core velocity dispersion

The core to core velocity dispersion (σ_{cc}) is generally compared to the virial velocity dispersion ($\sigma_{vir} = \sqrt{GM/5R}$) of the region around the cores. It represents the 1-D velocity dispersion necessary to prevent the collapse of an object. In the case of virial equilibrium, we would find $\sigma_{cc} = \sigma_{vir}$. Using the initial mass and size of the simulation, we found $\sigma_{cc}/\sigma_{vir} = 0.54$ for $\rho_{C^{18}O}$ and $\sigma_{cc}/\sigma_{vir} = 0.55$ for $\rho_{N_2H^+}$. Our objects are therefore clearly not in virial equilibrium. This is not very surprising since we know our molecular clouds are undergoing gravitational collapse and our objects are just formed.

These ratios are also consistent with the observations. The survey of the Perseus molecular cloud (Kirk et al., 2007) found sub-virial velocity dispersions for a typical ratio around 0.6. For ρ Ophiuchus, Peretto et al. (2006) also found sub-virial velocity dispersions by a factor ~ 3 .

4.10 Core-envelope velocity dispersion

Previous studies (Walsh et al., 2004, 2007; Kirk et al., 2007) investigate the motion of the dense cores, observed with N_2H^+ , and their envelope, traced with $C_{18}O$. They have shown that cores and their envelope are quiescent. Almost all cores were found to have a velocity difference with their surrounding medium less than the sound speed. This argument was used against the theory of competitive accretion, where a high velocity difference could help increase the accretion rates, by Ayliffe et al. (2007). But Kirk et al. (2007) reconciled these observations to simulations showing competitive accretion by showing they also had sub-sonic velocity differences.

In Figure 4.31, we plotted the histogram of the difference in the mean velocity of the cores calculated from $\rho_{C_{18}O}$ and $\rho_{N_2H^+}^+$. The difference calculated from $\rho_{C_{18}O}$ and $\rho_{N_2H^+}$ had some variations. The distribution is approximately Gaussian with a standard deviation of $\sigma = 0.22$, and therefore very few objects have supersonic velocity difference. These results are in agreement with the Kirk et al. (2007) measurements. They found a Gaussian distribution with a standard deviation of $\sigma = 0.17$ for starless cores and $\sigma = 0.16$ for protostars.

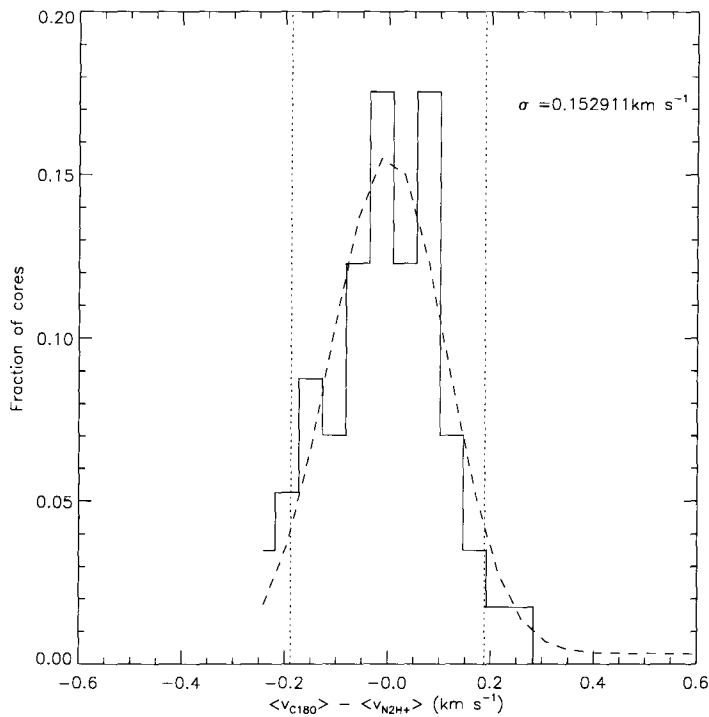


Figure 4.31 Difference in the mean velocity (on the line of sight) of the cores in $\rho_{C_{18}O}$ and $\rho_{N_2H^+}^+$. We fitted a Gaussian to the data, shown by the dashed line, with $\sigma = 0.22$. The dotted lines represent the speed of sound, showing that very few cores have supersonic velocities with respect to their envelope.

4.11 Core observed mass

By integrating the column density along the line of sight with column density above the half-maximum, we can define the half-maximum mass ($M_{1/2}$). We can compare the integrated mass ($M_{1/2}$) to the virial mass using $R_{1/2}$ and $\sigma_{1/2}$ defined in a coherent way. The approximation of a uniform density sphere with effective linewidth Δv_{eff} , and

$$M_{vir} = 210R[pc]\Delta_{eff}^2[km/s] \quad (4.10)$$

is commonly used (Caselli et al., 2002; Tachihara et al., 2002; Klessen et al., 2005), where $\Delta v_{eff} = (8 \ln 2)\sigma$. The results are plotted in Figure 4.32. The mass equipartition $M_{1/2} = M_{vir}$ is represented by the full line. This figure indicates that all our cores are not virialized, however some are close. The dotted line represents the energy equipartition $E_{Kin} = E_{Grav}$ where $M_{1/2} = M_{vir}/2$, which indicates the limit of bound cores. Therefore many of our cores are measured to be bound and most are close. This is what was expected since we saw clear accretion features in most N cores, so we would at least expect them to be bound. We have to be careful here because the velocity dispersion is not necessarily dominated by turbulence, as it is assumed here. The accretion on a bound core would also increase the velocity dispersion. This can explain the larger spread at small radius (see Figure 4.18); the strong accretion in the filamentary structures, observed for the N cores, which tend to be smaller in size, will increase the velocity dispersion significantly in the lines of sight along this filament.

But most of the gas surrounding the N cores is not showing strong accretion features, only along the dense filaments where density is higher and

velocity dispersion locally smaller. It is possible that only this dense gas would really be bound to the core and most of the rest would still be dominated by turbulence.

This result is consistent with observed starless cores which also tend to have larger virial mass than the measured mass. The cores of Tachihara et al. (2002), which do not have a central protostar, have a mass < 10 times smaller than their estimated virial mass. This is where most of our cores are also found. We estimate an averaged departure from equipartition by a factor ~ 3 , from our data. However, Morata et al. (2005) found departure by a factor ~ 30 and Caselli et al. (2002) found their cores without a central protostar to be near mass equipartition. The departure from equipartition by a factor 3, 10 and 30 are shown by dotted lines in Figure 4.32.

Protostellar cores are generally considered to be in “virial equilibrium” (Myers & Goodman, 1988). However, most density peaks formed by turbulence are unbound. Most of them are probably dissipated and never collapse into a dense core. Therefore, the significant differences observed in the M/M_{vir} ratios are thought (Morata et al., 2005) to indicate different evolution stages of the prestellar cores. Following this, some of our cores would be close to be to the stage of forming a central protostar.

4.11.1 Core Mass Function (CMF)

There is strong observational evidence for a link between the IMF and the CMF. The high-mass end ($0.5-1 M_{\odot}$) slope of the CMF ranges from -1.0 to -1.5 , measured in many low-mass star forming regions (see Ward-Thompson et al. (2007) for a full review of observational evidences), which matches that

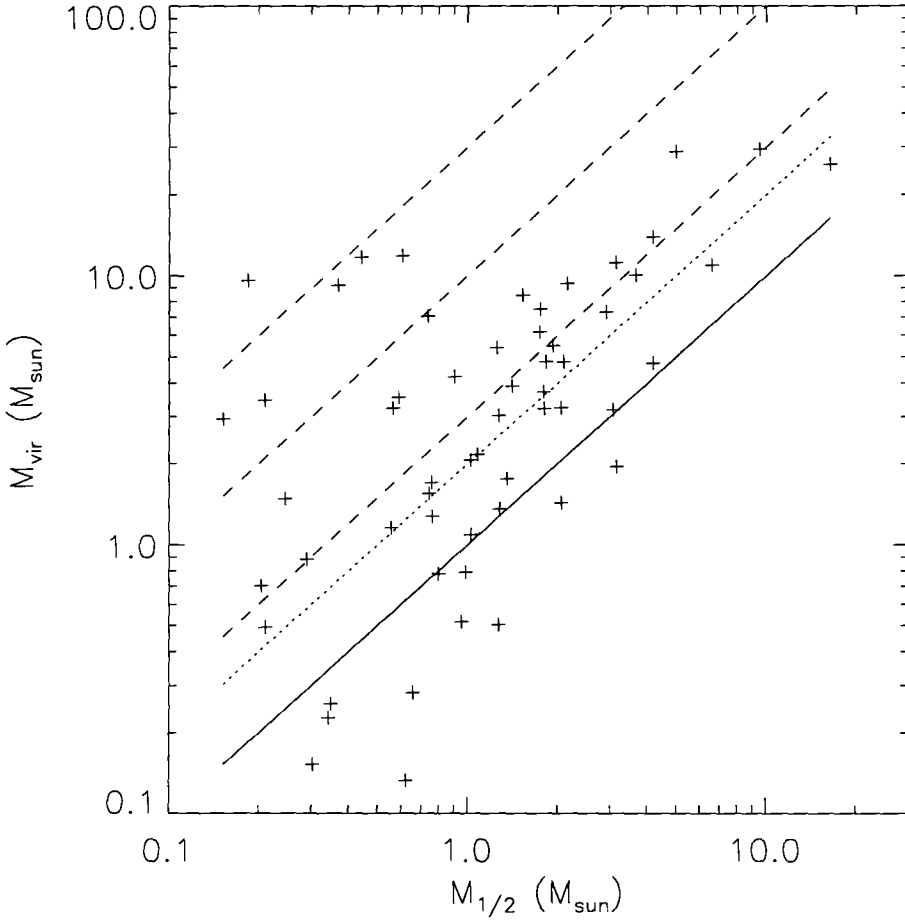


Figure 4.32 The virial mass ($M_{vir} = 210R[pc]\Delta_{eff}^2[km/s]$) of the cores is plotted as a function of $M_{1/2}$. The equipartition ($M_{1/2} = M_{vir}$) is shown by the full line. Departure from equipartition by a factor 3, 10 and 30 are shown by the dashed lines. The cores below the dotted line are bound.

of the IMF -1.35 (Salpeter, 1955). Also the peak mass of the CMF, found in the range of 0.2 to 1 M_{\odot} (Ward-Thompson et al., 2007) is only slightly larger than that of the IMF, ~ 0.08 to $\sim 0.2 M_{\odot}$ for single stars and multiple systems respectively (Chabrier, 2003).

However, larger discrepancies are found in the peak mass for more distant and massive star forming regions. Values as high as $\sim 8M_{\odot}$ are even

found (Reid & Wilson, 2005, 2006) for very massive regions. However, it is unclear whether this effect is due to an observational effect blending multiple sources at large distances.

To obtain an “observed” CMF with good statistics, we used the cores found with Clumpfind2D, see Section 4.2. We ran Clumpfind2D on the 4 column density maps shown on Figure 4.1 to 4.4 and combined the results to have better statistics. 731 cores were found in total. The resulting CMF is shown in Figure 4.33. The Salpeter power-law is also shown. The high mass range ($\leq 3 M_{\odot}$) agrees well with such a power-law. We found the end result quite sensitive to our choice of contours, especially at the high mass range where statistics are low. In general, reducing the number of contour lines reduced the slope at the high mass end. Using fewer contour lines has the effect of merging many cores that should be identified as independent objects of lesser mass. Using too many, on the other hand, would identify multiple cores in the density fluctuations of what appears as a single core. This would steepen the slope at high mass, since it would break the most massive cores into multiple lower mass ones.

The whole range of the distribution can also be well fit (see 4.33) with a log-normal function

$$CMF(\log m_{bin}) = A_0 \exp \left[- \left(\frac{\log m_{bin} - \log \mu_m}{\sigma_{\log m}} \right)^2 / 2 \right] \quad (4.11)$$

where $A_0 = 62.25$, the median mass is $\mu_m = 1.02 M_{\odot}$ and the log-mass dispersion $\sigma_{\log m} = 0.51$. The shape of the log-normal fit is very similar to the Chabrier (2005) IMF for multiple systems (shown in Figure 4.33, dotted line)

which has parameters $\mu_m = 0.2M_\odot$ and $\sigma_{\log m} = 0.55$. However, our median mass is significantly larger, by a factor of 4, which is in good agreement with the observed CMF.

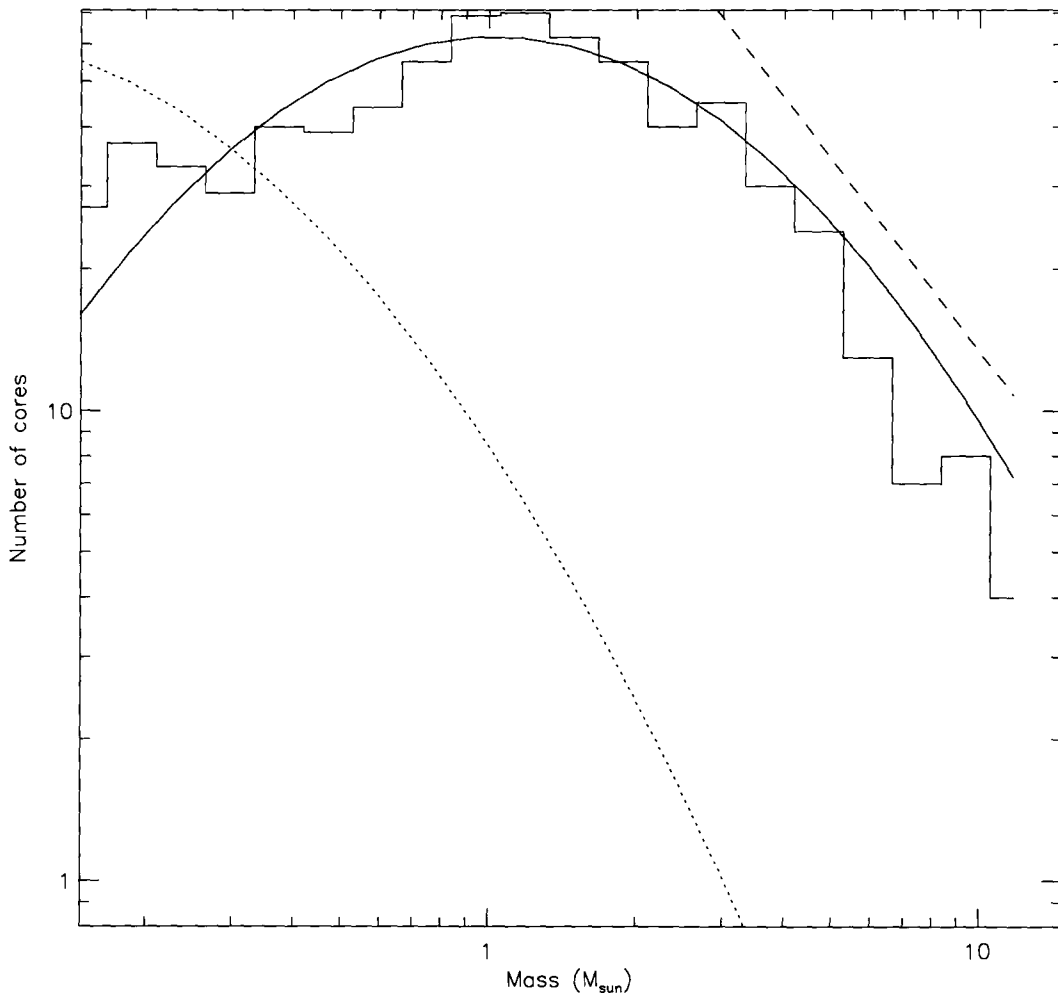


Figure 4.33 The CMF of the cores found with Clumpfind 2D, we combined the cores found in each simulation to get sufficient statistics. We also plotted the Salpeter power-law ($M^{-2.35}$) (dashed line), a log-normal fit to the data with Poisson statistical weighting (full line) and the Chabrier (2005) logarithmic multiple systems IMF (dotted line).

4.11.2 3D cores analysis

To compare some of our results found with the column density maps, we also did a 3D analysis of the cores. Given the rather subjective definition of cores, in terms of size, density (or column density) and mass, a different analysis using a different definition of cores can provide a healthy check on the methods used.

Here we defined our “cores” as density peaks, using a 3D density group finding algorithm. The program finds all the density peaks and creates a group if it contains at least a certain number of particles. The boundary of the groups are defined by the program by a contour of constant density. The only constraint we used was a minimum value of 200 particles to create “cores” of mass $>0.03 M_{\odot}$. This simple criterion eliminates the density fluctuation due to numerical noise and limits ourselves to the cores we consider resolved in number of particles. We found between 3372 to 4144 cores per simulation.

The core mass functions that we obtained this way for each simulation are shown in Figure 4.34, for the final time step (135 kyr). Every run had very similar CMFs, which are well fitted with a double power-law where $\Gamma_{low} = -0.8$ and $\Gamma_{high} = -1.9$ and a mass cutoff of $0.16 M_{\odot}$. The high mass slope is slightly steeper than observed values. We also combined the CMF found for each simulation (thick black line) and fit the resulting distribution by a log-normal, we found $\mu_m = 0.0068 M_{\odot}$ and $\sigma_{\log m} = 0.70$. The peak mass is significantly smaller, even smaller than the typical values found for IMF. This difference was expected, since we have the full 3D density information. When looking at a 2D column density map, many cores located along similar lines of sight can be merged together to form larger objects. Therefore, a smaller peak mass was expected. This effect can also explain the steeper slope at the

high mass end of the distribution. The most massive cores are more likely to be identified as multiple smaller object when using the full 3D information.

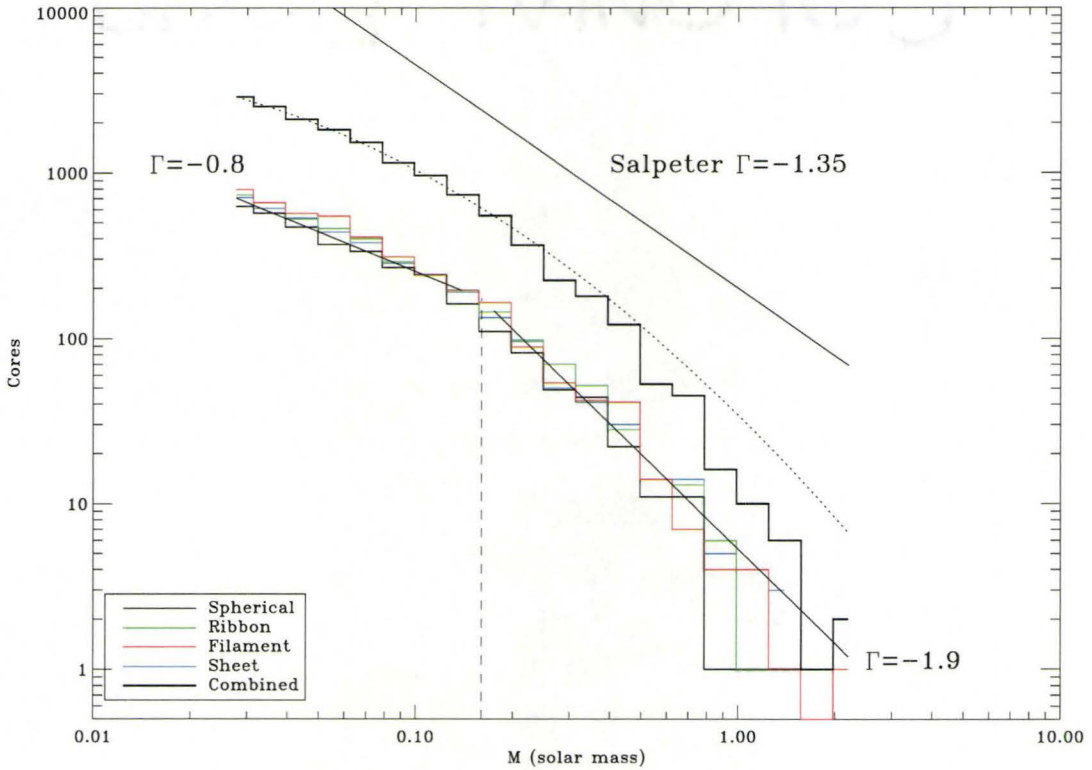


Figure 4.34 CMF for each simulation at the final time step (135 kyr). The dashed line represents the breaking point between the double power-law relation and the best fit power-laws are also shown. The resulting CMF from combining the CMF of each simulation are shown (thick line) and also its log-normal fit (dotted line).

On figure 4.35 we plot the virial mass in function of the actual mass of the cores for each simulations. This figure can be compared to figure 4.32 to display the dynamical state of these cores. We found that many of them are bound (i.e. at energy equipartition $E_{Kin} = E_{Grav}$ where $M_{1/2} = M_{vir}/2$) or close to bound, but most of them are not bound. We also find that the number of the unbound cores is decreasing with mass.

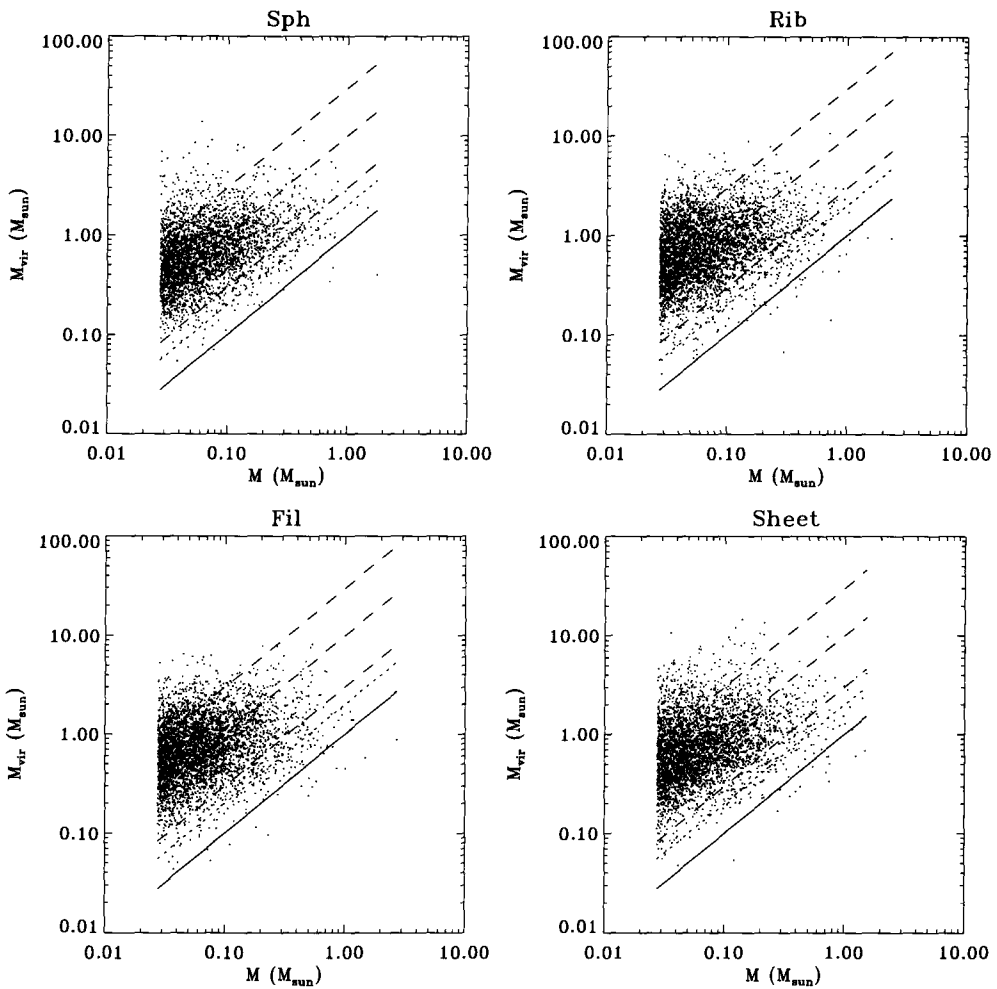


Figure 4.35 Virial mass of the 3D density group cores is plotted in function of their mass. The lines are the same as the one shown in Figure 4.32.

In Figure 4.36 we plotted the CMF of the bounded cores (dashed lines) for each simulation and compared it to the full respective CMF (full line). We found a total of 379 bounded cores, representing between 0.44 to 0.91 % of the total cloud mass. This very low core formation efficiency is consistent with the estimates ($\leq 1 - 20\%$) from recent very large submillimeter continuum surveys (Hatchell et al., 2005; Nutter et al., 2006).

For better statistics we combined the bound cores of the 4 simulations

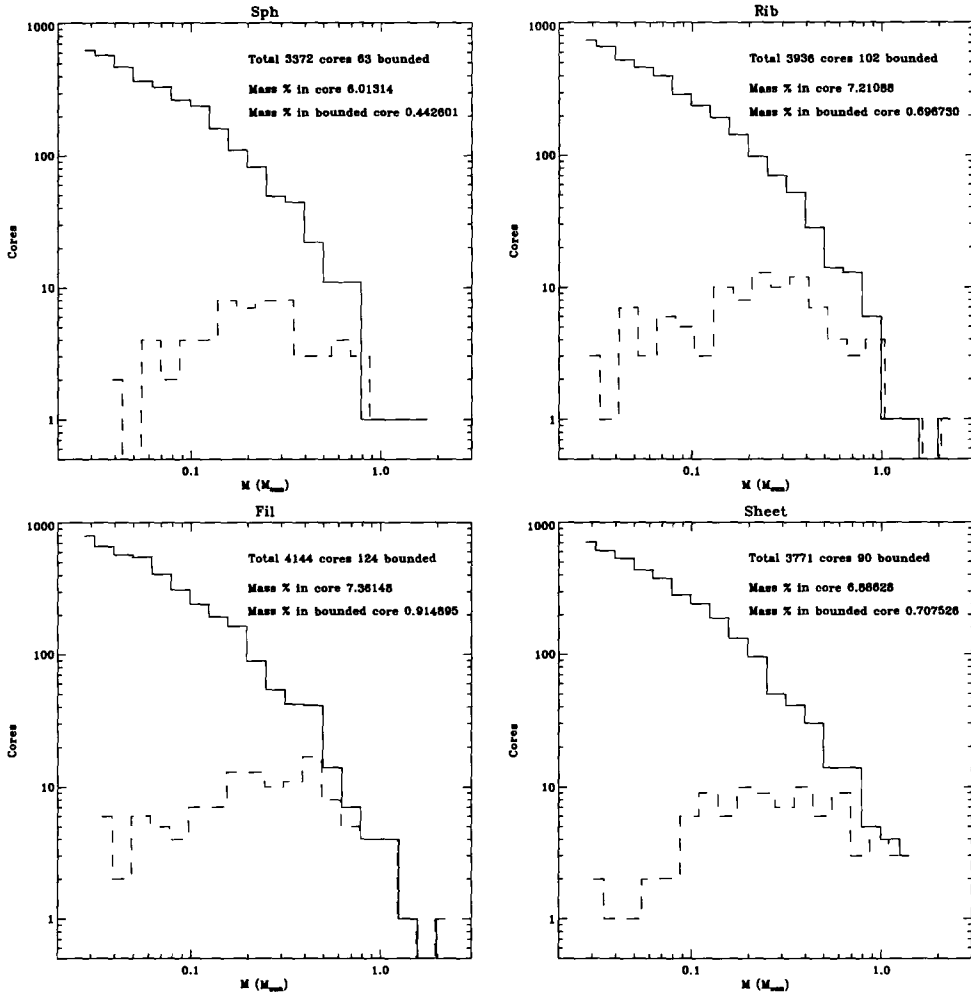


Figure 4.36 CMF of the bounded cores (dashed lines) compared to the total CMF (full lines) for each simulation.

and plotted the combined CMF (Figure 4.37). We could fit a log-normal with $\mu_m = 0.246M_\odot$ and $\sigma_{\log m} = 0.37$ to the data. The distribution has a smaller dispersion and the slope at the high mass end is slightly steeper, as expected previously. The peak of the distribution is now remarkably close to the observed ($0.2M_\odot$) IMF peak for multiple systems (Chabrier, 2005). The peak mass found from the 2D column density map is therefore significantly larger, by a factor ~ 4 . This implies that the peak mass estimated from 2D

column density map is probably overestimated.

In the context of the one-to-one transfer scenario from the CMF to IMF (Goodwin et al., 2008), this means that the already relatively high estimated star formation efficiency ($\epsilon_{core} \equiv M_*/M_{core} \sim 30 - 50\%$, André et al. (2008)), would be even higher.

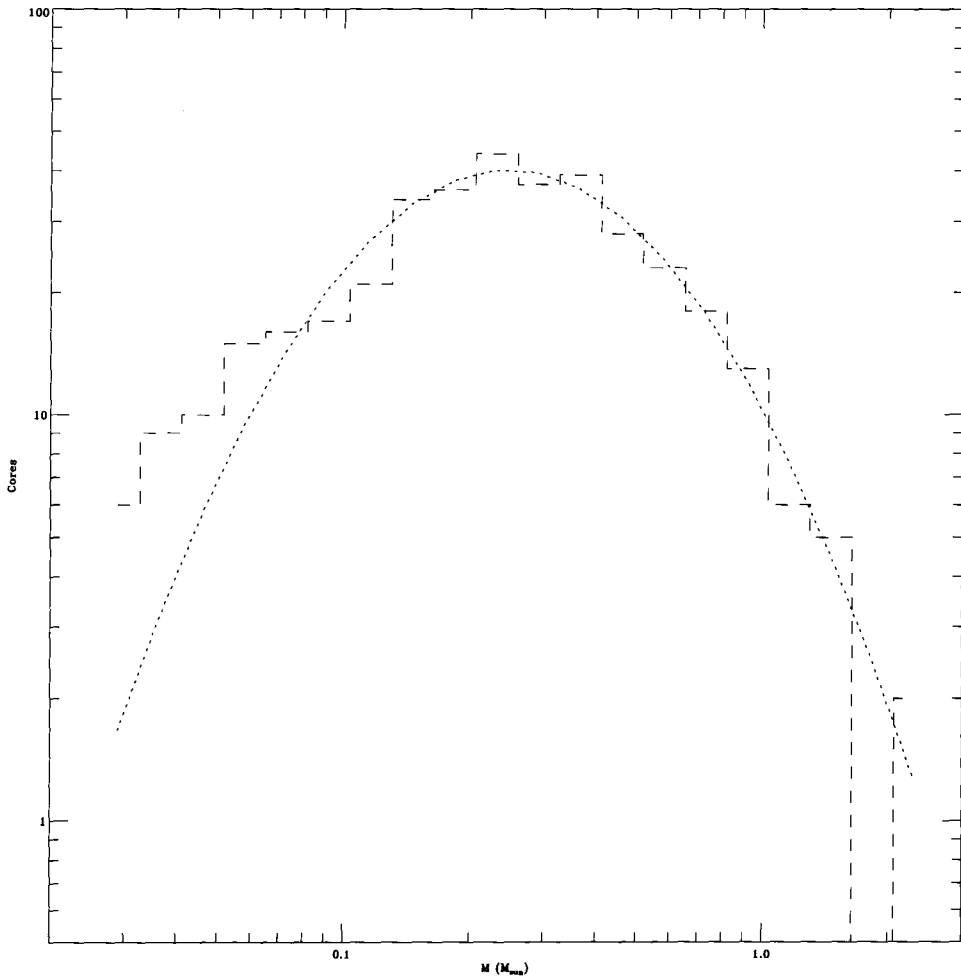


Figure 4.37 CMF of the combined bounded cores (dashed lines) with the log-normal fit (dotted line).

The mass we estimated from 2D column density maps can be overestimated in 2 ways. First we could have multiple objects aligned along the line

of sight. This situation didn't occur for any of the cores we looked at in detail. Some cores were fairly close, but no clear core overlapped along the 3 different lines of sight we looked at. Merging of cores could however happen depending on the specific choices of contours. However, the chances of this happening are strongly influenced by the total mass/size of the molecular cloud and the mass distribution along the line of sight. Both effects could be observed as a higher background column density.

The second way the mass of core can be overestimated is by the presence of large amount of low density gas along the line of sight. This was observed for every "fake" core we looked at. We found elongated structures of density larger than the background, lined up along the line of sight we were looking through.

We therefore estimated to which extent the low density gas along the line of sight could increase the mass of our objects. In Figure 4.38 we plotted the masses found by integrating the column density within $R_{1/2}$ in 2 different ways. To estimate the real mass of the cores, we calculated the column density by limiting the lines of sight to go only through the cores themselves ($M_{1/2}^{cut}$). We then compared this mass to the one found by letting the lines of sight go through the whole cloud ($M_{1/2}^{all}$). We found every cores mass overestimated by at least a factor 2 (full line), in every directions. Most cores were found to be overestimated below a factor 6 (dashed line), except for the "fake" cores (open diamonds) whose mass can be wildly overestimated.

We found a global averaged ratio of $M_{1/2}^{all}/M_{1/2}^{cut} = 4.978$. For the "fake" cores the ratio is much higher (9.038) and for the "real" cores only we found 4.064. Assuming most of the cores identified by Clumpfind2D were "real", the low density gas along the line of sight can explain the shift by a factor ~ 4 in

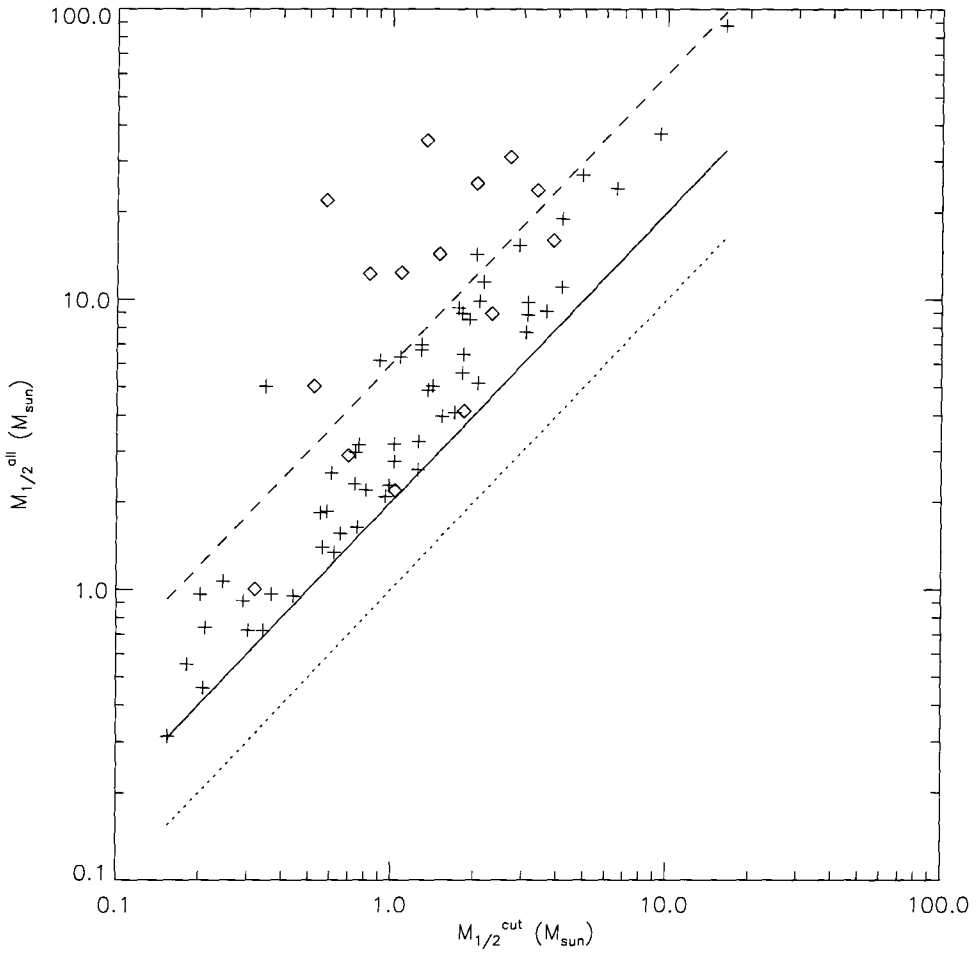


Figure 4.38 Mass of the cores integrated along the whole line of sight ($M_{1/2}^{all}$), in function of the real mass of the cores ($M_{1/2}^{cut}$). The “+” represent the “real” cores from 3 orthogonal directions (x, y, z). Similarly, the “fake” cores are represented by the open diamonds. The dotted line shows equal masses, the full line an overestimation by a factor 2 and the dashed line a factor 6.

the CMF.

This effect is larger than we originally thought, and raises the question whether observations could also be biased towards higher mass this way. Observations are however slightly different to our simulated observations. They observe the dust emission flux, always assuming the gas is optically thin. Our

method also makes this approximation, by integrating all the mass along the line of sight. Observers (e.g. Reid & Wilson (2005)) however subtract a background flux level in a very specific way. They in fact, measure the flux differences on a certain angular scale specific to the telescope. The background subtraction would therefore be unique to each observed regions, since they are located at different distances. Further investigations of the background subtraction effects would be helpful to distinguish whether the CMF mass peak is changing from a star formation regions to another or if it is more universal. Our work indicates, at least, that this background subtraction method could have more impact on the mass determination than previously though.

4.12 Conclusion

In this chapter, we found that most observed core properties can be reproduced fairly well with isothermal hydrodynamics simulations, without adding any extra physics like magnetic fields, outflows, a proper equation of state or radiative transfer.

The cores we identified as CC were found to correspond well to the observed prestellar cores. They are centrally concentrated, self-gravitating and unlikely to be transient objects. They do not have a central denser object and they are also seen in the dense molecular gas tracers (N_2H^+ and NH_3). However, our CC cores do not show signs of infall motions. The cores we identified as N are very similar to the observed protostellar cores. They contain a dense object in the center of a core-like envelope and show signs of accretion. The objects we classified as CR are similar to starless cores in many aspects. They do not show signs of infall, they are not centrally concentrated and

therefore doesn't appear tightly bound. However, they are denser than the observed starless cores, because our CR objects are seen in dense molecular tracers and not in $C_{18}O$. They are therefore at an intermediate stage between starless and prestellar cores.

The cores in our simulations had density profiles very similar to the observed cores. We found a good agreement in the size of the inner "flat" part, which is very meaningful because we would expect this property of the dense core to be very sensitive to the equation of state or the magnetic field. This indicates that for the early stages of star formation, the gas can collapse and stay nearly isothermal and that magnetic fields have little effects. Only the edges of our density profiles were shallower than observed.

The velocity dispersion in our cores were different for the CC-CR and the N cores. Our CC and CR cores had near sonic velocity dispersion in the center and showed an increase at the edges, like most observations suggest. Note that our velocity dispersion at the center are slightly high than the sub-sonic values observed, but Offner et al. (2008) reported measuring a bias towards higher velocity dispersion for direct measurements. They found a lower velocity dispersion when fitting the velocity spectrum with a Gaussian, the way observers do. They found the velocity distribution peak to be well fitted with a Gaussian, but much broader wings near the bottom 10%. These outliers, likely neglected in observations, will increase significantly the velocity dispersion measured directly. So the discrepancies between the observed velocity dispersions and our measurements are not significant.

The N cores on the other hand, showed the opposite trend; high supersonic velocity dispersion near the center, due to infall and rotation motions, with a decrease near the edges. This discrepancy with observed protostellar

objects was also observed in simulations by Offner et al. (2008). A possible explanation for this would be a departure from the optically thin assumption near the central dense object. Since most of the infall and rotation motions in our simulations were observed to be constrained to very small scales around the nucleus, only localized departure from optically thin conditions could explain the lack of observational evidences for these motions.

We could also quantify the observed relation between velocity dispersion and gas density ($\sigma \sim \rho^{-0.222}$).

We found that the rotation was not dynamically significant, in agreement with observations, and the observational method used to estimate the velocity gradient could even overestimate the actual angular momentum. We also proposed a core formation scenario (see section 4.3), where accretion would occur mostly along dense filaments, that naturally explains the low rotation gradients observed.

The overall shape of the CMFs we obtained were in good agreement with observations. However, we found a large discrepancy in the mass peak of the CMF we found using Clumpfind2D on our column density map and the one we found from the bounded density peaks. Clumpfind found a CMF more massive by a factor ~ 4 due to the low density gas contributing to the column density along the line of sight. We question whether or not this could also affect observations.

Bibliography

André, P., Basu, S., & Inutsuka, S.-i. 2008, arXiv:0801.4210

Ayliffe, B. A., Langdon, J. C., Cohl, H. S., & Bate, M. R. 2007, MNRAS, 374,
1198

Barranco, J. A., & Goodman, A. A. 1998, ApJ, 504, 207

Beltrán, M. T., Cesaroni, R., Neri, R., Codella, C., Furuya, R. S., Testi, L., &
Olmi, L. 2004, ApJ, 601, L187

Caselli, P., Benson, P. J., Myers, P. C., & Tafalla, M. 2002, ApJ, 572, 238

Chabrier, G. 2003, PASP, 115, 763

Chabrier, G. 2005, The Initial Mass Function 50 Years Later, 327, 41

Chandrasekhar, S. 1951, Proc. R. Soc. London, 210, 26

Chen, X., Launhardt, R., & Henning, T. 2007, ApJ, 669, 1058

Di Francesco, J., Myers, P. C., Wilner, D. J., Ohashi, N., & Mardones, D.
2001, ApJ, 562, 770

- Goodman, A. A., Benson, P. J., Fuller, G. A., & Myers, P. C. 1993, *ApJ*, 406, 528
- Goodman, A. A., Barranco, J. A., Wilner, D. J., & Heyer, M. H. 1998, *ApJ*, 504, 223
- Goodwin, S. P., Nutter, D., Kroupa, P., Ward-Thompson, D., & Whitworth, A. P. 2008, *A&A*, 477, 823
- Hatchell, J., Richer, J. S., Fuller, G. A., Qualtrough, C. J., Ladd, E. F., & Chandler, C. J. 2005, *A&A*, 440, 151
- Kegel, W. H. 1989, *A&A*, 225, 517
- Kirk, H., Johnstone, D., & Tafalla, M. 2007, *ApJ*, 668, 1042
- Klessen, R. S., Ballesteros-Paredes, J., Vázquez-Semadeni, E., & Durán-Rojas, C. 2005, *ApJ*, 620, 786
- Larson, R. B. 1981, *MNRAS*, 194, 809
- Mac Low, M.-M., & Klessen, R. S. 2004, *Reviews of Modern Physics*, 76, 125
- Morata, O., Girart, J. M., & Estalella, R. 2005, *A&A*, 435, 113
- Myers, P. C. 1983, *ApJ*, 270, 105
- Myers, P. C., & Goodman, A. A. 1988, *ApJ*, 326, L27
- Nutter, D., Ward-Thompson, D., & André, P. 2006, *MNRAS*, 368, 1833
- Offner, S. S. R., Krumholz, M. R., Klein, R. I., & McKee, C. F. 2008, *AJ*, 136, 404

- Padoan, P., Juvela, M., Goodman, A. A., & Nordlund, Å. 2001, *ApJ*, 553, 227
- Peretto, N., André, P., & Belloche, A. 2006, *A&A*, 445, 979
- Reid, M. A., & Wilson, C. D. 2005, *ApJ*, 625, 891
- Reid, M. A., & Wilson, C. D. 2006, *ApJ*, 644, 990
- Salpeter, E. E. 1955, *ApJ*, 121, 161
- Scalo, J. 1990, *Physical Processes in Fragmentation and Star Formation*, 162, 151
- Schöier, F. L., van der Tak, F. F. S., van Dishoeck, E. F., & Black, J. H. 2005, *A&A*, 432, 369
- Tachihara, K., Onishi, T., Mizuno, A., & Fukui, Y. 2002, *A&A*, 385, 909
- Tafalla, M., Myers, P. C., Caselli, P., Walmsley, C. M., & Comito, C. 2002, *ApJ*, 569, 815
- Tafalla, M., Myers, P. C., Caselli, P., & Walmsley, C. M. 2004, *A&A*, 416, 191
- Tilley, D. A., & Pudritz, R. E. 2004, *MNRAS*, 353, 769
- Walmsley, C. M., Flower, D. R., & Pineau des Forêts, G. 2004, *A&A*, 418, 1035
- Walsh, A. J., Myers, P. C., & Burton, M. G. 2004, *ApJ*, 614, 194
- Walsh, A. J., Myers, P. C., Di Francesco, J., Mohanty, S., Bourke, T. L., Gutermuth, R., & Wilner, D. 2007, *ApJ*, 655, 958

Ward-Thompson, D., André, P., Crutcher, R., Johnstone, D., Onishi, T., &
Wilson, C. 2007, *Protostars and Planets V*, 33

Williams, J. P., de Geus, E. J., & Blitz, L. 1994, *ApJ*, 428, 693

Chapter

5

Conclusion

In this thesis, we presented SPH simulations of clustered star formation. We wanted to test the use of sink particles in such simulations. To do so we reproduced Bate et al. (2003)'s simulations. We also addressed whether gravity could be an efficient driver of turbulence and we compared the prestellar objects we formed to observations. To do so we ran simulations of gravitationally collapsing molecular clouds and stopped the simulations after the first prestellar objects formed. This removed the requirement to use sink particles and the issues related to stellar feedback.

In chapter 2 we successfully reproduced the key characteristics of the star cluster simulation done by Bate et al. (2003). Both simulations had the same main discrepancy with the observed IMF: too many low mass objects (brown dwarfs) were forming in the late stages of the simulation. This result appears to be related, as expected, to the lack of radiative feedback in the simulations. Bate (2008) did the same simulation but including radiative transfer this time and found that it could effectively reduce fragmentation and

especially limit the formation of brown dwarfs. Including radiative transfer therefore seems essential to follow star formation processes accurately past the dense core stage.

We show in chapter 3 that turbulence in a self-gravitating supersonic molecular cloud does not decay as it has been shown in supersonic turbulent periodic boxes. We show that the gravitational energy of the cloud converts to kinetic energy and acts as the “driver” of turbulence. We also show that the turbulence generated this way is in very good agreement with the observed properties of turbulence within molecular clouds. We therefore argue that, yes, molecular cloud are driven, they are driving themselves through gravitational collapse. Stellar feedback could also contribute, but gravitational collapse can naturally explain the apparent multi-scale uniformity of turbulence.

In our study of dense cores, we found that most observed core properties can be reproduced fairly well with isothermal hydrodynamics simulations, without adding any extra physics like magnetic fields, outflows, a proper equation of state or radiative transfer.

The cores in our simulations had density profiles very similar to the observed cores. We found a good agreement in the size of the inner “flat” part, which is very meaningful because we would expect this property of the dense core to be very sensitive to the equation of state or the magnetic field. This indicates that for the early stages of star formation, the gas can collapse and stay nearly isothermal and that magnetic fields have little effects. Only the edges of our density profiles were shallower than observed.

We identified 3 different types of cores in our simulations, in increasing order of central concentration, we found *compact regions* (CR), *centrally concentrated* (CC) objects and *nucleus* (N) cores. The velocity dispersion in our

cores were different for the CR-CC and the N cores. Our CC and CR cores had near sonic velocity dispersion in the center and showed an increase at the edges, like most observations suggest. The N cores, on the other hand, showed the opposite trend: high supersonic velocity dispersion near the center, due to infall and rotation motions, with a decrease near the edges. This discrepancy with observed protostellar objects was also observed in simulations by Offner et al. (2008). A possible explanation for this would be a departure from the optically thin assumption near the central dense object. Since most of the infall and rotation motions in our simulations were observed to be constrained to very small scales around the nucleus, only localized departure from optically thin conditions could explain the lack of observational evidences for these motions.

We found that the rotation was not dynamically significant, in agreement with observations, and the observational method used to estimate the velocity gradient could even overestimate the actual angular momentum. We also proposed a core formation scenario (see section 4.3), where accretion occurs mostly along dense filaments, that naturally explains the low rotation gradients observed.

The overall shape of the CMFs we obtained were in good agreement with observations. However, we found a large discrepancy in the mass peak of the CMF we found using Clumpfind2D on our column density map and the one we found from the bounded density peaks. Clumpfind found a CMF more massive by a factor ~ 4 due to the low density gas contributing to the column density along the line of sight. We question whether or not this could also affect observations.

5.1 Future work

In the near future, a few more things could be done with these simulations. It would be interesting to simulate observations even further by producing spectrum of emission, for a given molecule, along the lines of sight. This way we could measure the velocity dispersion of cores the same way observers do, by fitting a Gaussian to the spectrum. This would be a closer measurement than the direct calculation of the velocity dispersion, which is biased if the distribution is not perfectly Gaussian.

With the emission spectra, we could also use the 2.5 dimensions (x, y, v_z) version of Clumpfind. From the velocity spectrum, it would be possible to identify if a column density peak is a single object or not. We could potentially eliminate a few “fake” cores this way.

Further down the road, the next step we would want to take these simulations would be to let them evolve further in time. To be able to run the simulations further in time, we would need to use something like sink particles. So we should work on improving this technique and solve the boundary issues. However, to let the simulation go later than the first star forming would require to include also radiative transfer. In this density regime, the stellar and accretion process emissions would have major effects on their environment (Bate, 2008).

The next things to worry about would be another form of stellar feedback, outflows. This could potentially increase the overall kinetic energy of the gas significantly. Also it would strongly affect the “local” gas distribution around stars.

The understanding of star formation is such a central problem to as-

trophysics. It is a key element in our understanding of a wide range of objects from galaxies, to brown dwarfs, to planets and even to life! This work contributed to a better understanding, however there is much more to be done and in the next few years, advances in computers, physics and observations should lead to a breakthrough in our understanding.

Bibliography

Bate, M. R., Bonnell, I. A., & Bromm, V. 2003, MNRAS, 339, 577

Bate, M. R. 2008, arXiv:0811.1035

Offner, S. S. R., Krumholz, M. R., Klein, R. I., & McKee, C. F. 2008, AJ, 136,

404

Appendix **A**

Appendix A

```
;;;;;;  
;;;;; Generate the 3-D initial divergence free turbulence field ;;;;;;  
;;;;;;
```

```
pro ic_turb, saveplot=saveplot
```

```
;;;;;;
```

```
machn= 6.4
```

```
pwrspeci=-4.
```

```
n=128L
```

```
L=n/2.
```

```
filename='/home/petitscn/idl/junk.dat'
```

```
;;;;;;
```

```
pi=3.1415926535897932384626d0
```

```
seed=3.2
```

```
nx=n
```

```
ny=n
nz=n
v1c= dcomplexarr(n,n,n)
v2c= dcomplexarr(n,n,n)
v3c= dcomplexarr(n,n,n)
sum=0d0
sum2=0d0
idiv=0

;; Setup of |k|^(n/2)
for k=1,nz/2+1 do begin
  rkz= 2d0*pi/L*(k-1)
  if (k gt nz/2) then rkz = 2*pi/L*(k-nz-1)
  kc = k
  if (k gt 1 and k ne nz/2+1) then kc = nz+2-k

  for j=1,ny do begin
    rky= 2d0*pi/L*(j-1)
    if (j gt ny/2) then rky = 2*pi/L*(j-ny-1)
    jc = j
    if (j gt 1 and j ne ny/2+1) then jc = ny+2-j

    for i=1,nx do begin
      rkx= 2d0*pi/L*(i-1)
      if (i gt nx/2) then rkx = 2*pi/L*(i-nx-1)
      ic = i
      if (i gt 1 and i ne nx/2+1) then ic = nx+2-i
      rk=sqrt(rkx^2+rky^2+rkz^2)
```

```

    tamp=double(rk)
    if (rk GT 2*pi/L*10./4.) then begin
tamp= double(rk^(pwrspeci/2.))
    endif else begin
        tamp=0.
    endelse

;; Setup of random unit vectors
randa= 2*pi*randomu(seed)
randv =0.
while (randv GT .5 or randv LE 0.) do begin
    xrand=randomu(seed)-.5
yrand=randomu(seed)-.5
zrand=randomu(seed)-.5
randv = sqrt(xrand^2+yrand^2+zrand^2)
endwhile
xrand=xrand/randv
yrand=yrand/randv
zrand=zrand/randv
denom=sqrt((rkx*yrand-rky*xrand)^2+(-rkx*zrand+rkz*xrand)^2+(rky*
zrand-rkz*yrand)^2)

; Cross product of vk
if (denom NE 0) then begin
    amp=tamp*complex(cos(randa),sin(randa))
    v1c(i-1,j-1,k-1)= amp*(-rkz*yrand+rky*zrand)/denom
v2c(i-1,j-1,k-1)= amp*(-rkx*zrand+rkz*xrand)/denom
v3c(i-1,j-1,k-1)= amp*(-rky*xrand+rkx*yrand)/denom

```

```

endif
if (k gt 1 and k lt nz/2+1) then begin
  v1c(ic-1,jc-1,kc-1)= conj(v1c(i-1,j-1,k-1))
  v2c(ic-1,jc-1,kc-1)= conj(v2c(i-1,j-1,k-1))
  v3c(ic-1,jc-1,kc-1)= conj(v3c(i-1,j-1,k-1))
endif

; Check for div(v)=0
div= complex(0,1.0)*(rkx*v1c(i-1,j-1,k-1) +rky*v2c(i-1,j-1,k-1)+
  rkz*v3c(i-1,j-1,k-1) )
sum= sum + abs(div)
sum2 = sum2 + abs(rk)*sqrt(abs(v1c(i-1,j-1,k-1))^2+
  abs(v2c(i-1,j-1,k-1))^2+abs(v3c(i-1,j-1,k-1))^2)
if (abs(div) GT idiv) then begin
  idiv=abs(div)
  vom = abs(rk)*sqrt(abs(v1c(i-1,j-1,k-1))^2+
    abs(v2c(i-1,j-1,k-1))^2+abs(v3c(i-1,j-1,k-1))^2)
endif
endfor
endfor
endfor

for k=1,nz/2+1,nz/2 do begin
  kc = k                ;special cases kc = k
  for j=2,ny/2 do begin  ;not 0 or Nyquist
    jc = j
    if (j gt 1 and j ne ny/2+1) then jc = ny+2-j
    for i=1,nx do begin

```

```

    ic = i
    if (i gt 1 and i ne nx/2+1) then ic = nx+2-i
    v1c(ic-1,jc-1,kc-1)= conj(v1c(i-1,j-1,k-1))
    v2c(ic-1,jc-1,kc-1)= conj(v2c(i-1,j-1,k-1))
    v3c(ic-1,jc-1,kc-1)= conj(v3c(i-1,j-1,k-1))
  endfor
endfor
endifor

for k=1,nz/2+1,nz/2 do begin
  kc = k                      ;special cases kc = k
  for j=1,ny/2+1,ny/2 do begin
    jc = j                    ;special case jc = j
    for i=1,nx/2+1 do begin
      ic = i
      if (i gt 1 and i ne nx/2+1) then ic = nx+2-i
      v1c(ic-1,jc-1,kc-1)= conj(v1c(i-1,j-1,k-1))
      v2c(ic-1,jc-1,kc-1)= conj(v2c(i-1,j-1,k-1))
      v3c(ic-1,jc-1,kc-1)= conj(v3c(i-1,j-1,k-1))
    endfor
  endfor
endifor

print, 'mean of div(v)_k=',sum/n^3,sum2/n^3

; Fourier transform back to real space
v1=FFT(v1c,dimension=0,/inverse,double=1)
v2=FFT(v2c,dimension=0,/inverse,double=1)

```

```
v3=FFT(v3c,dimension=0,/inverse,double=1)
v1= real_part(v1)
v2= real_part(v2)
v3= real_part(v3)

; Normalize velocities
v1a=mean(v1)
v2a=mean(v2)
v3a=mean(v3)
v1= v1-v1a
v2= v2-v2a
v3= v3-v3a

speed= sqrt(v1^2+v2^2+v3^2)
speedrms= mean(speed)

v1=v1*Machn/speedrms
v2=v2*Machn/speedrms
v3=v3*Machn/speedrms
speed2= sqrt(v1^2+v2^2+v3^2)
speedrmsf=mean(speed2)
print,'Final RMS Mach number=',speedrmsf

;; Plot a 2-D slice at k=10 of the 3-D velocity field
velovect,v1(*,*,10),v2(*,*,10)

openw,8,filename
writeu,8,v1,v2,v3
```

FREE_LUN, 8

end